UNIVERSITÀ DEGLI STUDI DI NAPOLI FEDERICO II

PH.D. THESIS

IN

INFORMATION TECHNOLOGY AND ELECTRICAL ENGINEERING

SYNTHETIC APERTURE RADAR FOR NATURAL HAZARDS OBSERVATION

FROM ACQUISITION GEOMETRY TO APPLICATIONS TO LANDSLIDES

DOMENICO ANTONIO GIUSEPPE DELL'AGLIO

TUTOR: PROF. ANTONIO IODICE

COORDINATOR: PROF. DANIELE RICCIO

XXXII CICLO

SCUOLA POLITECNICA E DELLE SCIENZE DI BASE
DIPARTIMENTO DI INGEGNERIA ELETTRICA E TECNOLOGIE DELL'INFORMAZIONE

to Annamaria
and to our purpiceddu

This page intentionally left blank.

Contents

This page intentionally left blank.

List of Acronyms

The following acronyms are used throughout this text.

1D	One-Dimensional
1D-FT	Two-Dimensional Fourier Transform
2D	Two-Dimensional
2D-FT	Two-Dimensional Fourier Transform
3D	Three-Dimensional
AOI	Area Of Interest
DEM	Digital Elevation Model
DInSAR	Differential Interferometric Synthetic Aperture Radar
FFT	Fast Fourier Transform
FM	Frequency Modulation
FT	Fourier Transform
GBInSAR	Ground Based SAR Interferometry
GCP	Ground Control Point

GPS	Global Positioning System
IDL	Interactive Data Language
InSAR	Interferometric Synthetic Aperture Radar
LM	Local Machine
LOS	Line Of Sight
MP	Measurement Point
pdf	probability density function
PRF	Pulse Repetition Frequency
PS	Permanent Scatterers
RAR	Real Aperture Radar
RCM	Range Cell Migration
RMSE	Root Mean Square Error
S1	Sentinel-1
SAR	Synthetic Aperture Radar
SBAS	Small BAseline Subset
SLC	Single Look Complex
SNAP	SentiNel Application Platform
SPOT	Sub-Pixel Offset Tracking
SRTM	Shuttle Radar Topography Mission
SVD	Singular Value Decomposition

TF Transfer Function

VM Virtual Machine

This page intentionally left blank.

List of Tables

This page intentionally left blank.

List of Figures

Chapter 1

Introduction

This thesis is a compendium of some of the results of my research activities carried out within the Ph.D. degree in Information Technology and Electrical Engineering at the University of Naples “Federico II”. The presented research topics are related to the remote sensing field using Synthetic Aperture Radar (SAR) data.

The importance of remote sensing sensors for the imaging of the Earth surface is well known within the scientific community. In the last decades, the increasing number of space missions have further confirmed the benefit derived from use of such systems, for the natural and human environment. Remote sensing sensors can be classified in two main categories: *passive* and *active* systems. The former use the radiation naturally emitted or reflected by the Earth surface (Fig. 1.1); the latter are equipped with a transceiver antenna illuminating the Earth surface and receiving the relative backscattered signal (Fig. 1.2).

Passive sensors are now in order. Earth emits energy in the form of electromagnetic waves approximately as a black body, with relevant radiation in some portions of the thermal infrared (spectral range 2.5 to 15 μm) and of the microwave (0.001 to 1 m) bands. Furthermore, it is illuminated

Figure 1.1. Electromagnetic radiation received by passive systems.

Figure 1.2. Electromagnetic radiation received by active systems.

by the Sun (and by the Moon), with relevant reradiation in the visible (0.4 to 0.7 μm), near infrared (0.7 to 1.3 μm) and ultraviolet (0.01 to 0.4 μm), regions [1].

The *spatial resolution* plays an important role for any imaging system. It is defined as the minimum distance at which two different objects are detected by the sensor as separated. Resolution on the order of few meters or tens of meters can be achieved by visible and infrared sensors. For instance, this is the case of the Enhanced Thematic Mapper Plus (ETM+) system of the LANDSAT-7 satellite [2]. It generates eight spectral bands in blue, green, red, Near InfraRed (NIR) and Mid-InfraRed (MIR). Bands 1-5 and 7 have 30 m resolution. The panchromatic (band 8) has 15 m resolution. The thermal band has 60 m resolution. Sensors such that are largely used in many applications such as land cover mapping, water resources management, soil protection, risk assessment. Two main drawbacks are evident: for first, the presence of clouds or fog covering the area under investigation and, secondly, the absence of an independent source of radiation. These constraints are overcome by active sensors that can be considered the complement of the passive ones.

When we talk about active sensors we mean radar systems working in the microwave region of the electromagnetic spectrum [3]. They are commonly referred as *Real Aperture Radars* (RARs). These systems allow to obtain images in any weather conditions, at any time (day and night). Their main limitation is due to the poor resolution achievable that is inversely proportional to the sensor flight-path antenna dimension, for a fixed working frequency and a fixed sensor-to-surface distance. In fact, microwave sensors flying at hundreds of kilometers distance from the Earth surface would have antenna dimension between several hundred meters to some kilometers (depending on the specific operating frequency) to reach resolutions on the order of magnitude of meters.

A suitable method to overcome this limitation is based on the concept of the *synthetic antenna* and its implementation on the *Synthetic Aperture Radar* (SAR) systems [4]. Indeed, it is possible to synthesize a very long antenna by moving a small one along a proper path (typically, the sensor flight path) and then appropriately processing the received signals. These operations allow to obtain an along path resolution higher than the RAR one and independent from the sensor altitude, making the SAR an essential tool for Earth [5] and other planets monitoring [6]. This is supported by the increasing number of missions involving SAR sensors. For instance, the European Space Agency (ESA) has tens-year-long experience on this field and, in the last years, it has strongly contributed to produce more impulse to remote sensing research by choosing to give the images provided by its twin SAR satellites Sentinel-1 [7] free of charge.

Therefore, the research activities started from the idea that remote sensing techniques and applications play a key rule in the Earth observation. Especially nowadays, where the effects of climate change on our life is more and more evident. Starting from this general statement, three research topics were identified and investigated leading to the results presented in this dissertation.

The first one (section 4.2) concerns the SAR acquisition geometry, i.e., the way the SAR sensor acquires data from the ground. Several modes are possible and for each of them a specific formulation and processing algorithm are available in literature. We present a unified formulation able to express SAR raw signals for any acquisition geometry. This formulation is then used to show that both sliding spotlight and TOPSAR raw signal simulation of extended, both canonical and realistic, scenes can be achieved also accounting for sensor trajectory deviations.

Developing efficient simulators like this is an important task nowadays. In fact, in the last years, we have observed the great effort provided by different space agencies around the world, leading to an increasing number of remote sensing satellites. Two relevant examples are provided by the ESA and the Italian Space Agency (ASI) that have launched the Sentinel-1 and the Cosmo-SkyMed missions, respectively. The main purpose of these missions is to generate useful products for the Earth Monitoring applications. This general idea lead us directly to the other two research topics developed within the Ph.D program and presented in this thesis.

The second topic (section 5.2.1) of research has been conducted during the 2019, under the aegis of the Progressive Systems Srl. The global project aims to demonstrate a monitoring service prototype through automated Earth Observation geo-spatial data analyses using the satellite interferometry technique, in order to monitor infrastructures in the long term period. For the validation of this service prototype, the focus of my specific research activity has been to evaluate a preliminary multi-temporal analysis of Sentinel-1 (S1) data for the monitoring of subsidence phenomena on two selected target: the Fiumicino Airport and the Brumadinho dam.

The third topic (section 5.3.1) can be considered complementary to the second one, not only in terms of technique and data used but also for the characteristic of the observed phenomenon. In fact, in this case, the suitability of space-borne SAR Sub-Pixel Offset Tracking (SPOT) technique using Cosmo-SkyMed products for the long-term monitoring of landslides in vegetated areas has been investigated. In particular, the case study of the Slumgullion landslide (Colorado, US) has been explored showing results in very good agreement with those provided in the past literature.

In order to properly frame the concepts, ideas and techniques developed within my research activities and presented in this thesis, some preliminary chapters about basic concepts of remote sensing and SAR have been inserted. For more details about the treated topics, the reader is referred to the quoted literature and in particular to [8].

This page intentionally left blank.

Chapter 2

Fundamentals

2.1 Synthetic Aperture Radar System Modes

In this paragraph the three standard SAR operating modes are briefly described. We refer to the stripmap, scanSAR and spotlight modes depicted in Figs. 2.1-2.2-2.3, respectively. For simplicity, they are addressed as *strip*, *scan* and *spot* in the following.

Among these, the strip mode is probably the most used. In this case, the antenna pattern points along a fixed direction with respect to the flight track in such a way that the antenna footprint covers a strip on the ground as the sensor moves. The dimension of the strip SAR images is limited in the across track (*range*) but not in the along track (*azimuth*) direction.

The scan mode is aimed at improving the range coverage at the expense of azimuth resolution. Indeed, in this case the antenna beam is periodically switched to illuminate neighboring subswaths by *bursts* shorter than the strip integration time. This determines a worsening in the azimuth resolution.

In opposite to the last one, the purpose of the spot mode is to improve the azimuth resolution. In this case, the antenna is steered during the

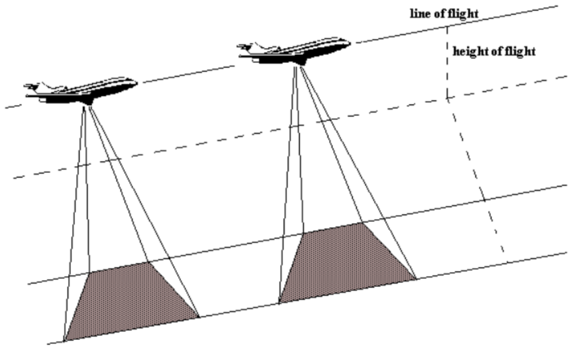

Figure 2.1. Stripmap SAR operation mode.

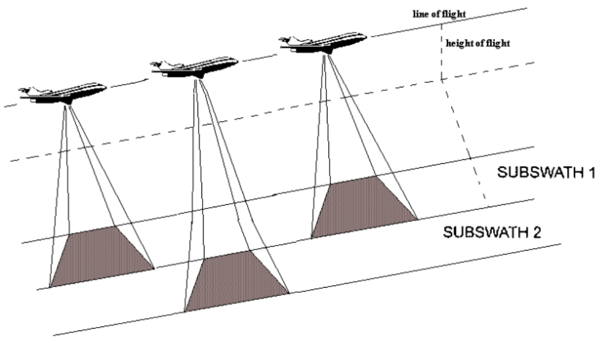

Figure 2.2. ScanSAR operation mode.

overall acquisition time to illuminate always the same area on the ground, causing an increase of the available synthetic antenna length. This gain is obviously traded off by loss of coverage due to the illumination of a limited scene along the azimuth direction.

To conclude this section, we annotate that there are others SAR acquisition techniques, each of which will be described in chapter 4.

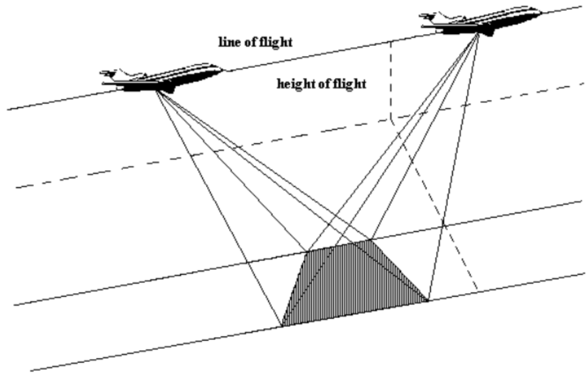

Figure 2.3. Spotlight SAR operation mode.

2.2 Geometric Resolution

The classic way to explain the geometric resolution of a SAR system is to starting from the strip mode. The basic geometric configuration, which naturally matches the *side-looking* radar operations, is shown in Fig. 2.4.

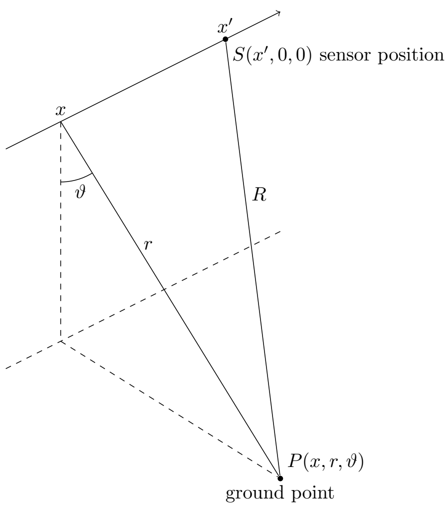

Figure 2.4. Cylindrical coordinate system (x, r, ϑ) for the strip SAR mode.

As mentioned before (see section 1), the *geometric resolution* is the minimum spacing between two objects that are detected as separated. When the resolution is properly computed, we can address the *resolution cell* in two (or three) dimensions. When we move to the discrete domain, due to the sampling signals, we define the *pixel spacing* that is the spacing between two consecutive samples.

2.2.1 Range

Let us consider a radar system transmitting electromagnetic pulses of time duration τ. So the sensor range resolution is

$$\Delta r = \frac{c\tau}{2}, \tag{2.1}$$

where c is the speed of light and factor 2 takes into account for the round-trip propagation.
The (2.1) can be also written as

$$\Delta r = \frac{c}{2\Delta f} \tag{2.2}$$

where $\Delta f \cong 1/\tau$ is the bandwidth of the pulse. Therefore, in order to improve the range resolution we have to transmit a pulse with a very short duration τ and, consequently, an high peak power. A method to overcome this limitation is to use modulated pulses.

The most popular pulse used in this context referred as *chirp*, having a linearly frequency modulated signal (Fig. 2.5)

$$f_1(t) = e^{j\left(\omega t + \frac{\alpha t^2}{2}\right)} \mathrm{rect}\left[\frac{t}{\tau}\right] \tag{2.3}$$

where ω is the angular frequency, α is the chirp rate related to the pulse bandwidth by $\alpha\tau \cong 2\pi\Delta f$.

If we assume the sensor to be located at $x = 0$, defining an associate

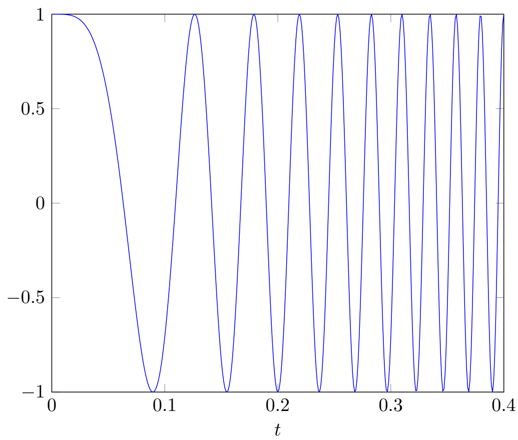

Figure 2.5. Chirp waveform for $\tau = 0.4s$ and $\alpha = 10^{-3}s^{-2}$.

plane orthogonal to the flight direction, and a target point $P \equiv (0, r, \vartheta)$ lying on it, the signal backscattered by it and received by the sensor is

$$f_1\left(t - \frac{2r}{c}\right) = e^{j\omega\left(t-\frac{2r}{c}\right)+j\frac{\alpha}{2}\left(t-\frac{2r}{c}\right)^2}\mathrm{rect}\left[\frac{t-2r/c}{\tau}\right] \tag{2.4}$$

which, after the demodulation, becomes as

$$f(t) = e^{-j\omega\frac{2r}{c}+j\frac{\alpha}{2}\left(t-\frac{2r}{c}\right)^2}\mathrm{rect}\left[\frac{t-2r/c}{\tau}\right] \tag{2.5}$$

Because of the spatial resolutions are of interest, we move towards the space coordinate $r' = ct/2$. Then, it is more convenient to define the following adimensional quantities

$$\begin{aligned} r &\rightarrow \frac{r}{c\tau/2} \\ r' &\rightarrow \frac{r'}{c\tau/2} \end{aligned} \tag{2.6}$$

Accordingly, the (2.5) becomes

$$f(r') = e^{-j\omega\tau r+j\frac{\alpha\tau^2}{2}(r'-r)^2}\mathrm{rect}\left[r'-r\right] \tag{2.7}$$

Convolving the received signal with the range reference function defined as

$$g(r') = e^{-j\frac{\alpha\tau^2}{2}r'^2}\mathrm{rect}\big[r'\big] \tag{2.8}$$

we obtain

$$\hat{f}(r') = e^{-j\omega\tau r}\mathrm{rect}\Big[\frac{r'-r}{2}\Big]\frac{\sin\big[\alpha\tau^2\big(r'-r\big)\big(1-|r'-r|\big)/2\big]}{\alpha\tau^2(r'-r)/2} \tag{2.9}$$

Assuming that $|r'-r| \ll 1$, we can rewrite the (2.9) as follows:

$$\begin{aligned}\hat{f}(r') &= e^{-j\omega\tau r}\mathrm{sinc}\Big[\tfrac{\alpha\tau^2}{2}\big(r'-r\big)\Big] \\ &= e^{-j\omega\tau r}\mathrm{sinc}\Big[\tfrac{\pi}{\Delta r}\big(r'-r\big)\Big]\end{aligned} \tag{2.10}$$

where

$$\Delta r = \frac{1}{\tau\Delta f} \tag{2.11}$$

By the (2.10) and (2.11) we discover that a point target located at r is imaged as a distributed object, represented by the *spread function* (Fig. 2.6) given by the equation (2.10). Δr represents the *normalized effective range dimension* of the target image.
In not-normalized units the (2.10) and (2.11) become, respectively,

$$\hat{f}(r') = e^{-j\frac{4\pi}{\lambda}r}\mathrm{sinc}\Big[\frac{\pi}{\Delta r}\big(r'-r\big)\Big] \tag{2.12}$$

and

$$\Delta r = \frac{c}{2\Delta f} = \frac{\lambda/2}{\Delta f/f} \tag{2.13}$$

where λ is the wavelength associated to the carrier frequency. According to

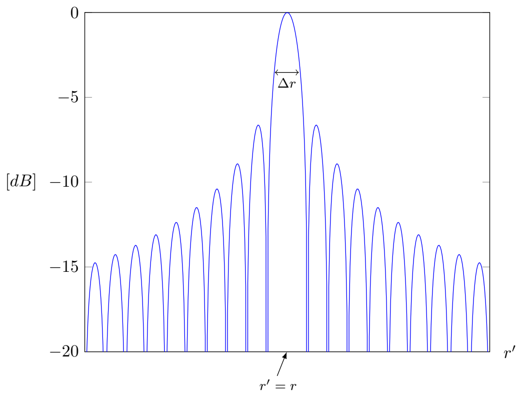

Figure 2.6. Point target spread function in range direction. The distance Δr is equal to the 3 dB range resolution. The vertical axis is expressed in decibel; the horizontal scale is in arbitrary units.

these last equations and to the system linearity, two point targets of equal amplitude located at $r = r_1$ and $r = r_2$, respectively, can be correctly resolved if $|r_2 - r_1| \geq \Delta r$ (Fig. 2.7). For this reason, Δr can be defined as the *(slant) range resolution* of the system.

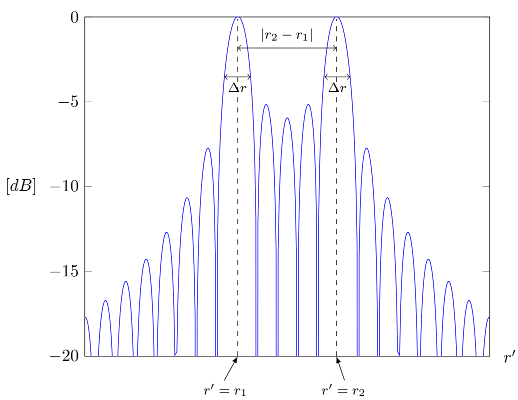

Figure 2.7. Superposition of the point spread functions of two target located at $r = r_1$ and $r = r_2$, respectively, with $|r_2 - r_1| > \Delta r$. The vertical axis is expressed in decibel; the horizontal scale is in arbitrary units.

In the case of a continuous distribution of targets described by *reflectivity pattern* $\gamma(r)$, proportional to the ratio between the backscattered and incident field, the processed signal is obtained by superposition and we have:

$$\hat{\gamma}(r') = \int \gamma(r)\hat{f}(r'-r)dr \tag{2.14}$$

2.2.2 Azimuth

Now we move to explore the capability of the sensor to resolve targets along the azimuth direction. As we can see in Fig. 2.8, two targets located at a certain range can be resolved only if they do not lies within the radar beam at the same time. So the azimuth resolution Δx can be expressed as

$$\Delta x \approx r\frac{\lambda}{L} \tag{2.15}$$

where r is the slant range and L is the physical antenna length along the azimuth direction.

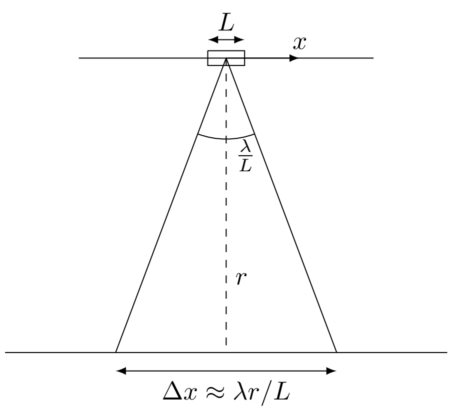

Figure 2.8. RAR azimuth resolution.

To improve the azimuth resolution we can reduce λ and/or increase L.

Both the ways are impracticable. The former is limited by the system characteristics. The latter is not an easy task when we want to launch these kind of systems in the space. Therefore, we have to implement the synthetic antenna concept shortly introduced in paragraph 1.

Let us assume the sensor working at an ideal mode, so called *start and stop*: in other words, the antenna transmits a pulse and receives the backscattered echo at the same position before it moves in another one along the flight direction. Consider $(2N+1)$ equally spaced positions of the sensor and a target point $T \equiv (0, r, \vartheta)$ located, for sick of simplicity, at the center of the scene illuminated by the real antenna at positions $S \equiv (x' = n'd, r = 0)$ with $n' = -N, ..., N$, as shown in Fig. 2.9.

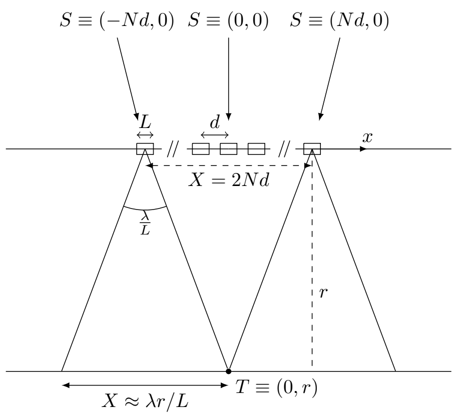

Figure 2.9. SAR array in the (x, r) plane.

In addition, we assume an isotropical radiation pattern within the main lobe of the antenna beam so that the length of the illuminated scene on the ground is

$$X \approx \frac{\lambda r}{L} \tag{2.16}$$

Hence, the signal received by the antenna (after the demodulation process) is given by

$$f(n'd) = e^{-j\omega\frac{2R}{c}} \approx e^{-j\left[\omega\frac{2r}{c}+\frac{2\pi}{\lambda r}(n'd)^2\right]} \tag{2.17}$$

where

$$R = \sqrt{r^2 + \left(n'd\right)^2} \approx r + \frac{\left(n'd\right)^2}{2r} \tag{2.18}$$

Neglecting the constant (with respect to the azimuth axis) factor $\exp(-j\omega 2r/c)$ in the (2.17), we can proceed to *synthesizing* an array antenna of length $2Nd = X$. As for the range case, we define the azimuth reference function

$$g(n'd) \approx e^{j\frac{2\pi}{\lambda r}(n'd)^2} \tag{2.19}$$

and we perform the convolution between it and the (2.17) obtaining that

$$\hat{f}(n'd) \approx 2N\frac{\sin\left(\frac{2\pi Xd}{\lambda r}n'\right)}{2N\sin\left(\frac{2\pi d^2}{\lambda r}n'\right)} \qquad n'd \ll X \tag{2.20}$$

Dividing all lengths by X in such a way that we use adimensional units, the equation (2.20) becomes

$$\hat{f}(x') \approx \frac{\sin\left(\frac{2\pi X^2}{\lambda r}x'\right)}{\frac{X}{d}\sin\left(\frac{2\pi Xd}{\lambda r}x'\right)} = \frac{\sin\left(\frac{2\pi X}{L}x'\right)}{\frac{X}{d}\sin\left(\frac{2\pi d}{L}x'\right)} \tag{2.21}$$

where $x' = n'd/X$. As for the range case, the equation (2.21) reveals that the image of the point target at $x = 0$ spreads along the azimuth direction. For $d/L \ll 1$, we can approximate the sine function at the denominator of the (2.21) by its argument and we have that

$$\hat{f}(x') \approx \sin\left(\frac{2\pi X}{L}x'\right) = \sin\left(\frac{\pi}{\Delta x}x'\right) \tag{2.22}$$

where

$$\Delta x = \frac{L}{2X} \tag{2.23}$$

represents the *normalized azimuth resolution* which becomes in not-normalized units:

$$\Delta x = \frac{L}{2} \tag{2.24}$$

The (2.24) shows that smaller the antenna, better the resolution. This result is in opposite to our intuition, but it is simply explained noticing that a decrease of L implies an increase of X and, accordingly, a larger number of elements of the synthetic array. As for the range case, distributed targets are taken into account by superposition obtaining

$$\hat{\gamma}(x') = \int \gamma(x)\hat{f}(x' - x)dx \tag{2.25}$$

Finally, by combining the equations (2.14) and (2.25) we have the overall SAR image expression:

$$\hat{\gamma}(x', r') = \iint \gamma(x, r)\mathrm{sinc}\Big[\frac{\pi}{\Delta x}\big(x' - x\big)\Big]\mathrm{sinc}\Big[\frac{\pi}{\Delta r}\big(r' - r\big)\Big]dxdr \tag{2.26}$$

where $\gamma(x, r)$ represents the two-dimensional (2D) reflectivity pattern of the scene, including the phase factor $\exp\big(-j\omega\tau r\big)$ of the (2.14).

2.3 Geometric Distortions

In many applications (such as, land cover mapping, geology studies, etc.), the SAR images computed in the sensor coordinates (i.e., slant range and azimuth) are not useful because of the presence of geometric distortions proper of the “range” imaging mode.

To clarify this aspect let us assume the geometry in Fig. 2.10 where S

represents the sensor moving along the azimuth direction perpendicular to the page. In addition, let us consider the simple case of a totally flat scene on the ground. It is obvious that a constant slant resolution Δr does not correspond to a constant resolution Δy on the ground, let us call it *ground resolution*. In fact, we have that

$$\Delta y = \frac{\Delta r}{\sin \vartheta} \tag{2.27}$$

where the variation of the incidence angle ϑ from the near range to the far range results in a decrease of Δy.

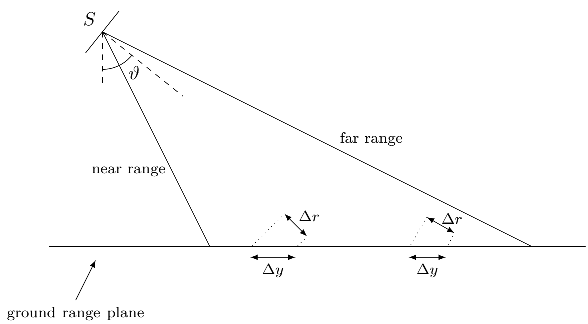

Figure 2.10. Slant range vs. ground range resolutions.

Therefore, if we consider a surface slope α, the ground resolution depends on the local incidence angle $\vartheta_i = \vartheta - \alpha$ and three cases are possible:

- *Foreshortening* $(-\vartheta < \alpha < \vartheta)$: it causes an expansion, if $0 < \alpha < \vartheta$ (Fig. 2.11-(a)), or compression, if $-\vartheta < \alpha < 0$ (Fig. 2.11-(b)) of Δy
- *Layover* $(\alpha \geq \vartheta)$: it determines an inversion of the image geometry. As we can see in Fig. 2.12-(a), peaks of mountains with a steep slope switch to their bases in the slant range, causing a severe image distortion. In particular, for $\alpha = \vartheta$ the area with this slope is compressed into a single pixel.

- *Shadow* ($\alpha \leq \vartheta - \pi/2$): in this case there is no backscattered contribution to the image (Fig. 2.12-(b)).

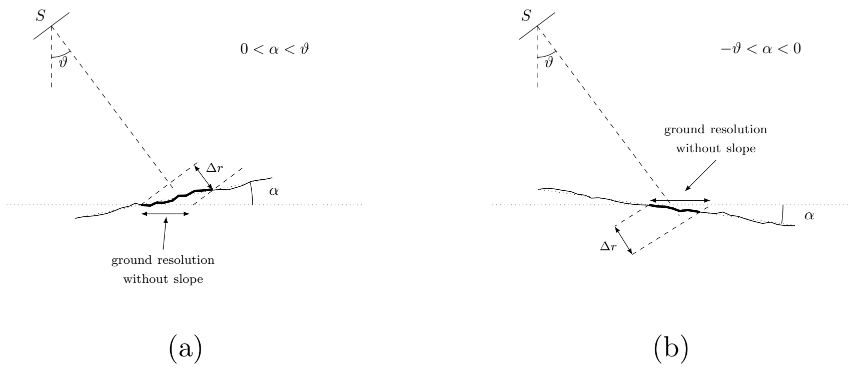

Figure 2.11. Foreshortening effect: the ground resolution is highlighted for (a) $0 < \alpha < \vartheta$ and (b) $-\vartheta < \alpha < 0$.

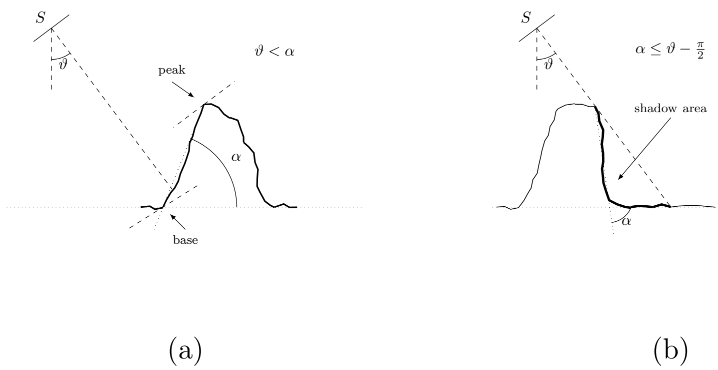

Figure 2.12. Layover (a) and shadow (b) effects.

2.4 Ambiguity Problems

In this section, we want to explore constraints related to the distance between successive positions of the transmit and receive antenna.

Range ambiguities arise if different backscattered pulses, one relative to a transmitted pulse and other due to a previous transmission, overlap during the receiving time. Let us define P'_n and P_n the range ambiguous and not-ambiguous signal power, respectively, during the n-interval of the data recording window. Therefore, we can define the *range ambiguity to signal ratio* (RASR) as

$$RASR = \frac{\sum_{n=0}^{N-1} P'_n}{\sum_{n=0}^{N-1} P_n} \tag{2.28}$$

where N is the number of intervals. In order to overcome this ambiguity, we have to choose a proper value for the *pulse repetition frequency* (PRF):

$$f_p = \frac{1}{T} \tag{2.29}$$

being T the time interval from a pulse to another one. An upper bound on the PRF is set at the aim to avoid that successive backscattered pulses are received at the same time. So, the time extension of each pulse has to be smaller than the interval between two successive pulses. For the geometry of Fig. 2.13 this constraints leads to

$$T \geq \frac{2\Delta W}{c} \Leftrightarrow f_p \leq \frac{c}{2\Delta W} \tag{2.30}$$

where

$$\Delta W \approx \frac{r\lambda}{L_r} \tan\vartheta \tag{2.31}$$

is the slant range projection of the illuminated area and L_r is the antenna length orthogonal to the azimuth and the pointing direction.

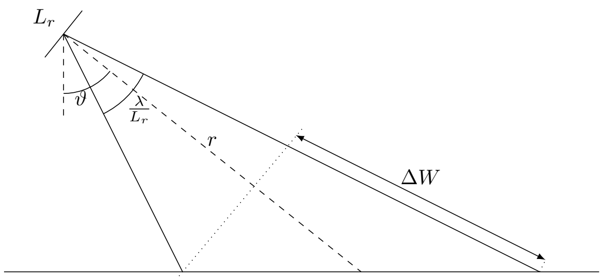

Figure 2.13. Slant range swath extension ΔW.

As for the range case, we can define an *azimuth ambiguity to signal ratio* (AASR) [9] in order to take into account for the *azimuth ambiguities.* In particular, they can occur in the presence of *grating lobes* [10]. To avoid these effects, a lower bound on the PRF is necessary:

$$T = \frac{d}{v} \leq \frac{L}{2v} \Leftrightarrow f_p \geq \frac{2v}{L} \tag{2.32}$$

where L is the azimuth antenna length. The equations (2.30) and (2.32) can be unified, obtained

$$\frac{2v}{L} \leq f_p \leq \frac{c}{2\Delta W} \tag{2.33}$$

which can satisfy if

$$\frac{2v}{L} \leq \frac{c}{2r\lambda \tan\vartheta / L_r} \Leftrightarrow LL_r \geq 4\frac{v}{c} r\lambda \tan\vartheta \tag{2.34}$$

leading to the conclusion that sensor parameters set a constraint to the antenna area LL_r.

This page intentionally left blank.

Chapter 3

Strip Mode Transfer Function and Data Processing

3.1 Signal Analysis in Time and Frequency Domain

Let us consider the coordinate system (x, r, ϑ) in Fig. 3.1, where the x-axis is coincident with the sensor trajectory assumed to be a straight line. The SAR sensor moves at constant velocity $\boldsymbol{v} = v\hat{\boldsymbol{x}}$. At time $t_n - \tau/2$, the sensor transmits pulses given by

$$f_1(t) = e^{j\omega t} P(t - t_n) \mathrm{rect}\left[\frac{t - t_n}{\tau}\right] \tag{3.1}$$

where $P(t - t_n)$ represents the signal modulation and τ is the duration of the transmitted pulse. If we use the *chirp* modulation described in section 2.2.1, we have that

$$P(t - t_n) = e^{j\frac{\alpha}{2}(t-t_n)^2} \tag{3.2}$$

where α is the chirp rate. For $\alpha\tau^2 \gg 1$, that is the case for the SAR

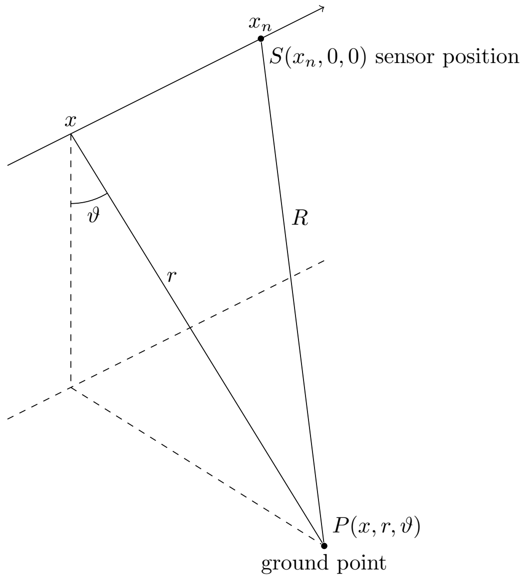

Figure 3.1. Cylindrical coordinate system geometry.

systems, we have $\alpha\tau \approx 2\pi\Delta f$, Δf being the chirp bandwidth. Anyway, a more general analysis is now in order and we do not consider any particular choice for $P(\cdot)$.

Let us consider the elementary scattered point at $P(x, r, \vartheta)$ (see Fig. 3.1). The signal backscattered and received by the sensor, after the demodulation process, is

$$\begin{aligned} f(x_n - x, t_n - t, r) &= e^{-j\omega\frac{2R}{c}} P\Big(t - t_n - \tfrac{2R}{c}\Big) \\ &\quad \mathrm{rect}\Big[\tfrac{t - t_n - \frac{2R}{c}}{\tau}\Big] w^2\big[x_n - x, r\big] \end{aligned} \tag{3.3}$$

where $x_n = vt_n$ is the coordinate of the antenna phase center, and

$$R = \sqrt{r^2 + (x_n - x)^2} \tag{3.4}$$

is the relative distance from the target to the sensor. The antenna footprint over the ground is represented by the ground illumination function $w[\cdot]$ which is related to the antenna gain.

It is worthwhile to specify that the equation (3.3) is obtained assuming the sensor moves in a *stop and go* way. That is, the system transmits a pulse and receive it at the same position. Of course, this is not the real situation. In fact, the system receives the transmitted pulse at a slightly different position due to the platform moving during the transmit and receive mode. For this reason, in the (3.3) we should substitute R by

$$\begin{aligned} R' &\approx \tfrac{1}{2}\sqrt{r^2 + (x_n - x)^2} + \tfrac{1}{2}\sqrt{r^2 + (x_n - x - \tfrac{2vR'}{c})^2} \\ &\approx R - \tfrac{v}{c}(x_n - x) \end{aligned} \tag{3.5}$$

The correction term is of order v/c and it is neglected in the following.

As in section 2.2.1, the time coordinates can be changed in range coordinates using the transformation

$$r' = \frac{ct'}{2} \tag{3.6}$$

with

$$t' = t - t_n \tag{3.7}$$

Moreover, considering

$$\Delta R = R - r = \sqrt{r^2 + (x_n - x)^2} - r \tag{3.8}$$

assuming the discrete x_n-coordinate to be continuous (see section 2.2.2), $x_n \to x'$, and normalizing r' and r to one half of the pulse spatial extension $c\tau/2$, we can rewrite the (3.3) as follows:

$$
\begin{aligned}
f(x'-x,r',r) \;&=\; e^{-j\frac{4\pi r}{\lambda}} e^{-j\frac{4\pi \Delta R}{\lambda}} P\Big(r'-(r+\Delta R)\Big) \\
&\quad\ \mathrm{rect}\left[\frac{r'-(r+\Delta R)}{c\tau/2}\right] w^2\left[x'-x,r\right]
\end{aligned} \tag{3.9}
$$

In addition, we have normalized x', x and ΔR in the (3.9), to the mid-swath azimuth illumination footprint X (see 3.2) given by

$$X \approx \lambda r_0/L \tag{3.10}$$

which is a conventional footprint, because the side lobes of the real antenna are included in the $w[\cdot]$ function definition. L is the azimuth effective length of the real antenna and r_0 is the closest range distance between the sensor and center of the footprint. As we can notice, X depends on the real antenna angular resolution $\Delta\theta \approx \lambda/L$.

The aforementioned normalization is understood from now on, although we do not change the symbols already used for the not-normalized quantities. By the superposition of all the elementary points backscattered from

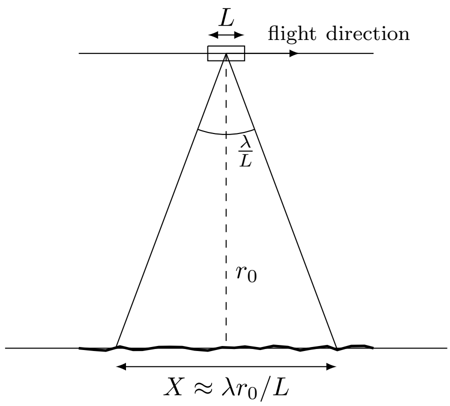

Figure 3.2. Acquisition geometry in the (x, r) plane.

the illuminated scene, we obtain the raw signal $h(x', r')$ from the (3.9):

$$\begin{aligned} h(x', r') &= \iint \gamma(x, r) e^{-j2\pi \frac{c\tau}{2} r} e^{-j4\pi \frac{X}{\lambda} \Delta R} P\Big(r' - r - \tfrac{2X}{c\tau}\Delta R\Big) \\ &\quad \mathrm{rect}\Big[r' - r - \tfrac{2X}{c\tau}\Delta R\Big] w^2\big[x' - x, r\big] dx dr \end{aligned} \tag{3.11}$$

where $\gamma(x, r)$ is the surface reflectivity pattern and

$$\Delta R = \sqrt{\left(\frac{c\tau}{2X} r\right)^2 + (x' - x)^2} - \frac{c\tau}{2X} r \tag{3.12}$$

The amplitude factors X and $c\tau/2$ due to the normalization of the differentials dx and dr, respectively, have been neglected in the (3.11). This latter equation can be rewrite in a more compact form:

$$h(x', r') = \iint \gamma(x, r) g(x' - x, r' - r, r) dx dr \tag{3.13}$$

where the following definitions are made:

$$\gamma(x, r) \rightarrow \gamma(x, r) e^{-j2\pi \frac{c\tau}{2} r} \tag{3.14}$$

that is the new reflectivity pattern, and

$$\begin{aligned} g(x' - x, r' - r, r) &= e^{-ja \frac{2L}{\lambda} \Delta R} P\Big(r' - r - \tfrac{2X}{c\tau}\Delta R\Big) \\ &\quad \mathrm{rect}\Big[r' - r - \tfrac{2X}{c\tau}\Delta R\Big] w^2\big[x' - x, r\big] \end{aligned} \tag{3.15}$$

represents the *impulse response* of the system, that is the return due to the *unitary point target*, dependent on the electrical, cinematic and geometry parameters of the SAR system, and

$$a = \pi \frac{X}{L/2} \tag{3.16}$$

We can notice that the additional phase factor $\exp(-j2\pi c\tau r/\lambda)$, which should be take into account in the definition of the unitary point target (3.15), has been coupled into the reflectivity function (3.14).

The (3.13) is the basic functional form of the SAR system raw signal. In fact, it shows the relationship between the *recorded raw signal*, $h(\cdot)$, the *reflectivity pattern*, $\gamma(\cdot)$, and the *SAR system impulse response*, $g(\cdot)$. Therefore, the equation (3.13) allows to manage the SAR imaging problem through a proper filter operation that gives an estimate of $\gamma(\cdot)$ (let us call it $\hat{\gamma}(\cdot)$) starting from the received signal $h(\cdot)$.

Finally, if the explicit r-dependence of $g(\cdot)$ can be neglected, $g(x'-x, r'-r, r) \rightarrow g(x'-x, r'-r)$, we have

$$h(x', r') \rightarrow \iint \gamma(x, r) g(x'-x, r'-r) dx dr = \gamma(x', r') \otimes g(x', r') \quad (3.17)$$

that is the 2D convolution between the reflectivity pattern and the SAR system impulse response. Anyway, we highlight that the simplification leading to the (3.17) is not allowed in general. For this reason, the r-dependence of $g(\cdot)$ requires special care when SAR data processing operations are implemented (see from section 3.3 to 3.5).

In order to perform the analysis in the frequency domain, obtaining the *SAR transfer function*, we have to consider the 2D Fourier Transform (2D-FT) of $h(\cdot)$:

$$\begin{aligned} H(\xi, \eta) &= \iint h(x', r') e^{-j\xi x'} e^{-j\eta r'} dx' dr' \\ &= \iint \gamma(x, r) \iint g(x'-x, r'-r, r) e^{-j\xi x'} e^{-j\eta r'} dx' dr' dx dr \\ &= \iint \gamma(x, r) e^{-j\xi x} e^{-j\eta r} G(\xi, \eta, r) dx dr \end{aligned} \quad (3.18)$$

where $G(\cdot)$ is the SAR system Transfer Function (TF), that is, the 2D-FT of the impulse response $g(\cdot)$

$$G(\xi,\eta,r)=\iint g(x'-x,r'-r,r)e^{-j\xi(x'-x)}e^{-j\eta(r'-r)}dx'dr' \tag{3.19}$$

If the r-dependence of the $G(\cdot)$ can be neglected, the (3.18) becomes

$$\begin{aligned} H(\xi,\eta) &= \textstyle\iint \gamma(x,r)e^{-j\xi x}e^{-j\eta r}G(\xi,\eta)dxdr \\ &= \Gamma(\xi,\eta)G(\xi,\eta) \end{aligned} \tag{3.20}$$

where $\Gamma(\cdot)$ is the 2D-FT of the $\gamma(\cdot)$. The result in (3.20) is consistency with the equation (3.17) and it is in according to the FT properties.

The analysis of $G(\cdot)$ is now in order. If we consider

$$\begin{aligned} p &= x'-x \\ q &= r'-r-\tfrac{2X}{c\tau}\Delta R \end{aligned} \tag{3.21}$$

the (3.19) becomes

$$G(\xi,\eta,r)=\int w^2[p,r]e^{-j\Psi_1(p)}dp\int P[q]\mathrm{rect}[q]e^{-j\eta q}dq \tag{3.22}$$

where

$$\Psi_1(p)=\xi p+2a\frac{L}{\lambda}\Delta R+\eta\frac{2X}{c\tau}\Delta R=\xi p+2a\frac{L}{\lambda}\Delta R\Big(1+\eta\frac{\varepsilon}{2\pi\Delta f\tau}\Big) \tag{3.23}$$

with

$$\Delta R=\sqrt{\Big(\frac{c\tau}{2X}r\Big)^2+p^2}-\frac{c\tau}{2X}r \tag{3.24}$$

and

$$\varepsilon = \frac{2\pi\Delta f}{\omega} = \frac{\Delta f}{f} \tag{3.25}$$

Δf being the transmitted signal bandwidth. The q-integral in the (3.22) is the FT of the transmitted signal and it is valid for any waveform $P(\cdot)$. Therefore, for a chirp modulation, the impulse response $g(\cdot)$ and the TF $G(\cdot)$ become, respectively,

$$\begin{aligned} g(x'-x, r'-r, r) \;=\;& e^{-ja\frac{2L}{\lambda}\Delta R} e^{jb\left(r'-r-\frac{2X}{c\tau}\Delta R\right)^2} \\ & \mathrm{rect}\Big[r'-r-\tfrac{2X}{c\tau}\Delta R\Big] w^2\big[x'-x, r\big] \end{aligned} \tag{3.26}$$

and

$$G(\xi,\eta,r) = \int w^2[p,r] e^{-j\Psi_1(p)} dp \int \mathrm{rect}[q] e^{-j\Psi_2(q)} dq \tag{3.27}$$

with

$$\Psi_2(q) = \eta q - bq^2 \tag{3.28}$$

$$\Psi_1(p) = \xi p + 2a\frac{L}{\lambda}\Delta R\Big(1 + \varepsilon\frac{\eta}{2b}\Big) \tag{3.29}$$

and

$$b = \alpha\frac{\tau^2}{2} = \pi\Delta f\tau \tag{3.30}$$

Investigation of the $w(\cdot)$ illumination function is now in order. As in section 3.1, it is useful to normalize x', x and ΔR to the azimuth footprint at the center of the illuminated scene. But this swath changes during the pulse because the instantaneous angular frequency $(\omega + \alpha t')$ changes too. In fact, if ω changes also the wavenumber $\omega/c = 2\pi/\lambda$ changes and, accordingly, the azimuth beamwidth λ/L changes. It can be noted that ω (Fourier mate of t') is related to η (Fourier mate of r'). If we assume

$$\eta_0 = \frac{\omega}{c}\frac{c\tau}{2} = \pi f \tau = \pi \frac{b}{\varepsilon} \tag{3.31}$$

the value of the normalized wavenumber at time $t' = 0$, the correct expression of the angular beamwidth as the chirp pulse elaspses is

$$\Delta\vartheta \approx \frac{2\pi}{L}\frac{c\tau}{2\eta_0\left(1+\frac{\eta}{2\eta_0}\right)} = \frac{2\pi}{L}\frac{c\tau}{2\eta_0\left(1+\varepsilon\frac{\eta}{2b}\right)} = \frac{\lambda}{L}\frac{1}{1+\varepsilon\frac{\eta}{2b}} \tag{3.32}$$

Therefore, using the (3.32), the $w(\cdot)$ function in normalized units becomes:

$$w[p,r] \approx w\left[\frac{\eta}{r\Delta\vartheta/x}\right] = w\left[\frac{p}{r/r_0}\left(1+\varepsilon\frac{\eta}{2b}\right)\right] \tag{3.33}$$

where the terms r/r_0 and $(1+\varepsilon\eta/2b)$ take into account for the range-space and the range-frequency dependence of the illumination footprint, respectively.

Analysing the equation (3.27), we can notice that a fast varying phase term is present in both the integrals (see equations (3.28) and (3.29)). Indeed, the 2D parameters a and b are very large realistically for all SAR systems. Therefore, the *stationary phase method* can be applied to the (3.27), leading to the asymptotic closed form solution for the TF, whose the relative error is on the order of $1/a$ and $1/b$ for the p-integral and the q-integral in (3.27), respectively [11]. So we get

$$G(\xi,\eta,r) \sim \frac{1}{\sqrt{|\Psi_1''(p_s)||\Psi_2''(q_s)|\big/(2\pi)^2}} w^2\left[\frac{p_s}{r/r_0}\left(1+\varepsilon\frac{\eta}{2b}\right)\right]e^{-j\Psi_1(p_s)}$$
$$\mathrm{rect}[q_s]e^{-j\Psi_2(q_s)} \tag{3.34}$$

where the stationary phase points q_s and p_s are solutions of the following equations:

$$\Psi_2'(q_s) = \left.\frac{d\Psi_2(q)}{dq}\right|_{q_s} = \eta - 2bq_s = 0 \Rightarrow q_s = \frac{\eta}{2b} \tag{3.35}$$

and

$$\Psi_1'(p_s) = \left.\frac{d\Psi_1(p)}{dp}\right|_{p_s} = \xi + 2a\frac{L}{\lambda}\left(1+\varepsilon\frac{\eta}{2b}\right)\frac{p_s}{R_s} = 0 \tag{3.36}$$

respectively, and R_s is the value of R at the stationary point p_s

$$R_s = \sqrt{\left(\frac{c\tau}{2X}r\right)^2 + p_s^2} \tag{3.37}$$

Applying the results of (3.28) and (3.35) in the q_s-dependent part of the 3.34 we get

$$\mathrm{rect}[q_s]e^{-j\Psi_2(q_s)} = \mathrm{rect}[\frac{\eta}{2b}]e^{-j\frac{\eta^2}{4b}} \tag{3.38}$$

In order to calculate the stationary point p_s, we substitute the (3.37) into the (3.36) and solve it for p_s obtaining

$$p_s = -\frac{\frac{r}{r_0}\xi}{\sqrt{(2a)^2\left(1+\varepsilon\frac{\eta}{2b}\right)^2 - \left(\frac{\lambda}{L}\xi\right)^2}} \tag{3.39}$$

This value is used to compute $\Delta R_s = \Delta R(p_s)$. In fact, setting $p = p_s$ into the (3.24) and using the (3.39) we have

$$\Delta R_s = \frac{r}{r_0}\sqrt{\frac{\xi^2}{(2a)^2\Big(1+\varepsilon\frac{\eta}{2b}\Big)^2 - \Big(\frac{\lambda}{L}\xi\Big)^2} + \Big(\frac{L}{\lambda}\Big)^2} - \frac{c\tau}{2X}r \tag{3.40}$$

Finally, substitution of (3.39) and (3.40) into the (3.29) leads us to

$$\Psi_1(p_s) = 2a\Big(\frac{L}{\lambda}\Big)^2\Big(1+\varepsilon\frac{\eta}{2b}\Big)\frac{r}{r_0} + \frac{L}{\lambda}\frac{r}{r_0}\sqrt{\Big(2a\frac{L}{\lambda}\Big)^2\Big(1+\varepsilon\frac{\eta}{2b}\Big)^2 - \xi^2} \tag{3.41}$$

In order to conclude the evaluation of the TF, we need to compute the function $w^2(\cdot)$ at the stationary point. If we do this, we have

$$w^2\Big[\frac{p_s}{r/r_0}\Big(1+\varepsilon\frac{\eta}{2b}\Big)\Big] \approx w^2\Big[-\frac{\xi}{2a}\Big] \tag{3.42}$$

where we use the first term only in the series expansion of the square root of the equation (3.39). Therefore, by substituting the equations (3.38), (3.41) and (3.42) into the (3.34) we get the overall expression of the SAR TF:

$$\begin{aligned} G(\xi,\eta,r) &\sim \frac{\pi}{\sqrt{a(r_0/r)b}}\mathrm{rect}\Big[\frac{\eta}{2b}\Big]w^2\Big[-\frac{\xi}{2a}\Big]e^{-j\Psi(\xi,\eta,r)} \\ &\approx \frac{\pi}{\sqrt{ab}}\mathrm{rect}\Big[\frac{\eta}{2b}\Big]w^2\Big[-\frac{\xi}{2a}\Big]e^{-j\Psi(\xi,\eta,r)} \end{aligned} \tag{3.43}$$

with

$$\begin{aligned} \Psi(\xi,\eta,r) = &\frac{\eta^2}{4b} - 2a\Big(\frac{L}{\lambda}\Big)^2\Big(1+\varepsilon\frac{\eta}{2b}\Big)\frac{r}{r_0} + \\ &+\frac{L}{\lambda}\frac{r}{r_0}\sqrt{\Big(2a\frac{L}{\lambda}\Big)^2\Big(1+\varepsilon\frac{\eta}{2b}\Big)^2 - \xi^2} \end{aligned} \tag{3.44}$$

Some considerations on the TF are now in order. For first, if we consider a uniform illumination pattern over the ground, that means

$$w^2\left[-\frac{\xi}{2a}\right] \approx \mathrm{rect}\left[\frac{\xi}{2a}\right] \tag{3.45}$$

we have that the $G(\cdot)$ TF is a function band limited (see Fig. 3.3) to the spectral interval given by:

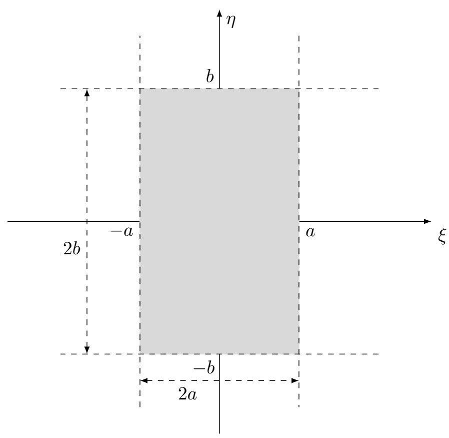

Figure 3.3. 2D signal spectrum domain for a boresight geometry.

$$\begin{aligned} -a \le \xi \le a \\ -b \le \eta \le b \end{aligned} \tag{3.46}$$

Denormalization of the azimuth spatial bandwidth $2a/2\pi$ provides us the relative frequency bandwidth

$$\frac{2a}{2\pi} \rightarrow \frac{2v}{L} \tag{3.47}$$

which is often interpreted as Doppler bandwidth.

Let us now study the square root term appearing in the (3.44). Because of the bounds for ξ provide the second factor in the square root much smaller than the first one, we can perform a Taylor series expansion around $\xi = 0$ obtaining

$$\sqrt{\left(2a\frac{L}{\lambda}\right)^2\left(1+\varepsilon\frac{\eta}{2b}\right)^2-\xi^2} \approx 2a\frac{L}{\lambda}\left(1+\varepsilon\frac{\eta}{2b}\right)-\frac{\xi^2\lambda L}{4a\left(1+\varepsilon\frac{\eta}{2b}\right)} \tag{3.48}$$

and the TF phase term assumes a more manageable form:

$$\Psi(\xi,\eta,r) \approx \frac{\eta^2}{4b}-\frac{\xi^2}{4a\frac{r_0}{r}\left(1+\varepsilon\frac{\eta}{2b}\right)} = \frac{\eta^2}{4b}-\frac{\xi^2}{4a'\left(1+\varepsilon\frac{\eta}{2b}\right)} = \tag{3.49}$$

with

$$a' = a\frac{r_0}{r} \tag{3.50}$$

which, if we pass to the not-normalized units, becomes equal to

$$a' \to \frac{2v^2}{\lambda r} \tag{3.51}$$

usually referred to as *Doppler rate* [9, 12, 13]. As we can notice, the series expansion in the (3.48) corresponds to the parabolic approximation (as depicted in Fig. 3.4) of the sensor-target distance (equation (3.4))

$$R = \sqrt{r^2+(x'-x)^2} \approx r + \frac{(x'-x)^2}{2r} \tag{3.52}$$

Despite the previously approximation leading to the equation (3.49), this can not be factorized in the product of two terms, each one depending on ξ and η only. This is possible if we use a further approximation, that is to neglect the coupling factor $\varepsilon\eta/2b$. In this case, the TF becomes the product of the spectra of two Frequency Modulation (FM) chirps

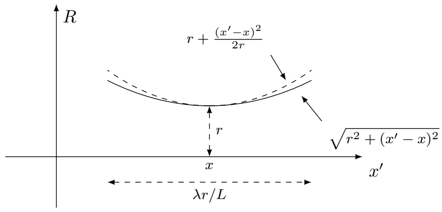

Figure 3.4. Sensor-target distance variation for a boresight geometry.

$$G(\xi, \eta, r) \approx \operatorname{rect}\left[\frac{\eta}{2b}\right] e^{-j\frac{\eta^2}{4b}} \operatorname{rect}\left[\frac{\xi}{2a}\right] e^{j\frac{\xi^2}{4a'}} \tag{3.53}$$

The η-dependent factor is the spectrum of the transmitted chirp. The ξ-dependent factor lies on the relative sensor-target motion and take into account for an r-dependent rate.

3.2 Squinted Geometry

The SAR systems antenna beam is generally pointed along the direction perpendicular to the flight path. In some cases, the antenna can be present an offset pointing angle, also known as *squint angle*, due to the platform instabilities [14–16] or to an intentional steering operation [17–19].

Let us consider the squinted SAR geometry of Fig. 3.5, where ϕ is the squint angle and S is the sensor position. In this section, we want to find the relationship between ϕ and the platform attitude angles, also known as *pitch* (ϑ_P), *yaw* (ϑ_Y) and *roll* (ϑ_R) [3, 20] (Fig. 3.6). More precisely, only the first two angles determine the squint offset. In fact, ϑ_R changes the antenna orientation in the plane orthogonal to the flight direction.

If the squint is absent, the unit vector in the boresight direction is

$$\hat{\boldsymbol{r}}_{\boldsymbol{\vartheta}} = -\sin\vartheta\hat{\boldsymbol{y}} - \cos\vartheta\hat{\boldsymbol{z}} \tag{3.54}$$

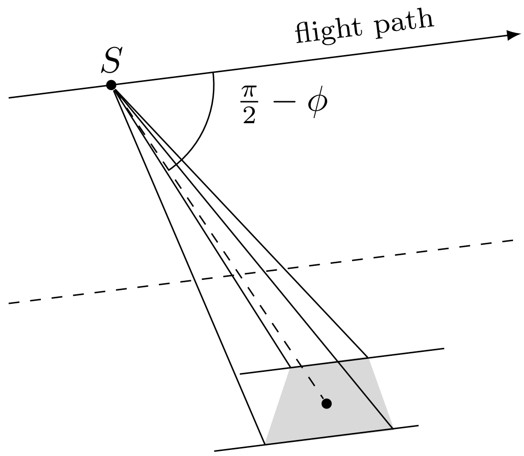

Figure 3.5. Strip mode illumination geometry in presence of a squint angle ϕ relative to the center of the scene.

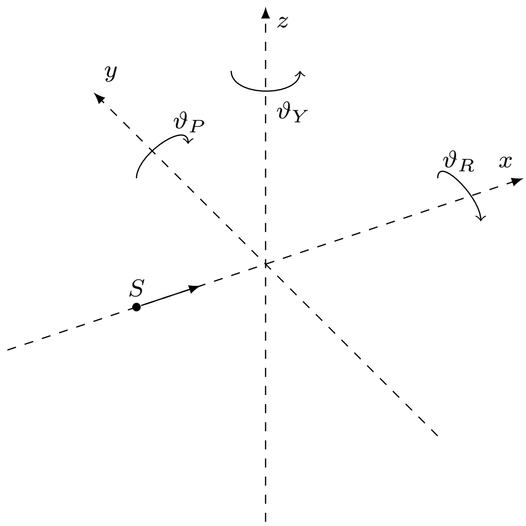

Figure 3.6. Roll (ϑ_R), pitch (ϑ_P) and yaw (ϑ_Y) angles.

If the shuttle rotates of ϑ_Y, $\hat{\boldsymbol{r}}_{\boldsymbol{\vartheta}}$ rotates too, and a new spatial position r'_ϑ

is obtained, with an x-component given by

$$\boldsymbol{r}'_{\boldsymbol{\vartheta}} \cdot \hat{\boldsymbol{x}} = -\sin\vartheta \sin\vartheta_Y \tag{3.55}$$

Therefore, the squint angle is

$$\phi = \frac{\pi}{2} - \cos^{-1}(\hat{\boldsymbol{x}} \cdot \hat{\boldsymbol{r}}'_{\boldsymbol{\vartheta}}) = \sin^{-1}(\sin\vartheta \sin\vartheta_Y) \tag{3.56}$$

In the same way, for the ϑ_P rotation we have

$$\phi = -\sin^{-1}(\cos\vartheta \sin\vartheta_P) \tag{3.57}$$

As we can see by the equations (3.56) and (3.57), ϕ depends on ϑ and this determines an its variation from the near to the far range.

The squint angle causes a changing in the TF. In fact, under the hypotheses of transmitting a chirp pulse and proceeding in the same way of the previous sections, we have

$$\begin{aligned} f(x_n - x, t', r) &= e^{-j\frac{4\pi r}{\lambda}} e^{-j\frac{4\pi\Delta R}{\lambda}} e^{j\frac{\alpha}{2}\left(t' - 2\frac{r+\Delta R}{c}\right)^2} \\ &\quad \mathrm{rect}\left[\tfrac{t' - 2(r+\Delta R)/c}{\tau}\right] w^2\left[x_n - x + r\tan\phi, r\right] \end{aligned} \tag{3.58}$$

This means that in presence of a squint angle the point target is at the center of the antenna beam only if $x - x_n = r\tan\phi$ (see Fig. 3.7).

Regarding the TF expression, we get

$$G(\xi, \eta, r) = \int w^2\left[p + \frac{c\tau}{2X} r\tan\phi, r\right] e^{-j\Psi_1(p)} dp \int \mathrm{rect}[q] e^{-j\Psi_2(q)} dq \tag{3.59}$$

where p and q are the same as in (3.21) and $x_n = x'$. Starting from the (3.33) for not-normalized units we get

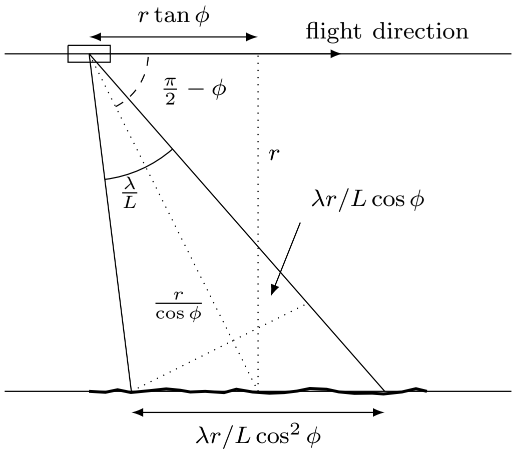

Figure 3.7. Squinted acquisition geometry in the (x, r) plane.

$$w[p + r\tan\phi, r] \approx w\left[\frac{p + r\tan\phi}{\frac{\lambda}{L}\frac{r}{\cos^2\phi}\left(1+\varepsilon\frac{\eta}{2b}\right)^{-1}}\right] \tag{3.60}$$

where $\lambda r/L\cos^2\phi$ is the azimuth illumination footprint on the ground (see Fig. 3.7).

The $G(\cdot)$ function in (3.59) is equal to the (3.27), except for the argument of $w(\cdot)$ function, which does not play any roles in the application of the stationary phase method. For this reason, we can write

$$G(\xi,\eta,r) \approx \mathrm{rect}\left[\frac{\eta}{2b}\right] w^2\left[\frac{2a\left(1+\varepsilon\frac{\eta}{2b}\right)\frac{L}{\lambda}\sin\phi - \xi}{2a\cos\phi}\right] e^{-j\Psi(\xi,\eta,r)} \tag{3.61}$$

If we use the same approximation of the equation (3.42) and consider small squint angle ($\cos\phi \approx 1$), we obtain

$$
\begin{aligned}
w^2\left[\frac{2a\left(1+\varepsilon\frac{\eta}{2b}\right)\frac{L}{\lambda}\sin\phi-\xi}{2a\cos\phi}\right] &\approx \operatorname{rect}\left[\frac{2a\left(1+\varepsilon\frac{\eta}{2b}\right)\frac{L}{\lambda}\sin\phi-\xi}{2a\cos\phi}\right] \\
&\approx \operatorname{rect}\left[\frac{\xi-2a\chi}{2a}\right]
\end{aligned}
\tag{3.62}
$$

where

$$
\chi = \left(1+\varepsilon\frac{\eta}{2b}\right)\frac{L}{\lambda}\sin\phi \approx \frac{L}{\lambda}\sin\phi \tag{3.63}
$$

The (3.62) shows that the ξ-component of the spectrum is still band limited but now its central spatial frequency ξ_d is ϕ-dependent (Fig. 3.8)

$$
\xi_d = 2a\chi \approx 2a\frac{L}{\lambda}\sin\phi \tag{3.64}
$$

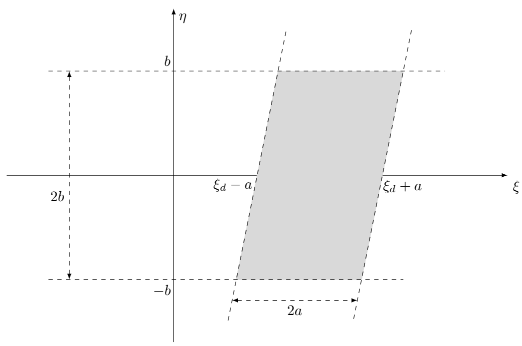

Figure 3.8. 2D signal spectrum domain for a squinted geometry.

We notice that if the small squint angle assumption is not verified, then the factor $\cos\phi$ in the (3.62) becomes relevant and, accordingly, the azimuth signal bandwidth reduces [19].

Because of $\xi \in [\xi_d - a, \xi_d + a]$, we can perform the square root Taylor expansion leading to the equation (3.48), but around $\xi = \xi_d$

$$\sqrt{\left(2a\frac{L}{\lambda}\right)^2\left(1+\varepsilon\frac{\eta}{2b}\right)^2-\left[\xi_d+\left(\xi-\xi_d\right)\right]^2} \approx 2a\frac{L}{\lambda}\left(1+\varepsilon\frac{\eta}{2b}\right)\cos\phi \ + \tag{3.65}$$
$$-\frac{\xi_d\left(\xi-\xi_d\right)}{2a\frac{L}{\lambda}\left(1+\varepsilon\frac{\eta}{2b}\right)\cos\phi}-\frac{\left(\xi-\xi_d\right)^2}{4a\frac{L}{\lambda}\left(1+\varepsilon\frac{\eta}{2b}\right)\cos^3\phi}$$

and substituting this latter in the (3.44), we obtain

$$\Psi(\xi,\eta,r)=\frac{\eta^2}{4b}-4a\left(\frac{L}{\lambda}\right)^2\left(1+\varepsilon\frac{\eta}{2b}\right)\frac{r}{r_0}\sin^2\left(\phi/2\right) \ + \tag{3.66}$$
$$-\frac{\left(\xi-\xi_d\right)^2+2\xi_d\left(\xi-\xi_d\right)\cos^2\phi}{4a'\left(1+\varepsilon\frac{\eta}{2b}\right)\cos^3\phi}$$

which, together with the (3.62), shows the squint effect. Indeed, on one hand the TF spectrum is centered at $\xi_d \neq 0$. On the other, the azimuth chirp rate presents the factor $\cos^3\phi$ and terms in ξ and η linearly dependent on r.

We notice that the approximation used to achieve the (3.2) corresponds to truncate the Taylor expansion of R around $x'-x+r\tan\phi=0$ (see Fig. 3.9)

$$R \approx \frac{r}{\cos\phi}-\sin\phi\left(x'-x+r\tan\phi\right)+\frac{\cos^3\phi}{2r}\left(x'-x+r\tan\phi\right)^2 \tag{3.67}$$

To conclude this section, we observe that the spatial frequency $\xi_d/2\pi$ in Hz units becomes

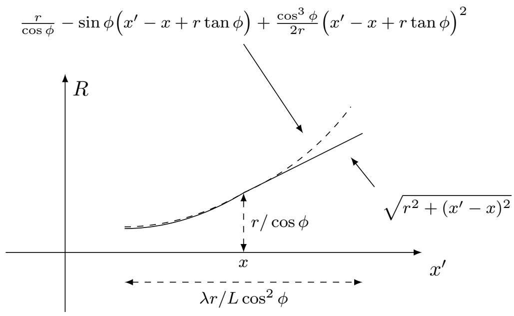

Figure 3.9. Sensor-target distance variation for a squinted geometry.

$$\frac{\xi_d}{2\pi} \to 2\frac{v}{\lambda}\sin\phi \tag{3.68}$$

and represents the Doppler frequency shift (also known as *Doppler centroid*) when the target point is at the center of the antenna beam.

3.3 Point Target Response

In this section we want to analyze the response of a SAR system for a unitary target point at coordinates $(\overline{x}, \overline{r})$, that means to consider $\gamma(x, r) = \delta(x - \overline{x})\delta(r - \overline{r})$. If this is the case, the raw signal backscattered becomes

$$h(x', r') = \gamma(x', r') \otimes g(x', r', \overline{r}) = g(x' - \overline{x}, r' - \overline{r}, \overline{r}) \tag{3.69}$$

If we assume to transmit a chirp pulse, we have

$$
\begin{aligned}
g(x'-\overline{x}, r'-\overline{r}, \overline{r}) \quad \approx \quad & \mathrm{rect}\left[r'-\overline{r}-a\frac{r_0}{\overline{r}}\frac{\varepsilon}{2b}\left(x'-\overline{x}\right)^2\right]\mathrm{rect}\left[\frac{x'-\overline{x}}{\overline{r}/r_0}\right] \\
& e^{jb\left(r'-\overline{r}-a\frac{r_0}{\overline{r}}\frac{\varepsilon}{2b}\left(x'-\overline{x}\right)^2\right)^2} e^{-ja\frac{r_0}{\overline{r}}\left(x'-\overline{x}\right)^2}
\end{aligned} \tag{3.70}
$$

Therefore, following the analysis of the previous sections, the 2D spectrum is

$$
\begin{aligned}
H(\xi,\eta) \quad = \quad & G(\xi,\eta,\overline{r})e^{-j(\eta\overline{r}+\xi\overline{x})} \\
\approx \quad & \frac{\pi}{\sqrt{ab}}\mathrm{rect}\left[\frac{\eta}{2b}\right]\mathrm{rect}\left[\frac{\xi}{2a}\right]e^{-j\left(\frac{\eta^2}{4b}-\frac{\xi^2}{4a\frac{r_0}{\overline{r}}\left(1+\varepsilon\frac{\eta}{2b}\right)}\right)}e^{-j(\eta\overline{r}+\xi\overline{x})}
\end{aligned} \tag{3.71}
$$

The main objective of a SAR processor is the proper combination of all the received contributions from each target on the ground in order to achieve the best resolutions. This consists of a deconvolution operation applied to $h(\cdot)$ to *compensate* for the convolution factor $g(\cdot)$ and *recover* the target contribution. This operation can be efficiently (using the Fast Fourier Transform (FFT) algorithm) performed in the Fourier domain through the multiplication between $H(\cdot)$ and $G^*(\cdot)$ (where $*$ is the conjugate operation). If we do this, we obtain the SAR image of a point target

$$
\hat{\gamma}(x',r') = \mathrm{sinc}\left[a\left(x'-\overline{x}\right)\right]\mathrm{sinc}\left[b\left(r'-\overline{r}\right)\right] \tag{3.72}
$$

As we have seen in sections 2.2.1 and 2.2.2, a point target is imaged as a distributed object with the $3-dB$ resolutions given by

$$\begin{aligned}\Delta r &= \tfrac{\pi}{b} = \tfrac{1}{\Delta f \tau} \\ \Delta x &= \tfrac{\pi}{a} = \tfrac{L}{2X}\end{aligned} \tag{3.73}$$

In not-normalized units

$$\begin{aligned}\Delta r &\rightarrow \Delta r \tfrac{c\tau}{2} = \tfrac{c}{2\Delta f} \\ \Delta x &\rightarrow \Delta x X = \tfrac{L}{2}\end{aligned} \tag{3.74}$$

These latter equations clearly proof that the achievable resolutions depend on the signal bandwidth.

Let us now provide a more accurate interpretation of (3.72). To this aim, we express $G^*(\xi, \eta, \overline{r}) = G_1^*(\eta) G_2^*(\xi, \eta, \overline{r})$, where

$$G_1^*(\eta) = \sqrt{\frac{\pi}{b}} \mathrm{rect}\left[\frac{\eta}{2b}\right] e^{j\frac{\eta^2}{4b}} \tag{3.75}$$

and

$$G_2^*(\xi, \eta, \overline{r}) = \sqrt{\frac{\pi}{a}} \mathrm{rect}\left[\frac{\eta}{2b}\right] \mathrm{rect}\left[\frac{\xi}{2a}\right] e^{-j\frac{\xi^2}{4a\frac{r_0}{\overline{r}}\left(1+\varepsilon\frac{\eta}{2b}\right)}} \tag{3.76}$$

The purpose is to decouple the effect of $G_1^*(\cdot)$ and $G_2^*(\cdot)$ on the image formation.

For first, let us consider the multiplication step involving just the function $G_1^*(\cdot)$. In the r'-domain, this operation corresponds to the convolution of $h(\cdot)$ with $\mathbb{F}^{-1}[G_1^*(\cdot)]$ (where $\mathbb{F}[\cdot]$ is the symbol for the Fourier Transform) and it is referred to as *range compression*:

$$\overline{h}(x', r') \approx e^{-ja\frac{r_0}{\overline{r}}\left(x' - \overline{x}\right)^2} \mathrm{rect}\left[\frac{x' - \overline{x}}{\overline{r}/r_0}\right] \mathrm{sinc}\left[b\left(r' - \overline{r} - a\frac{r_0}{\overline{r}}\frac{\varepsilon}{2b}\left(x' - \overline{x}\right)^2\right)\right] \tag{3.77}$$

which proof that the range-compressed signal (3.77) is spread along the curve given by

$$r' - \overline{r} = a\frac{r_0}{\overline{r}}\frac{\varepsilon}{2b}\left(x' - \overline{x}\right)^2 = \left(\frac{2X}{c\tau}\right)^2\frac{\left(x' - \overline{x}\right)^2}{2\overline{r}} \tag{3.78}$$

Consequently, the factor $G_2^*(\cdot)$ performs two different operations: it rectifies the range-compressed signal on a rectilinear path (*range cell migration* (RCM) compensation)

$$\mathrm{sinc}\left[b\left(r' - \overline{r} - a\frac{r_0}{\overline{r}}\frac{\varepsilon}{2b}(x' - \overline{x})^2\right)\right] \rightarrow \mathrm{sinc}\left[b\left(r' - \overline{r}\right)\right] \tag{3.79}$$

and it combines the azimuth chirp contributions (*azimuth compression*)

$$e^{-ja\frac{r_0}{\overline{r}}\left(x' - \overline{x}\right)^2}\mathrm{rect}\left[\frac{x' - \overline{x}}{\overline{r}/r_0}\right] \rightarrow \mathrm{sinc}\left[a\left(x' - \overline{x}\right)\right] \tag{3.80}$$

Examples of what has been just described are provided from Fig. 3.10 to Fig. 3.12.

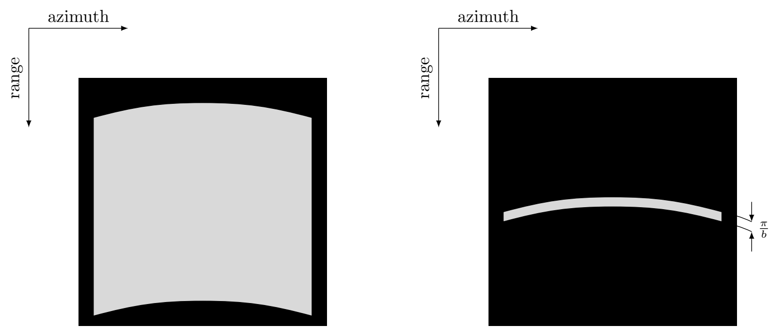

(a) (b)

Figure 3.10. Point target support (in gray) over an absorbing background (in black) (a) and the result of its range compression operation (b).

To conclude this section, we spend few words on the aforementioned analysis but in the presence of a squint angle ϕ. In this case, the obtained

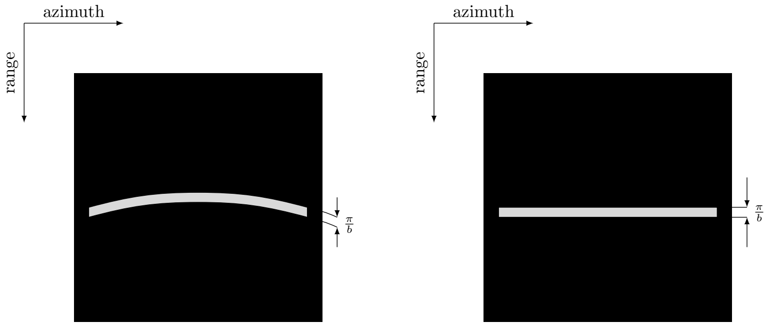

(a) (b)

Figure 3.11. Range compressed point target support (a) and the result of its range cell migration operation (b).

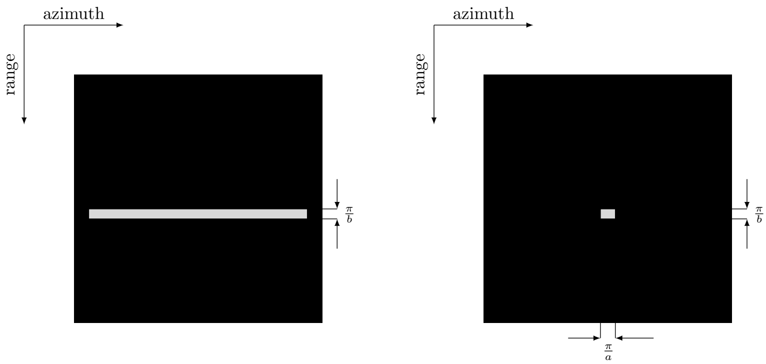

(a) (b)

Figure 3.12. Range compressed and compensated point target support (a) and the result of its azimuth compression operation (b).

results are still valid but the parabolic expression of the sensor-target distance is no more symmetrical. In fact, excursion of x' is now centered around $\overline{x} - c\tau\overline{r}\tan\phi/(2X)$. If this is the case, we have that

$$\begin{aligned}\hat{\gamma}(x', r') \quad &= \quad e^{j\xi_d\left(x'-\overline{x}+\overline{r}\frac{c\tau}{2X}\tan\phi\right)}\operatorname{sinc}\Big[a\Big(x'-\overline{x}+\overline{r}\frac{c\tau}{2X}\tan\phi\Big)\Big] \\ &\quad\quad \operatorname{sinc}\Big[b\Big(r'-\frac{\overline{r}}{\cos\phi}\Big)\Big]\end{aligned} \tag{3.81}$$

3.4 Synthetic Aperture Radar Transfer Function and its Approximations

As known, most of SAR processing algorithms presented in literature depend on different truncations of the series expansion of the TF phase term. In the previous section, we have seen that the function $\Psi(\cdot)$ of the equation (3.44) is linearly dependent on range r. It is desirable for the following analysis to decouple the r-invariant term from the r-variant one:

$$\Psi(\xi, \eta, r) = \Psi_0(\xi, \eta) + (r - r_0)K(\xi, \eta) \tag{3.82}$$

where

$$\Psi_0(\xi, \eta) = \Psi(\xi, \eta, r_0) \tag{3.83}$$

and

$$K(\xi, \eta) = -\frac{2a}{r_0}\Big(\frac{L}{\lambda}\Big)^2\Big(1+\varepsilon\frac{\eta}{2b}\Big) + \frac{L}{\lambda r_0}\sqrt{\Big(2a\frac{L}{\lambda}\Big)^2\Big(1+\varepsilon\frac{\eta}{2b}\Big)^2 - \xi^2} \tag{3.84}$$

If we assume that $|\varepsilon\eta/2b| \ll 1$ (that is almost always valid for the SAR systems), we can perform a series expansion of the square root leading to the following expression (after some arithmetic manipulations):

$$\frac{L}{\lambda r_0}\sqrt{\left(2a\frac{L}{\lambda}\right)^2\left(1+\varepsilon\frac{\eta}{2b}\right)^2-\xi^2}\approx\frac{2a}{r_0}\left(\frac{L}{\lambda}\right)^2\left(1+\varepsilon\frac{\eta}{2b}\right)+\mu(\xi)+\nu(\xi)\eta+\zeta(\xi)\eta^2 \tag{3.85}$$

with

$$\mu(\xi)=-\frac{2a}{r_0}\left(\frac{L}{\lambda}\right)^2+\sqrt{\left(2a\frac{L}{\lambda}\right)^2-\xi^2} \tag{3.86}$$

$$\nu(\xi)=-2a\left(\frac{L}{\lambda}\right)^2\frac{\varepsilon}{2br_0}+\frac{\frac{L}{\lambda}\left(2a\frac{L}{\lambda}\right)^2\frac{\varepsilon}{2br_0}}{\sqrt{\left(2a\frac{L}{\lambda}\right)^2-\xi^2}}=-1+\frac{2a\frac{L}{\lambda}}{\sqrt{\left(2a\frac{L}{\lambda}\right)^2-\xi^2}} \tag{3.87}$$

and

$$\zeta(\xi)=-\frac{\frac{L}{\lambda}\left(2a\frac{L}{\lambda}\right)^2\varepsilon^2\left(\frac{\varepsilon}{2b}\right)^2}{2r_0\sqrt{\left[\left(2a\frac{L}{\lambda}\right)^2-\xi^2\right]^3}} \tag{3.88}$$

Therefore, the $K(\cdot)$ function becomes

$$K(\xi,\eta)\approx\mu(\xi)+\nu(\xi)\eta+\zeta(\xi)\eta^2 \tag{3.89}$$

and the overall TF phase approximated function becomes

$$\begin{aligned}\Psi(\xi,\eta,r) &\approx \tfrac{\eta^2}{4b}+\left[\mu(\xi)+\nu(\xi)\eta+\zeta(\xi)\eta^2\right]r\\ &= \frac{\frac{\eta^2}{4b}}{1+4b\zeta(\xi)r}+\left[\mu(\xi)+\nu(\xi)\eta\right]r\end{aligned} \tag{3.90}$$

The phase factor $\mu(\xi)r$ causes the azimuth compression and it leads to an azimuth chirp function whose rate varying with range. The $\nu(\xi)\eta r$ term takes into account for the major component of the range migration phenomenon and it is referred to as RCM in the frequency domain. The $\zeta(\xi)\eta^2 r$ term results in a chirp signal, but it differs from the transmitted one because its rate is both range and azimuth-frequency dependent. This factor can be compensated by a further range compression step and, because of this, it is typically referred to as *secondary range compression* (SRC) [21]. Both these latter $\xi - \eta$ coupling terms account for the correction step of equation (3.79) of the section 3.3.

3.5 Synthetic Aperture Radar Focusing

In this section, we want to describe the SAR process in the case of an extended scene on the ground. As usual, we start from the raw signal neglecting the dependence on the range (that means to set $r = r_0$). This approach is convenient to analyze the processing (*focusing*) procedure. Hence, we have

$$h(x', r') = \iint \gamma(x, r) g(x' - x, r' - r, r_0) dx dr \tag{3.91}$$

As explained in the previous sections, we want to obtain an estimation of the reflectivity pattern ($\hat{\gamma}(\cdot)$) from the (3.91). In order to do this, it is convenient to perform the deconvolution operation in the Fourier domain thanks to the using of the FFT algorithm. Therefore, if $G_0(\xi, \eta) = \mathbb{F}[g(x', r', r_0)] = G(\xi, \eta, r_0)$, we get

$$H(\xi, \eta) = \Gamma(\xi, \eta) G_0(\xi, \eta) \tag{3.92}$$

which can be inverted for $\Gamma(\xi, \eta)$ *within the systems bandwidth*, providing

$$\Gamma(\xi, \eta) = H(\xi, \eta) G_0^*(\xi, \eta) \tag{3.93}$$

Accordingly, in the time domain

$$\begin{aligned}\hat{\gamma}(x', r') &= \frac{1}{(2\pi)^2}\iint \Gamma(\xi,\eta)e^{j\xi x'}e^{j\eta r'}d\xi d\eta \\ &= \gamma(x', r') \otimes \mathrm{sinc}(ax')\mathrm{sinc}(br')\end{aligned} \tag{3.94}$$

which, in the case of the presence of a squint angle, becomes

$$\hat{\gamma}(x', r') = \gamma(x', r') \otimes \mathrm{sinc}(ax')\mathrm{sinc}(br')e^{j\xi_d x'} \tag{3.95}$$

This 2D-processing is referred to as *narrow focus code*, because of only the central part of the illuminated area is perfectly focused, being $r = r_0$. The relative flowchart is reported in Fig. 3.13.

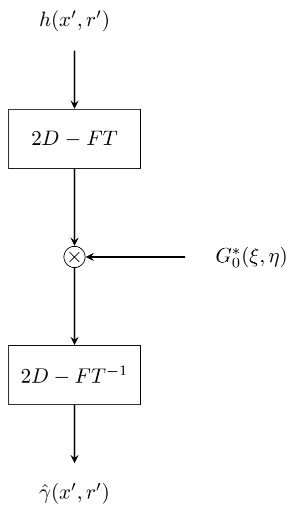

Figure 3.13. Narrow focus SAR processing flowchart.

The fully focused image process (*wide focus code*) is now in order. Let us consider

$$G(\xi, \eta, r) = G_0(\xi, \eta)e^{-j(r-r_0)K(\xi,\eta)} \tag{3.96}$$

where the $K(\cdot)$ function has been defined in (3.84). If we put $r' - r_0 \to r'$ and $r - r_0 \to r$, the $H(\cdot)$ function becomes

$$\begin{aligned} H(\xi,\eta) &= G_0(\xi,\eta) \iint \gamma(x,r) e^{-j\xi x} e^{-j(\eta+K(\xi,\eta))r} dx dr \\ &= G_0(\xi,\eta)\Gamma[\xi,\eta+K(\xi,\eta)] \end{aligned} \tag{3.97}$$

As we can notice, the FT of $\gamma(\cdot)$ is now computed over the grid $[\xi, \eta + K(\xi,\eta)]$. This means that the r-dependence of the TF generates a nonlinear mapping (*grid deformation*) [22–24] of the range frequencies of $\Gamma(\cdot)$ (see Fig. 3.14).

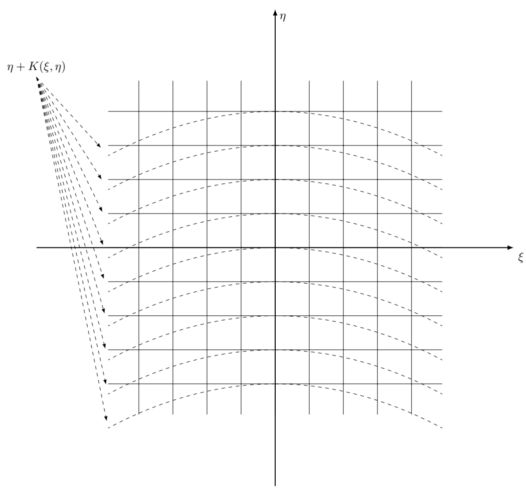

Figure 3.14. Grid distortion due to the r-dependent SAR TF phase term.

In order to pass from the nonlinear grid to the linear one, we have to perform a ξ-dependent shift of $\Gamma(\cdot)$ in the η-direction, according to the function $K(\cdot)$ (*counter deformation*), that leading to the block diagram of Fig. 3.15

Let us replace the series expansion of the equation (3.89) truncated to

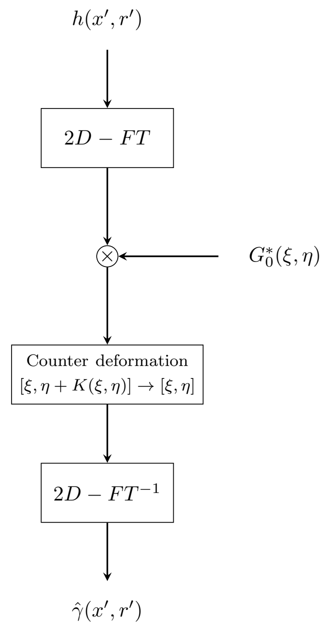

Figure 3.15. Wide focus SAR processing flowchart.

the linear term

$$K(\xi, \eta) \approx \mu(\xi) + \eta\nu(\xi) \tag{3.98}$$

in the (3.97) obtaining

$$\begin{aligned} H(\xi, \eta) &\approx G_0(\xi, \eta)\Gamma[\xi, \eta(1 + \nu(\xi)) + \mu(\xi)] \\ &= G_0(\xi, \eta)\Gamma[\xi, \eta\Omega(\xi) + \mu(\xi)] \end{aligned} \tag{3.99}$$

where

$$\Omega(\xi) = 1 + \nu(\xi) \tag{3.100}$$

is the range scaling factor. The equation (3.99) suggests us to perform the following process whose flowchart is shown in Fig. 3.16.

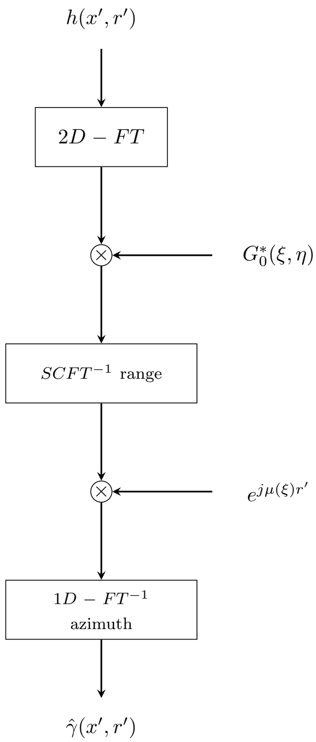

Figure 3.16. Wide focus SAR processing flowchart based on $SCFT^{-1}$ algorithm.

For first, we compute the 2D-FT of the raw signal and perform the r-invariant SAR filtering multiplying it by $G_0^*(\cdot)$. So, we have

$$\Gamma[\xi, \eta\Omega(\xi) + \mu(\xi)] \approx H(\xi, \eta)G_0^*(\xi, \eta) \tag{3.101}$$

Then, we perform an inverse *range-scaled* FT ($SCFT^{-1}$) that includes the scaling factor $\Omega(\cdot)$ in its kernel:

$$
\begin{aligned}
SCFT^{-1}\{\Gamma[\xi,\eta\Omega(\xi)+\mu(\xi)]\} &= \tfrac{1}{2\pi}\int \Gamma[\xi,\eta\Omega(\xi)+\mu(\xi)]e^{j\Omega(\xi)\eta r'}d[\Omega(\xi)\eta] \\
&= \hat{\gamma}(\xi,r')e^{-j\mu(\xi)r'}
\end{aligned}
\tag{3.102}
$$

The third step account for the focus depth variation effect. And finally, the standard azimuth inverse FT provides us the same result of the equation (3.94) and (3.95), for the squinted case. The presented method ensures an efficient digital implementation except for the $SCFT^{-1}$ part. To satisfy this requirement some techniques are available. Their details are not a specific object of this work and, for this reason, the interested reader can refer to available literature [25–28].

Eventually, if SAR system geometries are such that $\Omega(\xi) \approx 1$, we have

$$
H(\xi,\eta) = G_0(\xi,\eta)\Gamma(\xi,\eta+\mu(\xi)) \tag{3.103}
$$

and this allow us to replace the $SCFT^{-1}$ block in Fig. 3.16 with a conventional inverse FT, resulting in the procedure of Fig. 3.17. This technique is well known in literature as *monochromatic* 2D algorithm [29] and an efficient implementation is reported in [30].

3.6 Motion Compensation

In the following section, we want to show how the information about the changing of the platform forward velocity vector can be taken into account in the SAR data processing. In other words, we describe the way to compensate the motion errors due to the deviations of the shuttle from the nominal trajectory.

Let us consider the scheme of Fig. 3.18, where $S(x_s, y_s, z_s)$ is the radar position and $P(x, y, z)$ is the generic target point on the ground. The distance between them is

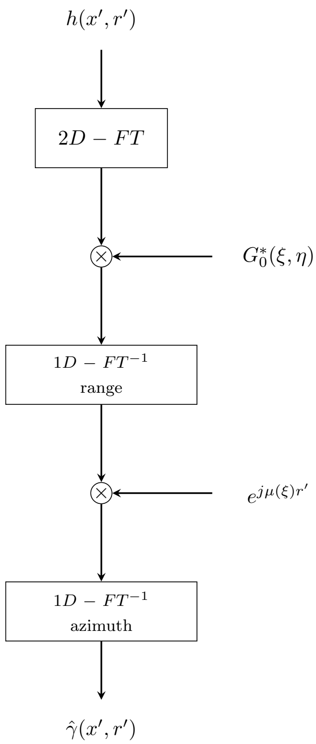

Figure 3.17. Wide focus SAR processing flowchart based on monochromatic algorithm.

$$R_{ST} = \sqrt{(x_s - x)^2 + (y_s - y)^2 + (z_s - z)^2} \tag{3.104}$$

If we neglect the changing in the along-track nominal trajectory (usually compensated through a real-time adjustment of the pulse repetition frequency), we can approximate R as follow:

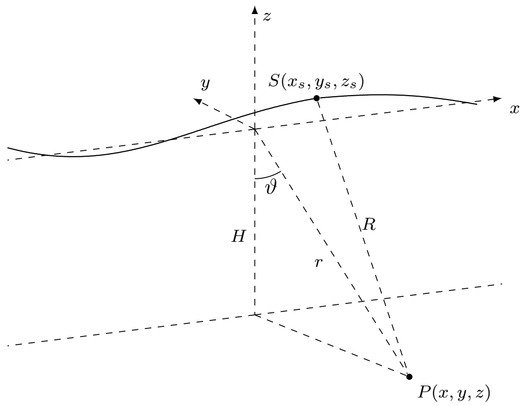

Figure 3.18. SAR geometry in the presence of motion errors.

$$
\begin{aligned}
R_{ST} &\approx \sqrt{(x'-x)^2 + y^2 + z^2 - 2yy_s - 2zz_s} \\
&\approx \sqrt{(x'-x)^2 + r^2 + 2(y_s r \sin\vartheta + z_s r \cos\vartheta)} \\
&\approx \sqrt{(x'-x)^2 + r^2} + y_s \sin\vartheta + z_s \cos\vartheta) \\
&\approx R + r_{LOS}
\end{aligned}
\tag{3.105}
$$

where R is the nominal sensor-target distance (see equation 3.4) and r_{LOS} is the *displacement in line of sight (LOS)* and it accounts for the y and z platform displacement components (Fig. 3.19).
As we can see, r_{LOS} depends on both the platform deviations and the look angle ϑ. This latter is unpredictable being dependent on the scene topography. If we assume a flat surface on the ground ($\vartheta = \cos^{-1}(H/r)$), it is possible to rewrite r_{LOS} as

$$
r_{LOS} = r_{LOS}(y_s, z_s, r) \tag{3.106}
$$

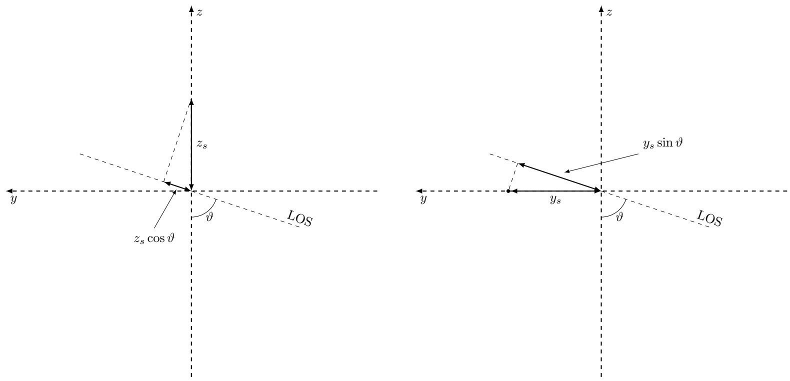

(a) (b)

Figure 3.19. LOS projection of the platform displacement along the z axis (a) and y axis (b).

If the range migration effect is negligible ($r \approx r'$), we have

$$r_{LOS} = r_{LOS}(y_s, z_s, r') \tag{3.107}$$

and we can compensate the motion error after the range compression operation.

On the opposite case, we have to decouple the phase correction in two terms, referred as *first order* and *second order motion compensation factors*, respectively [15]:

$$\begin{aligned} r_{LOS_I} &= r_{LOS}(y_s, z_s, r_0) \\ r_{LOS_{II}} &= r_{LOS}(y_s, z_s, r') - r_{LOS}(y_s, z_s, r_0) \end{aligned} \tag{3.108}$$

Hence, this leads us to the flowchart of Fig. 3.20.

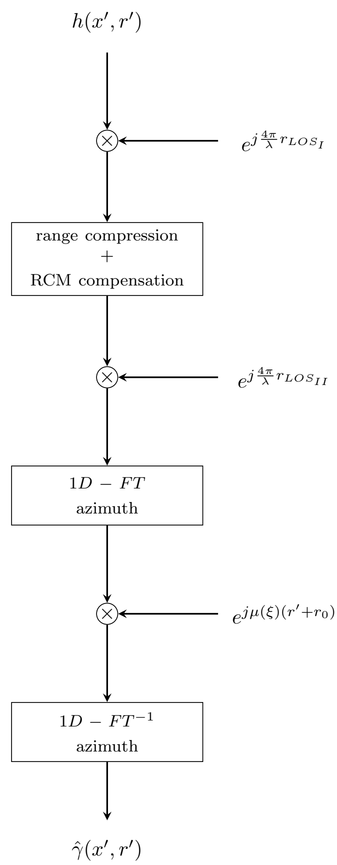

Figure 3.20. SAR processing flowchart in presence of motion errors.

Chapter 4

Unified Formulation for SAR Raw Signals

4.1 Different Acquisition Modes Analysis

In this chapter, we introduce the first main contribution achieved within the Ph.D. degree, that is the generation of a unique formula able to express the SAR raw signals provided from each acquisition modes. Then, we test this formula on the TOPSAR raw signal simulation providing the computational assessment and examples relative to extended scenes. To this aim, it is firstly necessary to complete the discussion, begun in the previous chapters, about the most important SAR operation modes.

4.1.1 Scan Synthetic Aperture Radar Mode

Let us start to consider the usual cylindrical coordinates system (x, r, ϑ) in Fig. 3.1 of chapter 3. The key point of the scan mode is that the radar is continuously *active* but the antenna main beam is *periodically switched* to illuminate neighboring subswaths (see Fig. 4.1 where a two-subswaths example is shown).

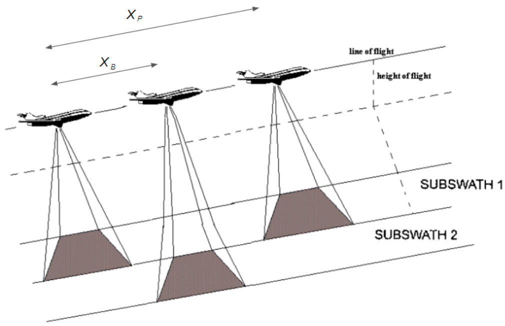

Figure 4.1. Scan mode acquisition geometry for the two subswaths case.

The time interval T_B within which a subswath is illuminated is called *burst* and it corresponds to the flown trajectory portion $X_B = vT_B$, where v is the constant velocity of the shuttle. The space interval between two bursts illuminating the same subswaths is referred to as *burst period* X_P. If we call X_S (larger than X_B) the synthetic antenna length coincident with the 3-dB azimuth antenna footprint (see Fig. 4.2), we notice that there are no holes in the investigated scene if

$$X_S \geq X_P - X_B \tag{4.1}$$

Obviously, because of targets inside the single burst illuminated area are not all on the same footing, only the marked area is illuminated for all the burst duration. This implies that processing data of a single burst produces an image with lower resolution at the edges. For this reason, if we want a uniform resolution, X_P has to be shortened, leading to the new condition (see Fig. 4.3)

$$X_S \geq X_P + X_B \tag{4.2}$$

It is evident that in the scan mode the PRF is still constrained by equation

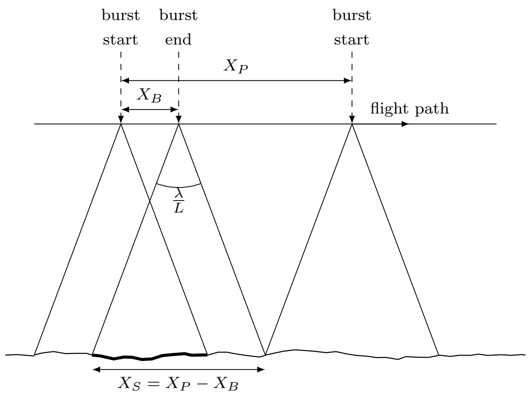

Figure 4.2. Bursting operation for continuous image coverage in the case limit $X_S = X_P - X_B$. The drawing refers to the same subswath

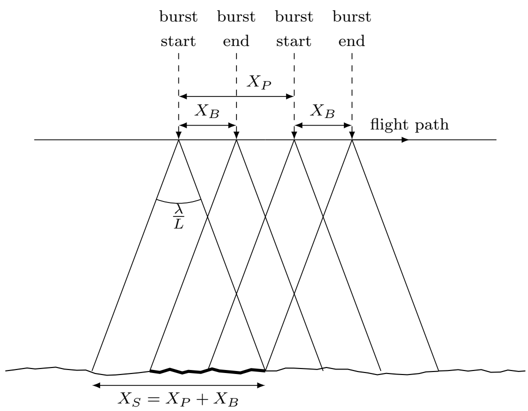

Figure 4.3. Bursting operation for full resolution continuous image coverage in the case limit $X_S = X_P + X_B$. The drawing refers to the same subswath

(2.33) of the section 2.4 but within a subswath. Therefore, the periodic illumination of different subswaths allows the increase of the range swath, but at the expense of an azimuth resolution degradation (compared to the strip mode case) due to the fact that only portions of the fully synthetic antenna length are collected for each target.

Carrying out the same analysis of chapter 3, in the case of normalized variables [1], we get for the burst unit response

$$\begin{aligned} g(x'-x, r'-r, x', r) &= e^{-j2\pi\frac{c\tau}{\lambda}r} e^{-ja\frac{2L}{\lambda}\Delta R} w^2\left[\frac{x'-x}{r/r_0}\right]\mathrm{rect}\left[\frac{x'}{X_B}\right] \\ & \qquad e^{jb\left(r'-r-\frac{2X}{c\tau}\Delta R\right)^2}\mathrm{rect}\left[r'-r-\frac{2X}{c\tau}\Delta R\right] \end{aligned} \tag{4.3}$$

where a, b and ΔR are the same of the chapter 3.

If we compare the (4.3) to the strip mode impulse response, we can write

$$g_{scan}(x'-x, r'-r, x', r) = g_{strip}(x'-x, r'-r, r)\mathrm{rect}\left[\frac{x'}{X_B}\right] \tag{4.4}$$

and we can conclude that the burst factor, $\mathrm{rect}[x'/X_B]$, returns the burst signal explicitly *azimuth dependent.*

Moving to the frequency domain, we have

$$\begin{aligned} G_{scan}(\xi, \eta, x, r) &\sim G_{strip}(\xi, \eta, r)\mathrm{rect}\left[\frac{x-\xi r/(2ar_0)}{X_B}\right] \\ &= G_{strip}(\xi, \eta, r)\mathrm{rect}\left[\frac{\xi-2axr_0/r}{2aX_Br_0/r}\right] \end{aligned} \tag{4.5}$$

which shows that the azimuth (spatial) spectrum is shifted around the frequency $2axr_0/r$, dependent on the target location. Then, the bandwidth is reduced compared to the strip mode case, being $X_Br_0/r = X_B/X_S < 1$. The azimuth bandwidth is directly related to the azimuth resolution and we aspect a resolution degradation proportional to the ratio X_S/X_B.

At this point, it is convenient to introduce the factor

[1] we mean that also X_B, X_S and X_P are normalized to $X \approx \lambda r_0/L$ which is the 3 dB midswath antenna footprint

$$N_L = \frac{X_S - X_B}{X_P} \tag{4.6}$$

which represents an equivalent number of looks. If $X_S = X_P + X_B$, then $N_L = 1$ and targets within the resolved area are illuminated by single burst. Consequently, if $X_S = NX_P + X_B$ (with N integer), we have that $N_L = N$ and each target inside the fully resolved area is illuminated N times. Therefore, $N_L = 1$ in the (4.5) and, in fact, it refers to the burst TF and not to the overall scan mode TF. This last one can be obtained from the (4.5) by superposition:

$$G_{scan}(\xi, \eta, x, r) \sim G_{strip}(\xi, \eta, r) \sum_{k=0}^{N_L-1} \mathrm{rect}\Big[\frac{\xi - 2a(x + kX_P)r_0/r}{2aX_B r_0/r}\Big] \tag{4.7}$$

Proceeding in a way similar to that one of section 3.3, we can consider a point target located in $(\bar{x}, \bar{r})$ and the (burst) image target response can be written as

$$\begin{aligned} \hat{\gamma}(x' - \bar{x}, r' - \bar{r}, \bar{x}, \bar{r}) \quad &= \quad \mathrm{sinc}\big[b(r' - \bar{r})\big] w^2 \Big[\tfrac{\bar{x}}{\bar{r}/r_0}\Big] \\ & \quad\quad \mathrm{sinc}\big[a' X_B (x' - \bar{x})\big] e^{ja'(x'^2 - \bar{x}^2)} \end{aligned} \tag{4.8}$$

which can be protracted to the case of an extended scene of reflectivity $\gamma(x, r)$, letting $\bar{x} \to x$, $\bar{r} \to r$ and by superposition, obtaining

$$\begin{aligned} \hat{\gamma}(x', r') \quad &\approx \quad w^2 \Big[\tfrac{x'}{r'/r_0}\Big] \iint \gamma(x, r) e^{ja'(x'^2 - x^2)} \\ & \quad\quad \mathrm{sinc}\big[b(r' - r)\big] \mathrm{sinc}\big[a' X_B (x' - x)\big] dx dr \end{aligned} \tag{4.9}$$

Comparison between the strip mode and the scan mode is now in order. The main effects of the burst windowing are on amplitude, phase and resolution of the azimuth component of the point target response.

In particular, the amplitude modulation is due to the two-way antenna pattern (*scalloping effect* [8, 9]) and its compensation requires knowledge of the antenna radiation diagram end pointing directions (in elevation and azimuth).

The phase term $a'(x'^2 - \bar{x}^2)$ (absent in the strip mode case) is dependent on the target location and it is zero for $x' = \bar{x}$ (that is at the peak of the impulse response). Phase variation from pixel to pixel can be quite large, so interpolation operations must be carefully carried out.

Eventually, just few words about the azimuth resolution decreasing. Comparing the (4.8) to the counterpart of the strip mode case we can write that

$$\Delta x_{scan} = \frac{\pi}{a' X_B} = \frac{\pi}{a} \frac{\bar{r}/r_0}{X_B} = \frac{\pi}{a} \frac{X_S}{X_B} = \Delta x_{strip} \frac{X_S}{X_B} \tag{4.10}$$

This degradation depends on the fact that only the fraction X_B/X_S of the overall synthetic antenna is available. In addition, X_S changes with range and the azimuth resolution is range dependent, too.

4.1.2 Spotlight Synthetic Aperture Radar Mode

Let us start to consider the usual cylindrical coordinates system (x, r, ϑ) in Fig. 3.1 of chapter 3, with a sensor moving at the constant velocity v. The key point of the spotlight mode is that the antenna beam is continuously *steered* during the overall acquisition time T_l (corresponding to the trajectory portion $X_l = vT_l$), pointing always at the same area on the ground (as depicted in Fig. 4.4).

In this case, the number of the received backscattered pulses from each target within the illuminated area is increased with respect to the strip mode, leading to an improvement in the azimuth resolution. However, this gain is traded off by loss of coverage due to the illumination of limited area along the flight path. From this viewpoint, we can consider the spot

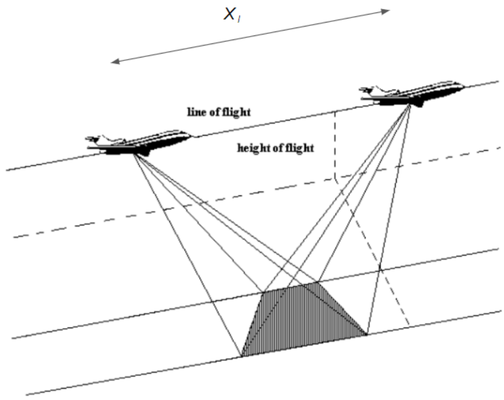

Figure 4.4. Spot mode acquisition geometry.

mode as dual to the scan mode, while the strip operation is in the middle of the previous two ones.

Exploiting the usual analysis in the time domain, but letting

$$\gamma(x,r) \to \gamma(x,r) w^2(x,r) e^{-j2\pi \frac{c\tau}{\lambda} r} \tag{4.11}$$

we reach the following expression for the system impulse response:

$$\begin{aligned} g(x'-x, r'-r, x', r) &= e^{-ja\frac{2L}{\lambda}\Delta R} e^{jb\left(r'-r-\frac{2X}{c\tau}\Delta R\right)^2} \\ &\quad \mathrm{rect}\left[r'-r-\frac{2X}{c\tau}\Delta R\right] \mathrm{rect}\left[\frac{x'}{X_l}\right] \end{aligned} \tag{4.12}$$

For first, we notice that no assumption has been made on the antenna pattern $w(\cdot)$, although it plays a key role in the spot technique. In addition, as for the scan mode case, the (4.12) shows a dependence on x' and r variables. In particular, the former is caused by the $\mathrm{rect}[x'/X_l]$ factor which recalls the burst factor $\mathrm{rect}[x'/X_B]$ of the scan mode case. But, it is important to underline that these two factors are on totally different footing: indeed, in general, X_l is larger thant the azimuth spot extension, at variance with X_B that is usually much smaller than the azimuth antenna footprint.

In order to perform an easy comparison between the spotlight mode and the stripmap one we can rewrite the 4.12 as

$$g_{spot}(x' - x, r' - r, x', r) \sim g_{strip}(x' - x, r' - r, r)\mathrm{rect}\left[\frac{x'}{X_l}\right] \tag{4.13}$$

Moving to the frequency domain, we get the spotlight mode TF

$$\begin{aligned} G_{spot}(\xi, \eta, x, r) &\sim G_{strip}(\xi, \eta, r)\mathrm{rect}\left[\tfrac{x-\xi r/(2ar_0)}{X_l}\right] \\ &= G_{strip}(\xi, \eta, r)\mathrm{rect}\left[\tfrac{\xi-2axr_0/r}{2aX_l r_0/r}\right] \end{aligned} \tag{4.14}$$

which allows us to clarify the aforementioned azimuth resolution improvement. In fact, we can write

$$\Delta x_{spot} = \frac{\pi}{aX_l}\frac{r}{r_0} = \frac{\pi}{a}\frac{X_S}{X_l} = \Delta x_{strip}\frac{X_S}{X_l} \tag{4.15}$$

As we can notice by the (4.14), if $X_l/X_S > 1$ the azimuth signal bandwidth is larger than the strip mode case. This implies that the azimuth resolution improves (see equation (4.15)), but also requires large sampling rates to avoid undersampling effects. In other words, the PRF must be high enough to properly sample the signal in the azimuth direction according to its bandwidth characteristics. The reader interested to this last aspect can well refer to [8].

4.2 Unified Raw Signal Formulation for All the Acquisition Modes

As we have understood from the previous sections, SAR systems can acquire data by using several operative modes. the proper mode to be used is chosen based on the specific purpose. Indeed, starting from the strip acquisition technique, spotlight mode is preferable if we desire to reach a better resolution; on the opposite, scan method has to be selected if we want to achieve a larger coverage on the ground.

For the sake of completeness, there are other two SAR acquisition modes which can be considered as an alternative solution of that one described in sections 4.1.1 and 4.1.2.

The first one is the so-called *hybrid stripmap/spotlight* or *sliding spotlight* mode [31–33]. Let us consider the geometry in Fig. 4.5, where the SAR sensor moves with constant velocity v along the x-axis and illuminates the surface with a steerable antenna beam. X_1 is the length of the flight path portion used to acquire the raw data, r_0 the range distance from the line of flight to the center of the observed scene on the ground,

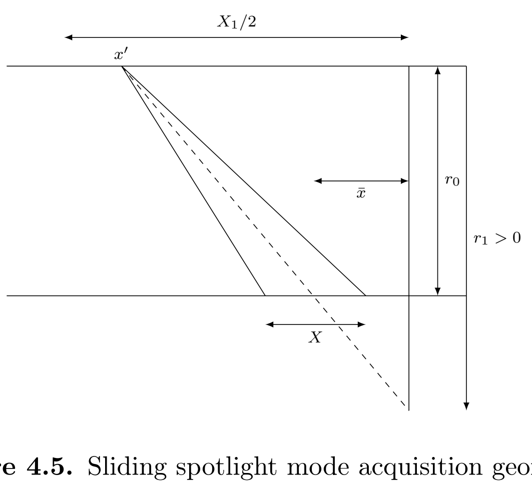

Figure 4.5. Sliding spotlight mode acquisition geometry.

and we define r_1 the *oriented distance* from the line of flight to the beam rotation center. In this case, $r_1 > 0$ and the radar antenna beam is steered about a point farther away from the radar than the area being observed in such a way the antenna footprint on the ground moves more slowly than the sensor (it *slides*). It is evident that this strategy allow us to obtain a compromise between the ground coverage and the resolution: in fact, the former is larger than the spotlight case but smaller than the strip one; the latter is better than the strip mode case but worse than the spotlight one.

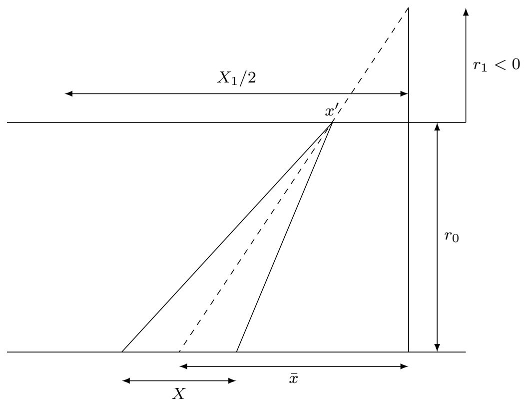

Figure 4.6. TOPSAR mode acquisition geometry.

The second alternative technique is known as *Terrain Observation by Progressive Scans* (TOPSAR) [34]. The main purpose of this acquisition method is to improve range coverage at the expense of azimuth resolution, but avoiding the scalloping effect (usually annoying the scan mode). To this aim the antenna beam is still periodically switched among different range subswaths, but within each burst, it is also steered from backward to forward (i.e., in the opposite way with respect to the spot or sliding spotlight cases) in such a way that the antenna footprint on the ground moves faster than the sensor. As we can see by the Fig. 4.6, in this case $r_1 < 0$ so that the main beam rotation center is above the sensor.

All the aforementioned operational modes are nowadays of practical interest. Indeed, while the first spaceborne SAR systems (as ERSS and ENVISAT) used stripmap and scanSAR modes, the most recent ones (for example, Cosmo-SkyMed, TerraSAR-X and Sentinel-1) are also employing sliding spotlight and/or TOPSAR modes [35]. For these reasons, many different algorithms have been developed to properly process data acquired by these different techniques [8, 9, 31–34, 36, 37]. Each technique have a proper formulation. Therefore, it becomes necessary to generate a unified raw signal formulation for all the acquisition modes. Actually, a work like this has been proposed in [38], but just for a point target and only in the space domain. Here, we describe a clear, general and analytical formulation able to express raw signals acquired by all the acquisition methods for extended scenes and both in space and frequency domains.

Before starting this analysis, it is worthwhile to underline that in the following we refer just to the case of not-normalized variables.

Let us start to consider the acquisitions geometry of Figs. 4.5 and 4.6 and the usual cylindrical coordinate systems of Fig. 3.1 of section 3.1. Moreover, for the sake of simplicity, we assume that $X_1 \ll |r_1|$ without losing any generality. Let us introduce the factor

$$A = \frac{r_1 - r_0}{r_1} \tag{4.16}$$

in such a way that it can be used to express both the sliding spotlight factor (defined in [32]) and the TOPSAR factor (defined in [34]). By simple geometric considerations, we verify that the angular velocity of the antenna beam is

$$\omega_a = \frac{v}{r_1} = \frac{v}{r_0}(1 - A) \tag{4.17}$$

that the antenna azimuth footprint over the ground moves with velocity

$$v_f = Av \tag{4.18}$$

and that, when the shuttle is in x', the center of the antenna azimuth footprint is at the position

$$\bar{x} = Ax' \tag{4.19}$$

As a consequence, the azimuth antenna pattern assumes the following expression

$$w\Big(\frac{Ax' - x}{X}\Big) \tag{4.20}$$

and the SAR system impulse response can be written as

$$\begin{aligned} g(x', r' - r, x, r) \quad = \quad & e^{-j\frac{4\pi}{\lambda}\Delta R} e^{-j\frac{4\pi}{\lambda}\frac{\Delta f/f}{c\tau}(r'-r-\Delta R)^2} \\ & \mathrm{rect}\Big[\tfrac{r'-r-\Delta R}{c\tau/2}\Big] w^2\Big(\tfrac{Ax'-x}{X}\Big)\mathrm{rect}\Big[\tfrac{x'}{X_1}\Big] \end{aligned} \tag{4.21}$$

By analyzing the last two factor of the equation (4.21), we notice that the generic ground point at position x is observed from a synthetic antenna length composed by all the trajectory points x' belonging at the same time to both the interval $[x/A - X/(2|A|), x/A + X/(2|A|)]$ and the interval $[-X_1/2, X_1/2]$. Moreover, the fully focused ground area is formed by the ground points x, such that the first interval (of size $X/|A|$), is included in the second one (of size X_1), if $X/|A| < X_1$, or the second interval is included in the first one if $X/|A| > X_1$. Therefore, we recognise that the synthetic antenna length of the fully focused ground points is

$$X_{SA} = \min\left\{\frac{X}{|A|}, X_1\right\} \tag{4.22}$$

and that the azimuth antenna size of the fully focused ground area is

$$X_F = ||A|X_1 - X| \tag{4.23}$$

Moving to the frequency domain, we get the SAR system TF

$$\begin{aligned} G(\xi, \eta, x, r) &= e^{j\frac{\eta^2}{4b}} e^{j\frac{\xi^2(r/r_0)}{4a(1+\eta\lambda/4\pi)}} \mathrm{rect}\left[\frac{\eta}{bc\tau}\right] \\ & \mathrm{rect}\left[\frac{B(\xi - 2ax)}{2aX}\right] w^2\left(\frac{A\xi - 2a(A-1)x}{2aX}\right) \end{aligned} \tag{4.24}$$

where we have introduced the new factor

$$B = \frac{X}{X_1} \tag{4.25}$$

Moreover, observing the last three terms of (4.24), we realize that the range bandwidth is

$$\frac{\Delta\eta}{2\pi} = \frac{bc\tau}{2\pi} = \frac{2\Delta f}{c} \tag{4.26}$$

as discussed in the previous sections; while, the azimuth bandwidth of each fully focused ground point is

$$\frac{\Delta\xi}{2\pi} = \frac{a}{\pi} X_{SA} = \frac{a}{\pi}\min\left\{\frac{X}{|A|}, X_1\right\} = \frac{2/L}{\max\{|A|, B\}} \tag{4.27}$$

Therefore, the overall azimuth bandwidth of the fully focused ground area can be obtained from the last two factors of the (4.24) and using the (4.23)

$$\xi_{max} - \xi_{min} = \frac{2}{L}\left(1 + \frac{X_1}{X}|1 - A|\right) = \frac{2}{L}\left(1 + \frac{|1 - A|}{B}\right) \tag{4.28}$$

Eventually, it is now possible to retrieve the SAR system slant range and azimuth resolutions

$$\begin{aligned} \Delta r &= \tfrac{c}{2\Delta f} \\ \Delta x &= \tfrac{L}{2}\max\big\{|A|, B\big\} \end{aligned} \tag{4.29}$$

At this point, it is worthwhile to notice that both the equations from (4.17) to (4.23), in the space domain, and the equations from (4.24) to (4.29), in the frequency domain, hold for any real value of A and for any positive real value of B. In addition, by varying them, all the acquisition modes [2] can be addressed (see Tab. 4.1).

Range of values	**Acquisition modes**
$A = 0$	spotlight
$0 < A < 1$	sliding spotlight
$A = 1, B \ll 1$	stripmap
$A = 1, B > 1$	scanSAR
$A > 1$	TOPSAR
$-1 \leq A < 0$	inverse sliding spotlight
$A < -1$	inverse TOPSAR

Table 4.1. Summary table of all the SAR acquisition modes at varying of A and B values.

To conclude this section, we want to remark that the presented discussion can be extended to the case of the presence of a squint angle ϕ. In fact, if this is the case, the equation (4.19) is replaced by $\bar{x} = Ax' + \phi r_0$ in such a way that in the numerator of the argument of the $w(\cdot)$ function, a term ϕr_0 must to be added in the (4.20) and (4.21), and a term $2a\phi r_0$ must be added in the (4.24).

[2]other two modes have been now introduced in Tab. 4.1: the *inverse* modes. In general, they are less convenient than the direct ones, because the coverage and resolution properties are the same, but the antenna rotation velocity is higher. For these reasons, they have been neglected in this thesis. Anyway, the interested reader can refer to it in [39]

4.2.1 Simulation of SAR Raw Signals: Sliding Spotlight and TOPSAR Modes

As well explained in chapter 3, for the stripmap case, and in section 4.1, for the scanSAR and the spotlight modes, it is possible to manage both the azimuth and range dependence of the SAR TF through a full 2D-FT approach. This allows us to implement efficient simulation of raw signals relative to extended scenes [40, 41].

On the opposite, for the sliding spotlight and TOPSAR cases, while the r-dependence of the SAR TF can still be managed (as we can see in the following), no procedure can be implemented to handle its x-dependence and an efficient simulation algorithm cannot be designed in the 2D-FT domain. Moreover, although an algorithm in the only space domain is possible, it is not computationally efficient and, therefore, not practicable in case of extended scenes. In [42], for the sliding spotlight case, the authors proposed an approach involving a range 1D-FT with a limited-range-swath assumption. This hypothesis is often reasonable for that case, but may be inappropriate for some TOPSAR systems.

The presented method is still based on a range 1D-FT but it can relax the limited-range-swath assumption and, hence, can be employed for any acquisition mode.

Let us start from the classical way to define the SAR raw signals in the space domain

$$h(x', r') = \iint \gamma(x, r) g(x', r' - r, x, r) dx dr \tag{4.30}$$

Using the $g(\cdot)$ function of the (4.21), we can rewrite it as follows

$$h(x', r') = \operatorname{rect}\left[\frac{x'}{X_1}\right] \int \left\{ \int \gamma_1(x', x, r) g_1(x' - x, r' - r, r) dr \right\} dx \tag{4.31}$$

where we have defined

$$\gamma_1(x', x, r) = \gamma(x, r) e^{-j\frac{4\pi}{\lambda}\Delta R} w^2\left(\frac{Ax' - x}{X}\right) \tag{4.32}$$

and

$$g_1(x' - x, r' - r, r) = e^{-j\frac{4\pi}{\lambda}\frac{\Delta f/f}{c\tau}(r'-r-\Delta R)^2} \mathrm{rect}\left[\frac{r' - r - \Delta R}{c\tau/2}\right] \tag{4.33}$$

The range 1D-FT of $h(\cdot)$ is given by

$$\begin{aligned} H(x', \eta) &= \int h(x', r') e^{-j\eta r'} dr' \\ &= \mathrm{rect}\left[\frac{x'}{X_1}\right] \int \Bigg\{ \int \gamma_1(x', x, r) e^{-j\eta r} dr \\ &\quad \int g_1(x' - x, r' - r, r) e^{-j\eta(r'-r)} dr' \Bigg\} dx \end{aligned} \tag{4.34}$$

The last integral in (4.34) can be evaluated using the stationary phase method, obtaining

$$\begin{aligned} G_1(x' - x, \eta, r) &= e^{j\frac{\eta^2}{4b}} \mathrm{rect}\left[\frac{\eta}{bc\tau}\right] e^{-j\eta\Delta R} \\ &= G_{10}(x' - x, \eta) e^{-j\eta(\Delta R - \Delta R_0)} \end{aligned} \tag{4.35}$$

where

$$G_{10}(x' - x, \eta) = e^{j\frac{\eta^2}{4b}} \mathrm{rect}\left[\frac{\eta}{bc\tau}\right] e^{-j\eta\Delta R_0} \tag{4.36}$$

and

$$\Delta R_0 = \Delta R(x' - x, r' = r_0) = \sqrt{r_0^2 + (x' - x)^2} - r_0 \tag{4.37}$$

Now, if $\eta(\Delta R - \Delta R_0) \ll 1$, which take into account for a maximum limit to the range swath size (see Appendix A), then the last exponential in (4.35) is equal to 1 so that we get

$$H(x', \eta) = \text{rect}\left[\frac{x'}{X_1}\right] \int \Gamma_1(x', x, \eta) G_{10}(x' - x, \eta) dx \tag{4.38}$$

where $\Gamma_1(\cdot)$ is the range 1D-FT of $\gamma_1(\cdot)$. Therefore, by an inverse FT we have that

$$h(x', r') = \text{rect}\left[\frac{x'}{X_1}\right] \int \left\{ \mathbb{F}^{-1}\left[\Gamma_1(x', x, \eta) G_{10}(x' - x, \eta)\right] \right\} dx \tag{4.39}$$

As we can note, most part of the r-dependence of the $G(\cdot)$ function is already accounted for in the exponential term of (4.32), and only the residual r-dependence of $G_1(\cdot)$ is neglected. Therefore, the assumption on range size is not extremely restrictive (see Appendix A) so that it can be safely made for sliding spotlight.

However, if the aforementioned assumption is not verified (i.e. the TOPSAR case), we can still handle the r-dependence of $G_1(\cdot)$ by using the Taylor Series of ΔR around $r = r_0$, obtaining

$$\Delta R - \Delta R_0 \cong \left(\frac{r_0}{\sqrt{r_0^2 + (x' - x)^2}} - 1 \right) (r - r_0) \tag{4.40}$$

and we get

$$
\begin{aligned}
H(x',\eta) &= \mathrm{rect}\left[\tfrac{x'}{X_1}\right] \int G_{10}(x'-x,\eta) \\
&\qquad \left\{ \int \gamma_1(x',x,\bar{r}) e^{-j\eta\Omega(x'-x)\bar{r}} d\bar{r} \right\} dx \\
&= \mathrm{rect}\left[\tfrac{x'}{X_1}\right] \int \Gamma_1[x',x,\eta\Omega(x'-x)] G_{10}(x'-x,\eta) dx
\end{aligned}
\tag{4.41}
$$

where $\bar{r} = r - r_0$ and

$$
\Omega(x'-x) = \frac{r_0}{\sqrt{r_0^2 + (x'-x)^2}} \tag{4.42}
$$

Eventually, performing an inverse FT we get

$$
h(x',r') = \mathrm{rect}\left[\frac{x'}{X_1}\right] \int \left\{ \mathbb{F}^{-1} \Big[\Gamma_1(x',x,\eta\Omega(x'-x)) G_{10}(x'-x,\eta) \Big] \right\} dx \tag{4.43}
$$

leading to he block diagram of Fig. 4.7.

This is the method employed in the simulator, for both the sliding spotlight mode and for each burst of the TOPSAR mode. Note that the interpolation in the η-Fourier domain can be efficiently performed by using grid deformation [40] or the chirp-scaling algorithm [8] so that the proposed method shows no substantial increase of computational complexity with respect to the method of [42]. Actually, the proposed method can be also applied for the stripmap, scanSAR, and spotlight modes, but in those cases, it is not convenient with respect to the methods shown in the previous sections, which use a full 2D-FT approach.

The presented procedure is certainly appropriate to spaceborne sensors: in fact, it assumes a straight-line flight path that is a good approximation for a few kilometres portion of the elliptical orbit of a satellite platform.

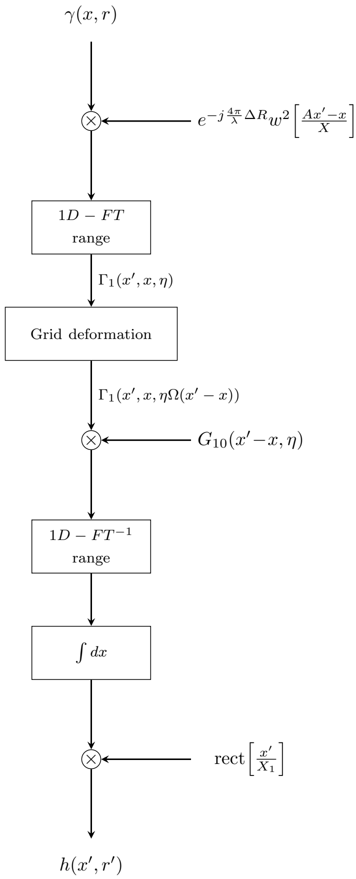

Figure 4.7. Block diagram of SAR raw signal simulation. In the limited-range-swath hypothesis, the grid deformation block can be removed.

Conversely, in the case of airborne sensors, appreciable deviations from the ideal trajectory may occur. Effects of these deviations can be easily accounted for by our simulation scheme since the azimuth processing is performed in time domain. Accordingly, it is sufficient to consider in (4.32), (4.33), and (4.35) the following expression for ΔR

$$\Delta R = \sqrt{[r + \Delta r(x', x, r)]^2 + (x' - x)^2} - r \tag{4.44}$$

where

$$\Delta r(x', x, r) = -d(x') \sin[\vartheta(x, r) - \beta(x')] \qquad d \ll r_0 \tag{4.45}$$

is the projection along the local LOS of the deviation with respect to the nominal trajectory at the sensor azimuth location x', with $d(x')$ and $\beta(x')$ define the shuttle displacement (see Fig. 4.8).

Accordingly, the equations (4.37), (4.40) and (4.42), respectively, becomes

$$\Delta R_0 = \sqrt{[r_0 + \Delta r(x', x, r_0)]^2 + (x' - x)^2} - r_0 \tag{4.46}$$

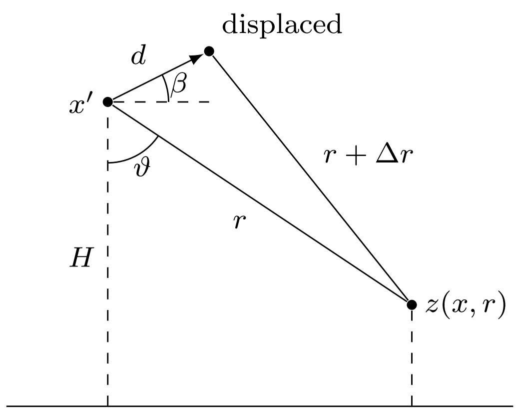

Figure 4.8. 2D lateral view geometry of the problem, accounting for trajectory deviation.

$$\Delta R - \Delta R_0 \cong \left(\frac{[r_0 + \Delta r(x', x, r_0)][1 + \Delta r'(x', x, r_0)]}{\sqrt{[r_0 + \Delta r(x', x, r_0)]^2 + (x' - x)^2}} - 1 \right)(r - r_0) \quad (4.47)$$

$$\Omega(x' - x) = \frac{[r_0 + \Delta r(x', x, r_0)][1 + \Delta r'(x', x, r_0)]}{\sqrt{[r_0 + \Delta r(x', x, r_0)]^2 + (x' - x)^2}} \quad (4.48)$$

where (see Appendix B)

$$\Delta r'(x', x, r_0) = \left. \frac{\partial \Delta r}{\partial r} \right|_{r=r_0} \cong \frac{-d(x') \cos[\vartheta(x, r_0) - \beta(x')]}{r_0 \tan[\vartheta(x, r_0)]} \quad (4.49)$$

To conclude this section, we want to remark that this method can simulate raw signals with any acquisition mode, accounting for trajectory deviations with no increase in the computational complexity. Moreover, no constraints on trajectory deviation amplitude are necessary (except that they are small compared to r_0, as it always happens in practice).

4.2.2 Performance Evaluation with Simulation Examples

In order to evaluate the performance of the proposed simulation algorithm, let us first compare its computational complexity (measured by the number of complex multiplications N_{1DFD}) with that one of a full time-domain direct approach (N_{TD}). Of course, in this analysis, we do not consider the generation of the reflectivity map $\gamma(\cdot)$, because it is the same in both approaches. We call N_1 the number of pulses within a burst length X_1, N the number of scene pixels within one azimuth footprint X, N_r the number of range pixels within the slant range swath S_r, and N_τ the number of samples of the transmitted pulse of duration τ. Therefore, we have

$$N_1 = X_1 \frac{f_p}{v} = \frac{X f_p}{v} \frac{1}{B} \tag{4.50}$$

$$N = \frac{X f_p}{v} \frac{1}{\max\{|A|, B\}} \tag{4.51}$$

$$N_r = S_r \frac{2 f_s}{c} \tag{4.52}$$

$$N_\tau = \tau f_s \tag{4.53}$$

where all the parameters have been introduced in the previous sections, except for f_s which is the *sampling frequency.*

If the raw signal $h(\cdot)$ is assessed in time domain, the efficiency of FFT codes is not exploited and the computational complexity is

$$N_{TD} \approx N_1 N N_r N_\tau \tag{4.54}$$

If we consider the proposed 1D-FT approach, we notice that computation of $\gamma_1(\cdot)$ requires $N_1 N N_r$ complex multiplications, and its 1D range FFT is calculated for each couple of values (x', x), so this step presents the computational complexity

$$N_1 N \frac{N_r}{2} \log_2 N_r \tag{4.55}$$

At this point, the matrix $\Gamma_1(\cdot)$ is multiplied by the function $G(\cdot)$ for every value (x', x, η) and then the inverse 1D range FFT of the updated matrix is calculated. This part exhibits the computational complexity

$$N_1 N N_r + N_1 N \frac{N_r}{2} \log_2 N_r \tag{4.56}$$

Therefore, the overall computational complexity of the algorithm showed in Fig. 4.7 is

$$N_{1DFD} \approx N_1 N N_r (2 + \log_2 N_r) \tag{4.57}$$

Consequently, by using the presented 1D Fourier domain approach, processing time is reduced by the factor

$$\frac{N_{1DFD}}{N_{TD}} = \frac{2 + \log_2 N_r}{N_\tau} \tag{4.58}$$

with respect to a time-domain simulation.

To give an idea of the quantities involved, let us consider $N_r = 8192$ and $N_\tau = 4096$. So, we obtain a processing time decrease factor of about $1/273$. In addition, we remark that if interpolation in the Fourier domain is needed, the numerator of (4.58) only slightly increases (the exact amount depends on the employed interpolation technique) so that the very large advantage of the proposed simulation scheme with respect to the time domain is maintained.

Let us move to show the accuracy of the simulated raw signals presenting some interesting examples.

First of all, we want to verify that the raw signal corresponding to a single scattering point, simulated by using the presented 1D-FT approach, agrees with the one obtained directly from the exact time-domain expression. In order to do this, we start to consider system parameters similar to those of the Sentinel-1 spaceborne sensor, operating in the TOPSAR mode (see the second column of Tab. 4.2.

In particular, we refer to a point scatterer placed at the center of the observed scene, that is at the coordinates $(x = 0, r = r_0)$. In Fig. 4.9 the results related to the phase error are depicted. The phase error is here the phase difference between the raw signal simulated by using the presented method and the one obtained via a full time-domain simulation.

We notice that that the absolute value of this phase difference is always smaller, and often much smaller, than $\pi/10$, thus leading to negligible

	Spaceborne	**Airborne**
Platform height (h)	693 km	6 km
Platform velocity (v)	7.5 km/s	0.142 km/s
Look angle (ϑ)	24 $degrees$	50 $degrees$
Azimuth antenna length (L)	12 m	0.9 m
Range antenna length (L_r)	0.7 m	0.141 m
Carrier frequency (f)	5.405 GHz	5.31 GHz
Pulse duration (τ)	50 μs	7 μs
Pulse bandwidth (Δf)	50 MHz	37.5 MHz
Sampling frequency (f_s)	50 MHz	37.5 MHz
Pulse repetition frequency (PRF)	1642 Hz	329 Hz
A	2.9	2.9
B	0.5	0.5
Azimuth size of the scene	16.8 km	2.804 km
Ground range size of the scene	92.5 km	6.392 km
Azimuth resolution (Δx)	17.4 m	1.302 m
Ground range resolution (Δy)	7.4 m	5.221 m
Raw signal azimuth size	1537 $pixels$	2716 $pixels$
Raw signal range size	15040 $pixels$	1488 $pixels$

Table 4.2. Main SAR system parameters used in the simulations.

effects. Fast small oscillations in the range cut are due to the stationary phase method approximation and to the well known Gibbs phenomenon.

Similar consideration can be done on the azimuth and range cuts of the amplitudes of the raw signals generated by using the two different approaches (see Fig. 4.10).

Similar comparisons for a point scatterer located at the azimuth and range borders of the illuminated scene provide almost identical results, as shown in Figs. 4.11 and 4.12 for the phase and the ambplitude cuts, respectively. The only differences with respect to the previous case are very

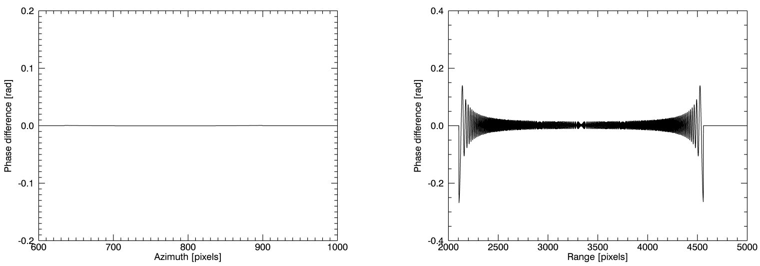

(a) (b)

Figure 4.9. Azimuth (a) and range (b) cuts of the phase error for a scatterer point located at the scene center $(x = 0, r = r_0)$.

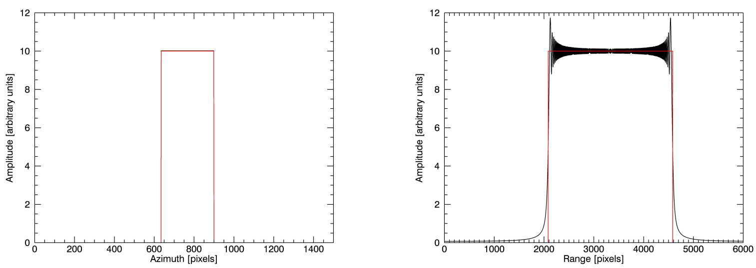

(a) (b)

Figure 4.10. Azimuth (a) and range (b) cuts of the amplitudes of the raw signals simulated by using the presented approach (in black) and the time-domain simulation (in red), for a scatterer point located at the scene center $(x = 0, r = r_0)$.

slight, negligible oscillations in the azimuth amplitude and phase cuts. Similar results are also obtained for different values of the system parameters.

A simulation to obtain an extended scene is now in order. We use the same spaceborne SAR system data of Tab. 4.2 (second column) and a "canonical" extended scene, which is a cone over a flat plane. Moreover, we assume that outside the fully resolved area, the scene is completely

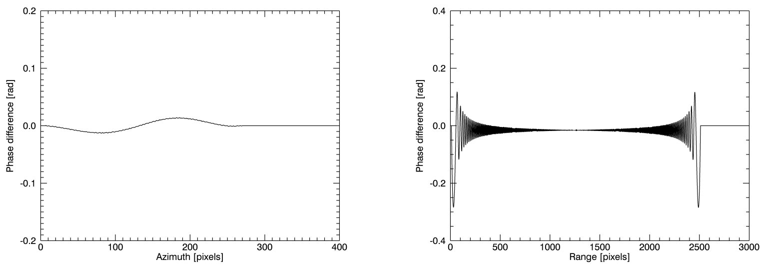

(a) (b)

Figure 4.11. Azimuth (a) and range (b) cuts of the phase error for a scatterer point located at the near range scene border ($x = -8000m, r = r_0 - 18300m$).

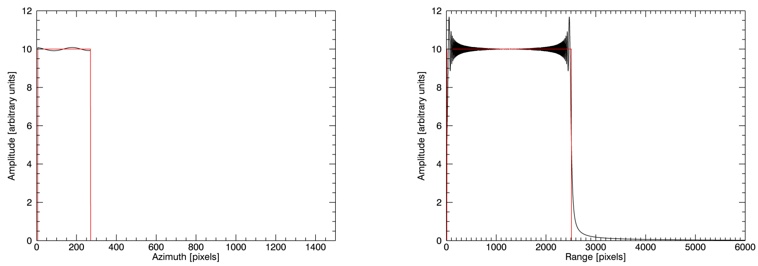

(a) (b)

Figure 4.12. Azimuth (a) and range (b) cuts of the amplitudes of the raw signals simulated by using the presented approach (in black) and the time-domain simulation (in red), for a scatterer point located at the near range scene border ($x = -8000m, r = r_0 - 18300m$).

absorbing. Corresponding raw signal has been generated and the image obtained by using a TOPSAR focusing algorithm is shown in Fig. 4.13.

As a final example of extended scene simulation, we investigate an actual scenario. In Fig. 4.14 is displayed the image obtained using the same system parameters of the previous simulations and providing as input to the simulator a DEM of the southern Apennines area in Campania, Italy.

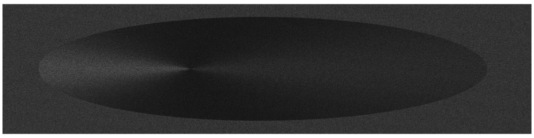

Figure 4.13. Amplitude image obtained by focusing a simulated raw signal of a canonical extended scene (a cone over a flat plane).

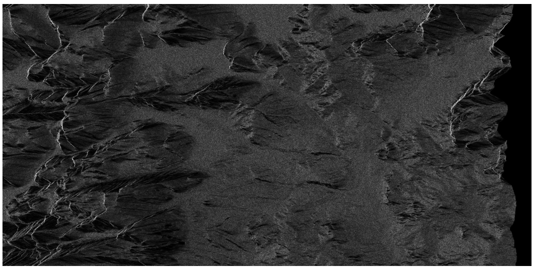

Figure 4.14. Amplitude image obtained by focusing a simulated raw signal of the Apennines area in Campania, Italy. A multilook of two has been applied in the range direction to obtain an almost square pixel.

Eventually, let us now consider an airborne sensor parameters (see third column of Tab. 4.2) operating in the TOPSAR mode, in the case of trajectory deviations. For a simpler comparison, we here consider a scattering point located at $(x = 0, r = r_0)$ (center of the investigated area) and sinusoidal deviations from the ideal flight path. In particular, the considered sinusoidal trajectory has a 1 m amplitude (when projected along the local line of sight) and a period of 157 m. These are quite strong deviations. In Fig. 4.15, we show the azimuth and range cuts of the phase error. Also in this case, it is always smaller, and often much smaller, than $\pi/10$, thus confirming the validity of the described method. About the amplitudes, results very similar to those of the spaceborne sensor with no trajectory deviations (see Figs. 4.10 and 4.12) are achieved.

A few last words are now needed about the processing time. In the

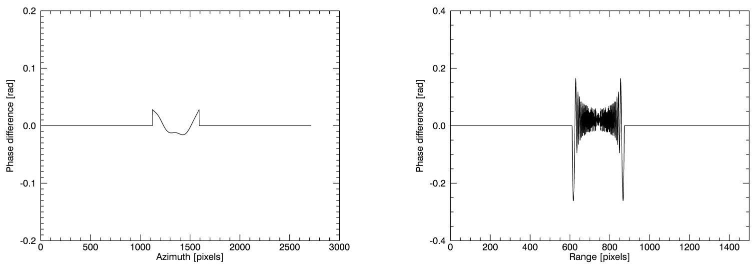

(a) (b)

Figure 4.15. Azimuth (a) and range (b) cuts of the phase error in the presence of sinusoidal trajectory deviations for a scatterer point located at the scene center ($x = 0, r = r_0$).

case of the simulation of the extended scene of Fig. 4.13, with a raw signal of 1537 (azimuth) $\times$ 15040 (range) samples, the raw signal simulation took about 40 min on a PC with an Intel Core 2 Duo Processor E8400 @ 3.00 GHz and 8 GB RAM. Note that time-domain processing of the same scene would require a processing time of the order of some days on the same PC.

Appendix A

In this Appendix, we want to calculate the conditions under which the approximation

$$\eta(\Delta R - \Delta R_0) \ll 1 \tag{4.59}$$

used in (4.38) and (4.39) holds. Of course, η is limited by the range bandwidth $bc\tau = 4\pi\Delta f/c$. For the second factor in (4.59) we have

$$\begin{aligned} \Delta R - \Delta R_0 &\cong \frac{(x'-x)^2}{2r} - \frac{(x'-x)^2}{2r_0} = \frac{(x'-x)^2}{2r_0}\left(\frac{r_0}{r} - 1\right) \\ &\cong -\frac{(x'-x)^2}{2r_0}(r - r_0) \end{aligned} \tag{4.60}$$

where

$$|x' - x| \leq \frac{|1-A|X_1 + X}{2} = \frac{X}{2}\Big(1 + \frac{|1-A|}{B}\Big) \tag{4.61}$$

and

$$|r - r_0| \leq \frac{S_r}{2} \tag{4.62}$$

where S_r is the slant range extension of the illuminated scene. Therefore, we ca write that

$$\Delta R - \Delta R_0 \leq \frac{1}{8}\Big(\frac{X}{r_0}\Big)^2\Big(1 + \frac{|1-A|}{B}\Big)^2\frac{S_r}{2} \tag{4.63}$$

and the final result is

$$\begin{aligned}
|\eta(\Delta R - \Delta R_0)| &\leq \tfrac{\pi\Delta f}{2c}\Big(\tfrac{X}{r_0}\Big)^2\Big(1 + \tfrac{|1-A|}{B}\Big)^2\tfrac{S_r}{2} \\
&= \tfrac{2\pi 2\Delta f}{c}\Big(\tfrac{2\lambda}{L}\Big)^2\Big(1 + \tfrac{|1-A|}{B}\Big)^2\tfrac{S_r}{64} \\
&= \tfrac{2\pi}{\Delta r}\Big(\tfrac{\lambda}{L/2}\Big)^2\Big(1 + \tfrac{|1-A|}{B}\Big)^2\tfrac{S_r}{64}
\end{aligned} \tag{4.64}$$

In practice cases, this phase term is much smaller than the upper limit of the expression (4.64), Accordingly, it is sufficient to consider the following, more conservative, condition

$$|\eta(\Delta R - \Delta R_0)| < \pi \Leftrightarrow S_r < \frac{32\Delta r\Big(\frac{L/2}{\lambda}\Big)^2}{\Big(1+\frac{|1-A|}{B}\Big)^2} \tag{4.65}$$

For example, in the case of an hypothetic high-resolution spaceborne sliding spotlight SAR system with $\lambda = 3cm$, $L = 6m$, $\Delta r = 1m$, $B = 1/6$ and $A = 1/2$, we have $S_r < 20km$. More or less, the same result is achieved for a spaceborne SAR system working in TOPSAR mode with $\lambda = 6cm$, $L = 12m$ and $\Delta r = 3m$.

To conclude, we note that the approximation in (4.40) amounts to neglect a term of the order of

$$\begin{aligned} &\Delta R - \Delta R_0 - \left(\frac{r_0}{\sqrt{r_0^2 + (x'-x)^2}} - 1 \right)(r - r_0) \cong \\ &\cong \frac{(x'-x)^2}{2r_0^3}(r - r_0)^2 \end{aligned} \tag{4.66}$$

In this case, the condition becomes

$$\begin{aligned} &\frac{2\pi}{\Delta r}\left(\frac{\lambda}{L/2}\right)^2 \left(1 + \frac{|1-A|}{B}\right)^2 \frac{S_r^2}{128 r_0} < \pi \Leftrightarrow \\ &\Leftrightarrow S_r < \frac{8\sqrt{\Delta r r_0}\left(\frac{L/2}{\lambda}\right)}{\left(1 + \frac{|1-A|}{B}\right)} \end{aligned} \tag{4.67}$$

For example, for the same aforementioned system parameters, wuth $r_0 = 1000km$, we have $S_r < 200km$.

Appendix B

In this Appendix, we want to derive equations (4.47)-(4.49) from equations (4.44)-(4.46). We start expanding the (4.44) around $r = r_0$ and arresting it at the first order:

$$\begin{aligned} &\Delta R - \Delta R_0 \cong \left.\frac{\partial \Delta R}{\partial r}\right|_{r=r_0} (r - r_0) \\ &= \left(\frac{[r_0 + \Delta r(x', x, r_0)]\left[1 + \left.\frac{\partial \Delta r(x', x, r)}{\partial r}\right|_{r=r_0}\right]}{\sqrt{[r_0 + \Delta r(x', x, r_0)]^2 + (x'-x)^2}} - 1 \right)(r - r_0) \end{aligned} \tag{4.68}$$

By using the (4.45), we can write

$$\left.\frac{\partial \Delta r(x', x, r)}{\partial r}\right|_{r=r_0} = -d(x') \cos[\vartheta(x, r_0) - \beta(x')] \left.\frac{\partial \vartheta(x, r)}{\partial r}\right|_{r=r_0} \tag{4.69}$$

From the Fig. 4.8 we know that

$$\vartheta(x,r) = \arccos\left(\frac{H - z(x,r)}{r}\right) \tag{4.70}$$

so that

$$\begin{aligned}
&\tfrac{\partial\vartheta(x,r)}{\partial r} = \tfrac{H - z(x,r) + r\frac{\partial z(x,r)}{\partial r}}{r^2 \sin[\vartheta(x,r)]} \\
&= \tfrac{1}{r\tan[\vartheta(x,r)]} + \tfrac{\frac{\partial z(x,r)}{\partial r}}{r\sin[\vartheta(x,r)]} \cong \tfrac{1}{r\tan[\vartheta(x,r)]}
\end{aligned} \tag{4.71}$$

where a modest topography assumption is made to achieve the last approximate equality. Hence, substituting (4.71) in (4.69), we obtain the equation (4.49). While, equation (4.48) is derived from (4.68). i.e., from (4.47).

This page intentionally left blank.

Chapter 5

Terrain Displacement Measurements via Synthetic Aperture Radar

5.1 Synthetic Aperture Radar Interferometry

Historically, the main purpose of the Interferometric Synthetic Aperture Radar (InSAR) is to restore the Digital Elevation Model (DEM) of an observed area [43]. The basic idea lies on imaging the same scene on the ground from two *slightly* different angles in such a way to have a stereoscopic vision.

As we have learned by the previous chapters, a SAR system can measure both the azimuth and range dimension of a target. Obviously, the knowledge of the target range r' is not sufficient to uniquely detect the position of that target and, consequently, its height from the reference plane. In fact, all the targets within the range beam and located on an equidistance curve are imaged at the same range position.

In order to overcome this kind of ambiguity, we can consider a second image obtained by a sensor that illumines the same area from a different position (Fig. 5.1).

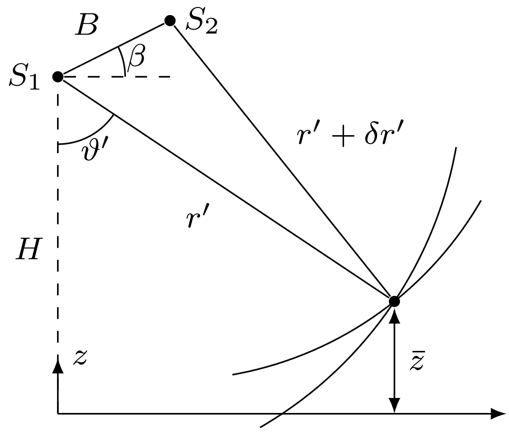

Figure 5.1. Stereoimaging system geometry in the plane orthogonal to the fight direction.

The distance B between the two sensors is referred to as *baseline*. The β angle between B and the y axis is referred to as *tilt angle*. The two images can be acquired by a single system equipped with two imaging sensors (one active and one passive), or using two repeat passes of just one imaging sensor system. Of course, in this latter case, it is important that the properties of the interested scene must remain unchanged within the time span of the two passes. Based on this, the ambiguity on the target location is totally solved: indeed, using the range distance information derived from the second system, only one point is located at distance r' and at distance $r' + \delta r'$ from the first and the second system, respectively. Therefore, a technique (called *stereometry*) to detect the height of a target on the reference plane can be derived.

Let us consider a point in the first image (referred to as the *master* image) at a range distance r' (see Fig. 5.1). We want to *search* for it in the second image (referred to as the *slave* image). Because of we can measure the target range position $r' + \delta r'$ on the slave, its height on the reference plane is retrieved from the following two equations:

$$(r' + \delta r')^2 = r'^2 + B^2 - 2Br' \sin(\vartheta' - \beta) \tag{5.1}$$

$$z = H - r' \cos \vartheta' \tag{5.2}$$

In other words, we evaluate ϑ' (the target *look angle*) from the (5.1) using the knowledge of r', $\delta r'$, B and β; then we use it in the (5.2) to determine the target height z.

We now ask ourselves what the achievable height accuracy is. If we assume that r' is exactly calculated and to perfectly know the orbital parameters (B,H and β), then the measurement accuracy depends only on the error occurring in the evaluation of $\delta r'$. This change depends on the range system resolution. In fact, higher the range resolution, better the range discrimination and, accordingly, higher the precision in the $\delta r'$ measurement. Therefore, from the (5.1) and (5.2) we have

$$\frac{\partial z}{\partial \delta r'} = \frac{\partial z}{\partial \vartheta'} \frac{\partial \vartheta'}{\partial \delta r'} = r' \sin \vartheta' \Big[- \frac{r' + \delta r'}{Br' \cos(\vartheta' - \beta)} \Big] \approx - \frac{r' \sin \vartheta'}{B \cos(\vartheta' - \beta)} \tag{5.3}$$

where we have used the *parallel ray approximation* $r' \gg B, \delta r'$. So, the height resolution depends on the ratio r'/B, which typically is very large in SAR systems. For a basic SAR sensor configuration working, for example, at C-band we get an accuracy of $1.5km$ which is impracticable for the most important applications.

The (5.3) suggests us that to improve the height resolution we need to increase the baseline length. This solution is generally not usable because of the presence of a multiplicative noise (so-called *spekle*) in the SAR images. The electromagnetic field backscattered from a resolution cell may have large variations when this is imaged from two very different view angles. So, an increase of the baseline length can generate large variations of the radiometric response, thus decreasing the accuracy in locating the same target in the two SAR images.

For this reason, the stereometric techniques are often unusable on the SAR systems and we have to move towards other solutions.

5.1.1 Interferometric Synthetic Aperture Radar Processing

A possible way to overcome the limitation of the stereometric method is to retrieve $\delta r'$ from the phase difference of the focused images (SAR *interferometry*). Based on what has been presented in chapter 3, the two focused signals, for not-normalized units, are:

$$\hat{\gamma_1}(x', r') = \iint \gamma(x, r) e^{-j\frac{4\pi}{\lambda}r} \mathrm{sinc}\big[a(x'-x)\big] \mathrm{sinc}\big[b(r'-r)\big] dx dr \tag{5.4}$$

$$\hat{\gamma_2}(x', r') = \iint \gamma(x, r) e^{-j\frac{4\pi}{\lambda}(r+\delta r)} \mathrm{sinc}\big[a(x'-x)\big] \mathrm{sinc}\big[b(r'-r-\delta r)\big] dx dr \tag{5.5}$$

From the (5.1) we have

$$\delta r' = \sqrt{r'^2 + B^2 - 2Br' \sin(\vartheta' - \beta)} - r' \tag{5.6}$$

and an identical expression is valid for δr in the (5.5), changing $r' \to r$ and $\vartheta' \to \vartheta$. The δr value is the range displacement of the generic investigated area in the two images. For the sake of simplicity, let us assume that the system bandwidth a and b are infinite in such a way that the sinc$(\cdot)$ functions in the (5.4) and (5.5) approach to the Dirac functions. If this is the case, we get

$$\hat{\gamma_1}(x', r') = \gamma(x', r')e^{-j\frac{4\pi}{\lambda}r'} \tag{5.7}$$

$$\hat{\gamma_2}(x', r') = \gamma(x', r' - \delta r')e^{-j\frac{4\pi}{\lambda}r'} \tag{5.8}$$

where $\delta r' = \delta r(r = r')$.

Accordingly, first of all, we have to perform a proper image registration

$$\hat{\gamma_2}(x', r') \rightarrow \hat{\gamma_2}(x', r' + \delta r') = \gamma(x', r')e^{-j\frac{4\pi}{\lambda}(r'+\delta r')} \tag{5.9}$$

Then, we multiply the master image by the complex conjugate of the slave one in such a way we can extract the phase information (*interferometric phase*):

$$\varphi(x', r') = \measuredangle\hat{\gamma_1}(x', r')\hat{\gamma_2}^*(x', r' + \delta r') = \frac{4\pi}{\lambda}\delta r' \tag{5.10}$$

where the symbol $\measuredangle$ represents the operator that return the *full* phase (that means the phase not restricted to the $]-\pi, \pi]$ interval).

As we can see, the information on the path difference $\delta r'$ is obtained from the phases of the target responses in the two SAR images. The accuracy on $\delta r'$ measurement is better than that one achievable by the stereometric systems leading to the centimeter or even the millimeter scale for the most common SAR sensors.

In addition, it is important to underline that to extract the desired path difference $\delta r'$ we need to properly register the two focused images (also referred to as *single-look complex*, SLC, images). This determine a paradox: indeed, we need the *a priori* knowledge on $\delta r'$ to set $r'+\delta r' \rightarrow r'$ in the slave image. But this paradox is just due to the considered hypotheses. In fact, if we relax the unlimited bandwidth assumption moving to the real case, the target response is *spread* over the resolution cell. So, two pixel *areas* (and not two single points) should be aligned and $\delta r'$ is an *average* value over the cell, weighted over the local backscattering coefficient. This pixel alignment can be implemented with an accuracy of a fraction of the pixel dimension. For this reason, $\delta r'$ is evaluated through a phase measurement, with an accuracy of the wavelength scale.

At this point, we also notice that all the discussion done lies on the ability to measure the phase φ. Anyway, complex data allow to measure φ_m restricted to the $]-\pi,\pi]$ interval, usually referred to as *wrappedinterferometric phase*. Therefore, techniques (so-called *phase unwrapping*) able to recover φ (*unwrapped phase*) from the wrapped one φ_m.

The overall InSAR processing is summarized in hlFig. 3 di pag 173 (184) ma forse meglio quello degli apppunti di gioia service.

5.1.2 Interferometric Phase Statistics

In this section, we introduce the interferometric phase statistics needed to take into account for the interferometric phase noise (detailed in section 5.1.3). Let us consider the on-dimensional case of Fig. 5.2, where $g_1(\cdot)$ and $g_2(\cdot)$ are the impulse responsens of the master and the slave channels, respectively. The output signals are

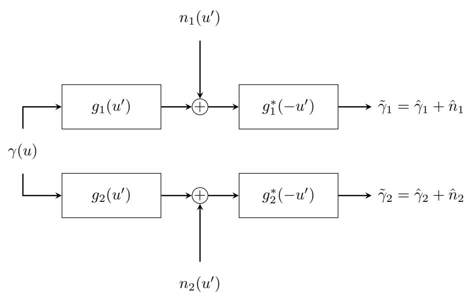

Figure 5.2. 1D model for derivation of InSAR statistics.

$$\begin{aligned}\tilde{\gamma}_1(u') &= \hat{\gamma}_1(u') + \hat{n}_1 \\ \tilde{\gamma}_2(u') &= \hat{\gamma}_2(u') + \hat{n}_2\end{aligned} \tag{5.11}$$

where $\hat{n}$ is the noise n filtered by the SAR data processing.

Some hypotheses on the characteristic of the involved random processes are now in order. We assume $\gamma(\cdot)$ to be a circular, zero mean Gaussian stationary white complex process with a power spectral density $2\sigma^2$. Therefore, its self-correlation function is

$$r_\gamma(u) = 2\sigma^2\delta(u) \tag{5.12}$$

The noise in the two channels to be mutually incoherent circular, zero mean Gaussian stationary white complex processes with a power spectral density $2n_0^2$ in such a way that

$$\begin{aligned}&r_{n_1}(u) = r_{n_2}(u) = 2n_0^2\delta(u) \\ &r_{n_1n_2}(u) = 0 \;\; \forall u\end{aligned} \tag{5.13}$$

And finally, $\gamma(\cdot)$ and n_k for $k \in \{1, 2\}$ to be mutually incoherent:

$$r_{n_1\gamma}(u) = r_{n_2\gamma}(u) = 0 \;\; \forall u \tag{5.14}$$

Because of the linear systems of Fig. 5.2 preserve the Gaussian distribution properties of the input signals, the self and joint statistics are totally described by their covariance matrix. In particular, their probability distribution function (pdf) is [44]

$$f(\tilde{\gamma}_1, \tilde{\gamma}_2) = \frac{1}{(2\pi)^2|\boldsymbol{C}|^{\frac{1}{2}}} e^{-\frac{1}{2}\boldsymbol{u}^T\boldsymbol{C}^{-1}\boldsymbol{u}} \tag{5.15}$$

where

$$
\begin{aligned}
&\boldsymbol{u}^T = [\tilde{\gamma}_{1r}, \tilde{\gamma}_{2r}, \tilde{\gamma}_{1i}, \tilde{\gamma}_{2i}] \\
&\tilde{\gamma}_1 = \tilde{\gamma}_{1r} + j\tilde{\gamma}_{1i} \\
&\tilde{\gamma}_2 = \tilde{\gamma}_{2r} + j\tilde{\gamma}_{2i} \\
&\boldsymbol{C} = \mathbb{E}[\boldsymbol{u}\boldsymbol{u}^T] = \sigma^2 \begin{bmatrix} q_1 & \Re[p] & 0 & -\Im[p] \\ \Re[p] & q_2 & \Im[p] & 0 \\ 0 & \Im[p] & q_1 & \Re[p] \\ -\Im[p] & 0 & \Re[p] & q_2 \end{bmatrix}
\end{aligned}
\tag{5.16}
$$

and

$$
\begin{aligned}
q_1 &= \tfrac{1}{\sigma^2}\mathbb{E}[\tilde{\gamma}_{1r}^2] = \tfrac{1}{\sigma^2}\mathbb{E}[\tilde{\gamma}_{1i}^2] \\
q_2 &= \tfrac{1}{\sigma^2}\mathbb{E}[\tilde{\gamma}_{2r}^2] = \tfrac{1}{\sigma^2}\mathbb{E}[\tilde{\gamma}_{2i}^2] \\
p &= \tfrac{1}{2\sigma^2}\mathbb{E}[\tilde{\gamma}_1\tilde{\gamma}_2^*]
\end{aligned}
\tag{5.17}
$$

To introduce a measure about the phase quality, it is now useful to refer to the *cross-correlation factor* χ between $\tilde{\gamma}_1$ and $\tilde{\gamma}_2$ defined as

$$
\chi = \frac{\mathbb{E}\left[\tilde{\gamma}_1\tilde{\gamma}_2^*\right]}{\sqrt{\mathbb{E}\left[|\tilde{\gamma}_1|^2\right]\mathbb{E}\left[|\tilde{\gamma}_2|^2\right]}} = \frac{p}{\sqrt{q_1 q_2}} = k e^{j\varphi_0}
\tag{5.18}
$$

In addition, for the equation (5.15) it is convenient to refer to the polar coordinates $\tilde{\gamma}_1 = V_1 e^{j\varphi_1}$ and $\tilde{\gamma}_2 = V_2 e^{j\varphi_2}$, obtaining

$$
\begin{aligned}
f(V_1, \varphi_1, V_2, \varphi_2) \quad = \quad & \frac{V_1 V_2}{4\pi^2\sigma^2\left(q_1 q_2 - |p|^2\right)} \\
& e^{-\frac{q_2 V_1^2 + q_1 V_2^2 - 2\sqrt{q_1 q_2} V_1 V_2 k \cos(\varphi_2 - \varphi_1 - \varphi_0)}{2\sigma^2(q_1 q_2 - |p|^2)}}
\end{aligned}
\tag{5.19}
$$

Integrating with respect to V_1 and V_2 we have

$$f(\varphi_1, \varphi_2) = \frac{1}{4\pi^2}\left(1 - \frac{|p|^2}{q_1 q_2}\right)\left[\frac{1}{1-k^2\cos^2(\varphi_2-\varphi_1-\varphi_0)} + \frac{k\cos(\varphi_2-\varphi_1-\varphi_0)\cos^{-1}[-k\cos(\varphi_2-\varphi_1-\varphi_0)]}{[1-k^2\cos^2(\varphi_2-\varphi_1-\varphi_0)]^{3/2}}\right] \tag{5.20}$$

Therefore, the pdf of the phase difference $\varphi = \varphi_2 - \varphi_1$ is

$$f(\varphi) = \frac{1-k^2}{2\pi}\frac{1}{1-k^2\cos^2(\varphi-\varphi_0)} \left[1 + \frac{k\cos(\varphi-\varphi_0)\cos^{-1}[-k\cos(\varphi-\varphi_0)]}{[1-k^2\cos^2(\varphi-\varphi_0)]^{1/2}}\right] \tag{5.21}$$

which is a periodic function of period 2π and it should be restricted between $-]\pi,\pi]$ to represent the pdf of the wrapped phase φ_m. The (5.21) is depicted in Fig. 5.3 for several values of k and $\varphi_0 = 0$. As we can observe, the phase distribution is less dispersed when $k \to 1$: so, higher k lower the contributions of the interferometric noise.

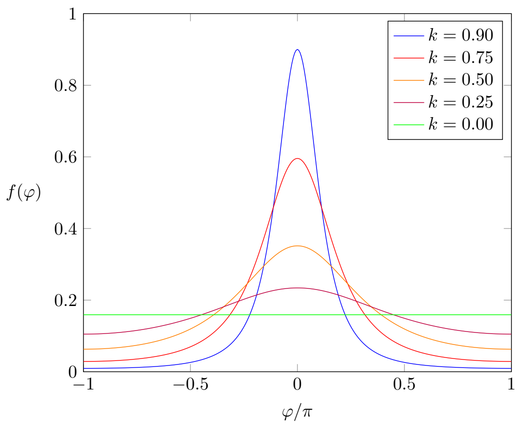

Figure 5.3. Interferometric phase pdf for different coherence values.

5.1.3 Decorrelation Effects

In this section, we want to study the cross-correlation coefficient χ between the two SLC images, which is needed to describe the statistics of the interferometric phase. In section 5.1.2, we have considered $\tilde{\gamma}_1$ and $\tilde{\gamma}_1$ two zero mean processes. Therefore, applying the (5.11) and (5.14) to the first channel of the Fig. 5.2, we have

$$\begin{aligned} \mathbb{E}[|\tilde{\gamma}_1|^2] &= \mathbb{E}[|\hat{\gamma}_1 + \hat{n}_1|^2] \\ &= \mathbb{E}\left[|\hat{\gamma}_1|^2\right] + \mathbb{E}\left[|\hat{n}_1|^2\right] = \mathbb{E}\left[|\hat{\gamma}_1|^2\right]\left(1 + \tfrac{1}{SNR_1}\right) \end{aligned} \tag{5.22}$$

where SNR_1 is the output signal-to-(thermal)-noise ratio on the first channel. The same is valid for the second channel. Moreover, due to the independence of signal an noise in both the channels, we have

$$\mathbb{E}\left[\hat{\gamma}_1\hat{\gamma}_2^*\right] = \mathbb{E}\left[\tilde{\gamma}_1\tilde{\gamma}_2^*\right] \tag{5.23}$$

and the cross-correlation χ becomes

$$\chi = \chi_g \chi_n \tag{5.24}$$

where

$$\chi_g = \frac{\mathbb{E}\left[\hat{\gamma}_1\hat{\gamma}_2^*\right]}{\sqrt{\mathbb{E}\left[|\hat{\gamma}_1|^2\right]\mathbb{E}\left[|\hat{\gamma}_2|^2\right]}} \tag{5.25}$$

is the *geometric decorrelation term* and

$$\chi_n = \frac{1}{\sqrt{\left(1 + SNR_1^{-1}\right)\left(1 + SNR_2^{-1}\right)}} \tag{5.26}$$

is the *thermal noise*. In particular, it is possible to explicit χ_g as follow

$$\begin{aligned}\chi_g &= \tfrac{ab}{\pi^2} e^{j\frac{4\pi}{\lambda}\delta r'} \iint e^{j\left[\frac{4\pi}{\lambda}\left(\delta r - \delta r'\right) - \Delta\xi_d p\right]} \mathrm{sinc}[ap]\mathrm{sinc}[bq] \\ &\quad \mathrm{sinc}\big[a\big(p - u'_x + \delta x'\big)\big]\mathrm{sinc}\big[b\big(q - u'_r + \delta r\big)\big]\, dp dq\end{aligned} \tag{5.27}$$

where δr is function of q.

At this point, in order to derive a relationship between the range changes at the cell center $\delta r'$ and its value δr within the resolution cell (see Fig. 5.1), the height profile must be specified. If we consider the height profile as a linear function with a slop equal to $\tan\Omega_t$, we can write

$$\delta r - \delta r' \approx \frac{B_\perp}{r'}(r' - r)\cot(\vartheta' - \Omega_t) = -k_\Omega(x', r')q \tag{5.28}$$

where $B_\perp = B\cos(\vartheta' - \beta)$. In addition, by letting

$$\begin{aligned}\chi_x(u'_x) &= \tfrac{a}{\pi}\int \mathrm{sinc}[ap]\mathrm{sinc}\big[a\big(p + m'_x\big)\big] e^{-j\Delta\xi_d p} dp \\ \chi_r(x', r', u'_r) &= \tfrac{b}{\pi}\int \mathrm{sinc}[bq]\mathrm{sinc}\big[b\big(q + m'_r\big)\big] e^{-j\frac{4\pi}{\lambda}k_\Omega q} dq\end{aligned} \tag{5.29}$$

with $m'_x = \delta x' - u'_x$ and $m'_r = \delta r' - u'_r$, we can rewrite the (5.27) as follow

$$\chi_g \approx \chi_x \chi_r e^{j\frac{4\pi}{\lambda}\delta r'} \tag{5.30}$$

In order to better detail the different type of decorrelation, we need to compute χ_x and χ_r. Following the analysis described in [8], we have:

$$\chi_r(r', u'_r) = \Lambda\Big[\frac{2\pi}{\lambda b}k_\Omega\Big]\mathrm{sinc}\Big[m'_r\Big(b - \frac{2\pi}{\lambda}|k_\Omega|\Big)\Big] e^{j\frac{2\pi}{\lambda b}k_\Omega m'_r} \tag{5.31}$$

$$\chi_x(u'_x) = \Lambda\Big[\frac{\Delta\xi_d}{2a}\Big]\mathrm{sinc}\Big[m'_x\Big(a - \frac{|\Delta\xi_d|}{2}\Big)\Big] e^{j\frac{\Delta\xi_d}{2}m'_x} \tag{5.32}$$

The first kind of decorrelation is due to the m'_x and m'_r terms of the (5.31) and (5.32) and it is referred to *misregistration decorrelation*. The misregistration errors cause a decrease in the cross-correlation coefficient amplitude and, accordingly, an increase in the interferogram noise contribution. If $k_\Omega = 0$, we have a complete decorrelation when $m'_r = \pi/b$, that means that the range misalignment is equal to the range resolution. In the same way, if $\Delta\xi_d = 0$, a full decorrelation is achieved when $m'_x = \pi/a$, that is when the azimuth misalignment is equal to the azimuth resolution.

Anyway, the most critical error for the InSAR system is the *spatial decorrelation*. It lies on the fact that the same ground resolution cell is imaged from two different look angles. In order to find the terms from which the spatial decorrelation depends, we consider the case of perfect registration. Therefore, the (5.31) becomes

$$\chi_r(x', r') = \Lambda\Big[\frac{2\pi}{\lambda}\frac{k_\Omega}{b}\Big] = \Lambda\Big[\frac{2\Delta r}{\lambda}\frac{B_\perp \cot(\vartheta' - \Omega_t)}{r'}\Big] \tag{5.33}$$

where, as usual, we have indicated by Δr the range resolution. From the (5.33) we notice that the spatial decorrelation effect increases at the increasing of the baseline length. We can define a *critical baseline* such that $\chi_r = 0$ for $\Omega_t = 0$ (no slope):

$$B_{\perp c} = \frac{\lambda}{2\Delta r}\frac{r'}{\cot(\vartheta')} \tag{5.34}$$

In this case, the phase noise is uniformly distributed in $]-\pi, \pi]$ and the interferometric signal is completely unreliable.

The term $\Delta\xi_d \neq 0$ (the case of a presence of a squint angle) is responsible of the *frequency decorrelation* (or *Doppler centroid decorrelation*). This is more evident if we move to the spectral domain. Indeed, observing the Fig. 5.4, images generated from the raw data pair are relative to a different spectral portion of the reflectivity function. No spectral overalapping is present in the azimuth direction if $|\xi_{d2} - \xi_{d1}| > 2a$, where ξ_{di} for $i \in \{1, 2\}$

has been well defined in the equation (3.64) of the section 3.2.

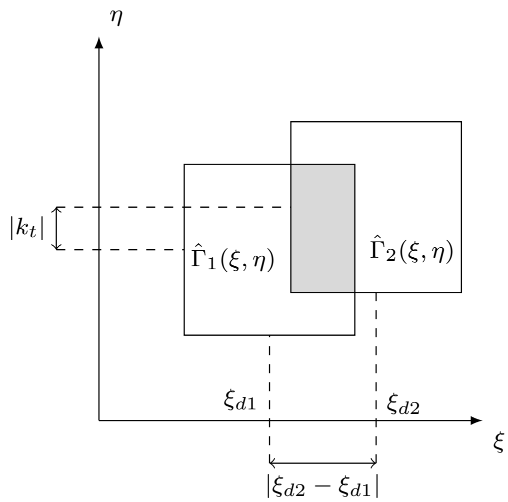

Figure 5.4. Frequency shift for InSAR signals.

While, the range spectral shift is due to the presence of an angular diversity in the plane orthogonal to the flight path. As we can see by the Fig. 5.4, no overlapping in the range domain is present if $|k_t| = |4\pi k_s/\lambda| > 2b$, where $k_s = -(B_{\perp 0}/r_0)\cot(\vartheta_0 - \bar{\Omega}_t)$, being $\bar{\Omega}_t$ the mean terrain slope over the whole imaged swath and $B_{\perp 0} = B_{\perp}(\vartheta' = \vartheta_0)$ with ϑ_0 the look angle at the center of the scene.

Spatial and frequency decorrelations are here explained as coherence loss due to the spectral misalignment effects. A reduction of this noise can be achieved, at the cost of a worsening in resolution, by using only the spectra common portion in the two interferometric channels [45].

The last type of error, is known as *temporal decorrelation* and it is present when we use the repeat pass mode. If this is the case, the $\gamma(\cdot)$ function (describing the scene backscattering properties) becomes time dependent and an additional phase changes between the $\hat{\gamma}_1(\cdot)$ and $\hat{\gamma}_2(\cdot)$

signals are present. This kind of decorrelation is very difficult to manage from a statistical viewpoint [46]. Typically, it is related to weather changes. In fact, arid zones are less affected by this phenomenon than the vegetated ones where even wind direction introduces a variable leaves orientation and, accordingly, a changing in the $\hat{\gamma}(\cdot)$ function. In addition, it is evident that the temporal decorrelation is dependent on the wavelength. For this reason, lower frequencies (for example, sensors working at L- or P-band) are preferred in vegetated areas. Instead, X-band antennas are suggested to get a better height accuracy in arid regions. Graphs of the coherence factor k that include temporal decorrelation effect (also referred to as *coherency maps* [47]) are very useful to get an estimate of this type of decorrelation.

5.2 Differential Interferometric Synthetic Aperture Radar

Differential interferometric SAR (DInSAR) is a technique able to detect surface displacements on the centimeter scale. Let us consider the two-pass InSAR geometry in the plane orthogonal to the antenna direction of the Fig. 5.5. Assume that a ground target displacement (d_{LOS}) occurs between the two passes, in such a way that r'_{sd} is the target range in the second pass and r'_s is the one relevant to the same area but in absence of the surface movement. Therefore, the interferometric phase is given by:

$$\varphi = \frac{4\pi}{\lambda}\left(r'_{sd} - r'\right) \Rightarrow \frac{\lambda\varphi}{4\pi} = r'_{sd} - r'_s + r'_s - r' = \delta r'_d + \delta r' \tag{5.35}$$

where $\delta r'_d$ is the contribution to the path difference due to the target motion and $\delta r'$ is the topographic height profile (that is the path difference when the ground displacement is absent).

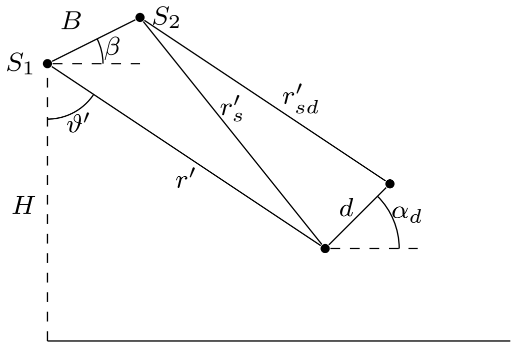

Figure 5.5. DInSAR geometry in the plane orthogonal to the antenna trajectory.

In the ideal case on which the two passes occur exactly on the same orbit ($B = 0$), the topographic contribution is equal to zero and we have that

$$\delta r'_d \approx d \sin(\vartheta' - \alpha_d) \tag{5.36}$$

The equation (5.36) shows that $\delta r'_d$ is equal to the displacement component parallel to the look direction, also known as *LOS displacement* component (d_{LOS}). In this ideal case, the DInSAR technique provides a LOS displacement phase accuracy on the order of fractions of λ, but the real situation ($B \neq 0$) requires two aspects to be taken into account: the topographic term $\delta r'$ and the noise term.

About the former, the using of a small baseline is recommended in order to limit the topographic contribution in the (5.35). Indeed, if the baseline is sufficiently small, we can obtain a precise estimate of $\delta r'$ and, consequently, a good separation between the topographic and the displacement terms. For instance, let us consider a given DEM with a $\sigma_z = 30\ m$ accuracy and a perpendicular baseline component of $B_\perp = 100\ m$. So, inverting the (5.3), the corresponding accuracy on $\delta r'$ is equal to 1 cm and, accordingly, this is the error passed to $\delta r'_d$ after that the topographic term $\delta r'$ has been subtracted.

About the noise contribution, two main causes has to be taken into account. For first, the decorrelation of images between the two passes (as showed in section 5.1.2). This is a crucial assumption for the DInSAR techniques because of the surface displacements are usually related to the scattering variations, for example, landslides. Anyway, this aspect is less serious for other applications such as fault movements [48, 49], slow ice movements [50] and volcanic areas deformations [51, 52]. Secondly, another source of error is related to the change of the atmospheric conditions from one pass to the other. Indeed, rain, clouds, and so on, modifies the electromagnetic wavelength during the two passes producing possibly severe errors (see equation (5.35)).

These aspects limited the development of the operational use of the DInSAR method for about a decade: in fact, it was only at the beginning of the 2000 that this technique reached a sufficient reliability. Two key factors allowed the increasing of the DInSAR applications: the devising of phase unwrapping algorithms able to work with "sparse data" [53], and the availability of long historical series of SAR data. The former allowed to consider only the high-coherence points on SAR images in the processing of data; the latter allowed researchers to develop parameter fitting methods to manage large amount of SAR images of the same area, acquired at different times, in order to filter out the "atmospheric" noise and, hence, to isolate the phase term corresponding to terrain displacement.

At this aim, two main different classes of methods have been devised: the *Permanent Scatterers* (PS) approach [54, 55], and *Small Baseline Subset* (SBAS) approach [56–60].

The PS strategy is based on the phase history of a limited number of very highly coherent pixels, corresponding to scene point-like elements characterized by a very stable electromagnetic scattering behaviour over time and over incidence angle. This allows to use large sets of SAR images, also with very large temporal and spatial baselines; consequently, a very high accuracy on the measured displacement velocity of the selected points can be obtained.

On the contrary, SBAS approach considers sets of SAR acquisitions with small spatial baselines in order to be able to take into account also distributed targets with sufficiently high coherence. Therefore, in this case, a reasonable accuracy on a much larger number of pixels is obtained.

However, in both approaches, the resulting accuracy depends both on the spatial density of coherent pixels and on the number of SAR images used. In fact, remarkable results have been obtained by the DInSAR technique in monitoring subsidence and landslides in urban areas or other little vegetated zones. An example is the case study presented in the next section, leading us to the second main contribution achieved within the Ph.D. degree.

5.2.1 DInSAR Application by Using Sentinel-1 Data

The monitoring of subsidence phenomena, caused by the reduction of fluvial sediments in coastal areas as well as in zones close to rivers, dams and so on, is a well-known problem in the remote sensing community. In fact, the quantification of the displacement rate on these areas is a crucial aspect, not only for the natural environment itself but also for the humans activities. The following activity aims to explore the capability of the DInSAR technique, exploiting Sentinel-1 (S1) TOPS data for the period 2014-2019, on two specific target sites here described.

Study Areas: Fiumicino Airport and Brumadinho Dam

Fiumicino is an area located on the southwest of the city of Rome, close to the Tevere river delta and coastal plain. This area is basically known because it includes the main airport of the city, the international airport “Leonardo da Vinci”, which has more than 40 million passengers per year. Due to the alluvial settlings around the Tevere river, many subsidence phenomena affect the area, making it potentially dangerous for civil infrastructures. In fact, many recently man-made structures suffer problems related to this: this is the well-known case of the “Leonardo Da Vinci” airport.

On January 25th 2019, the tailings dam n.1 of Corrego do Feijao iron mine, in the state of Minas Gerais close to Brumadinho in the metropolitan region of Belo Horizonte (in southeastern Brazil), suddenly failed releasing almost 12.000.000 m^3 of tailings in a big burst. The muddy wave traveled approximately 7 km downhill until reaching the Paraopeba river, destroying a bridge of the mine’s railway branch and spreading through several areas of the local community of Vila Ferteco, near the town of Brumadinho. Tailings dams are structures that hold mining waste, which must be properly stored for environmental reasons. Built in 1976, the Brumadinho dam was 86 meters high with a crest length of 720 meters where the disposed tailings occupied an area of about 250.000 m^2. The dam used the upstream method, which, although common, is the least safe, according to the experts. Upstream method is the process where the dam uses the tailings itself to lift the mud up in steps. Therefore, the structure at Brumadinho strained the very definition of “dam”. It had no separate concrete or metal wall to hold back its contents. Instead, the structure, relied on the lake of mud to remain solid enough to contain itself. Such type of dams makes them vulnerable to a potentially devastating process, called liquefaction. When this happens, a solid material can abruptly become a murky liquid. Even little changes (for example, an increase in water content because of heavy rains, or poor management) can create enough internal pressure to push apart the solid tailings and liquefy the mud. However the reasons of the failure are not yet clear, but the slope of the dam seems to have undergone a sudden rotational failure that spread over the entire width and height of the dam. There are no reports of any external events that are typically known to trigger such failures, like earthquakes or heavy rainfall. In this case, the trigger might have been the drilling of a monitoring well that was ongoing in the middle of the slope as it collapsed. Information coming up in early February 2019 appears to confirm that the safety factor of the dam was intolerable low and that there were serious deficiencies with monitoring of the dam stability. Among that, the erosion of the downstream embankment due to damaged surface channels, the damage of draining tubes and improper installation of drains.

Methodology

In order to monitor areas like those before described, we have exploited a multi-temporal DInSAR technique, based on the Singular Value Decomposition (SVD) method [61, 62].

To investigate the deformation phenomena occurring on Fiumicino Airport area, we have used a dataset of 299 Copernicus S1 SAR data collected from the beginning of the mission (on the October 2014) up to the end of February 2019. In particular, 114 acquisitions in descending orbit (track number: 95) and 185 acquisitions in ascending orbit (track number: 117), see Tab. 5.1. These are not the all acquisitions covering the Area-Of-Interest (AOI), but we have discarded the ones where the AOI laid on the

Sentinel-1 dataset	**Fiumicino airport**		**Brumadinho dam**	
	Ascending	Descending	Ascending	Descending
# of acquisitions	185	114	-	108
Track	117	95	-	53
Acquisition period	10/2014 - 02/2019		01/05/2015 - 22/01/2019	

Table 5.1. Sentinel-1 dataset used in this activity.

limit of the footprint. Considering the higher number of the used acquisitions with respect to the discarded ones and their density in the period analysed, we retain that the final results are not effected by this choice.

Instead, for the target site of the Brumadinho Dam, 108 acquisitions of the track 53 only for the descending orbit are available. As we can note in Tab. 5.1, they cover a time span of a little more than 3.5 years. In order to identify possible structure anomalies using the DInSAR technique, we have considered the acquisitions up to January 22th 2019, immediately before the collapse of the dam. The SAR acquisitions geometry for each track and each target site is depicted in Figs. 5.6, 5.7 and 5.8.

Due to this large amount of data to be store and process, it has been necessary to have a proper amount of resources both in terms of hardware and software. For this activity we have employed resources provided by the ESA Research & Service Support. In particular, it has been used a Virtual Machine (VM) running on cloud with the following specifications:

Figure 5.6. SAR acquisitions geometry for the AOI of Fiumicino airport in ascending orbit.

Figure 5.7. SAR acquisitions geometry for the AOI of Fiumicino airport in descending orbit.

Figure 5.8. SAR acquisitions geometry for the AOI of Brumadinho dam in descending orbit.

- RAM: 32 GB
- CPUs: 8

- HDD: 1 TB

The entire DInSAR processing chain can be splitted in two main parts (see Fig. 5.9) which are execute on two different hardware and software environments.

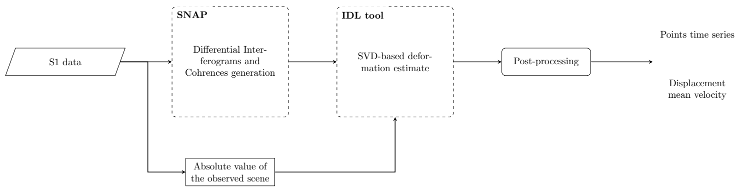

Figure 5.9. General flowchart of the adopted methodology.

The first goes from the download of the data up to the geocoded differential interferograms and cohrences generation. It is implemented using the ESA SentiNel Application Platform (SNAP) software on the before described VM. SNAP is widely used within the scientific community for many reasons: it provides multi-mission toolbox supporting both SAR and optical data processing; it is well integrated with other useful tools (e.g. the Snaphu tool used in this work for the phase unwrapping); but it is especially a free of charge and an open source tool, based on Python programming language, and it can be modified by the users if necessary.

The second part of the processing chain concerns the tool for monitoring the temporal evolution of the surface deformations. It is implemented in IDL language and executable on a Local Machine (LM) with the following specifications:

- RAM: 16 GB
- CPUs: 4
- SSD: 256 GB

This tool is suitable both for geocoded and not geocoded images. In order to take advantage of the greater resources of the employed VM with respect to the LM ones, we have chosen to perform the geocoding phase via the first part in the block scheme of Fig. 5.9. Moreover, to reduce the transfer time of the products from the VM to the LM, a proper subset based on geographic coordinates has been performed (but it is not strictly necessary). As we can see by the Fig. 5.9, this tool takes as input the differential interferogram pairs, the relative cohrences and the absolute value of the observed scene (used just as background in order to better identify the *reference area* for the DInSAR measurements), and it provides as output a Three-Dimensional (3D) matrix of the deformation estimations. In other words, it provides a stack of matrices each of them represents the deformation estimations on the specific AOI (space-dimension). The third dimension is the time-dimension and it corresponds to the acquisition dates.

On the basis of the aforementioned considerations, we can now briefly explain the main steps of the implemented technique. Due to the available hardware/software resources, we start to download and process a stack of more or less 30 S1 Interferometric Wide SLC acquisitions per time. This allow us to have enough memory space not only to store some intermediate products during the processing, but also to well manage any computational overheads. Moreover, it is worthwhile to note that, typically, 30 acquisitions cover a time span of six months (especially considering the twin S1-A and S1-B satellites). Because of the orbital tube of the S1 interferometric dataset is much lower than the critical baseline, it is possible to avoid any constrain on the spatial baseline and allows us to select the interferometric pairs taking into account only the minimization of the temporal decorrelation effects. Therefore, let us consider $N + 1$ the number of the SAR images and M the number of the interferograms generated: if $M = N$, then we move towards a method very similar to the PS technique [54, 55];

if $M > N$, then we move towards a method very similar to the SBAS technique [56–60]. In particular, this last one has been the choice for this activity but we have only one spatial subset [63].

To give an example of the selection criteria of the interferometric pairs, let us consider only 10 acquisition dates of the entire exploited dataset: let us label them by letters from A to J. So, a possible choice for the interferometric pairs generation is depicted in Fig. 5.10. For this activity we have generated 827, 287 and 176 interferograms, for Fiumicino ascending track, Fiumicino descending track and Brumadinho descending track, respectively.

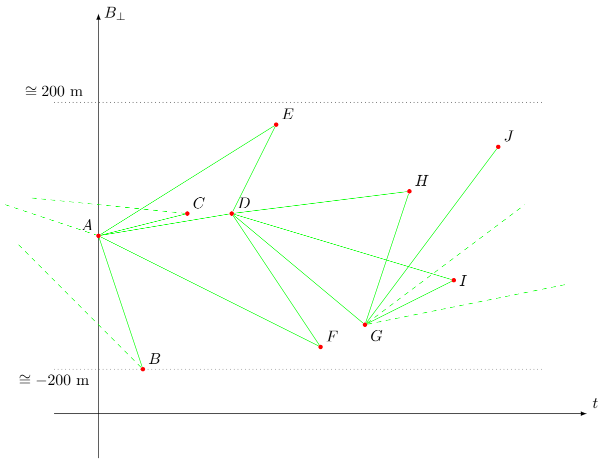

Figure 5.10. Example graph of the interferograms pairs selection.

The processing performed via SNAP consists of three main parts, as we can see in the block diagrams of Fig. 5.11. Each block (except for the SNAPHU [64] unwrapping block) is a SNAP tool whose main setting parameters, changed with respect to the default values, are shown in Tab. 5.2, 5.3 and 5.4.

With regards to these tables, some clarifications are now in order. In particular, the selection of the subswath where the AOIs lies is manually

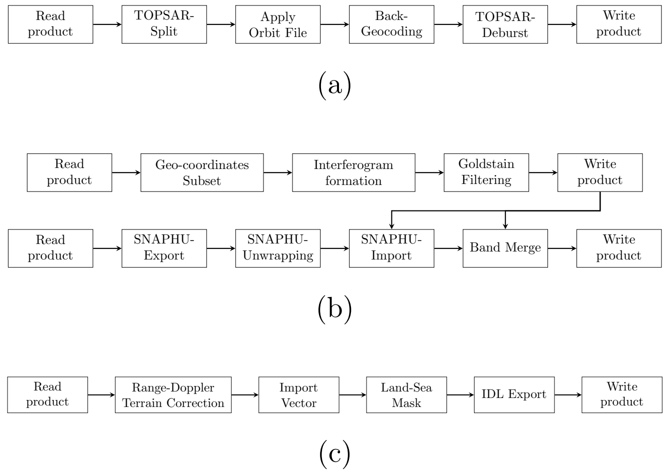

Figure 5.11. Exploded view of the three main parts (a),(b),(c) of the SNAP processing.

	Setting parameter	**Value**
TOPSAR-Split	Fiumicino descending subswath	IW1
	Fiumicino ascending subswath	IW2
	Brumadinho descending subswath	IW1
	Polarization	VV
	Bursts	1-9
Apply Orbit File	Orbit State Vectors	Sentinel Precise
	Polynomial Degree	3
Back-Geocoding	DEM	SRTM 3 sec
	DEM resampling method	Bilinear
	External DEM No Data value	0.0
	Mask out area without elevation	true
TOPSAR-Deburst	Selected polarizations	VV

Table 5.2. Setting parameters of the part (a) of the SNAP processing.

performed. Based on the time available for this activity and on the limited number of the target to be analyzed, it has not been necessary writing an

	Setting parameter	**Value**
Geo-coordinates Subset	subSamplingX	1
	subSamplingY	1
Interferogram formation	Subtract Flat Earth Phase	true
	Include Coherence	true
	Square Pixel	true
	Subtract TopographicPhase	true
Goldstein Filtering [65]	Alpha	1.0
	Use Coherence Mask	false
	Coherence Threshold	0.2
SNAPHU-Export	Statistical-Cost Mode	DEFO
	Initial Method	MCF
	Number Of Tile Rows and Cols	10
	Number Of Processors	8
	Row and Col Overlap	100
	Tile Cost Threshold	500
SNAPHU-Import	Do Not Keep Wrapped	true
Band Merge	Geographic Error	1.0e-5

Table 5.3. Setting parameters of the part (b) of the SNAP processing.

ad hoc code. But certainly, in order to provide a more extensive service, it can be an efficient solution. The coregistration step [66] use the SRTM 3 arc-sec DEM masking out the areas with no elevation. We have chosen this DEM in order to have a more reliable comparison with most of the works on this application. Further, because of the obtained wrapped interferograms are affected by noise dependent on several causes (some inaccuracies in the DEM used, the changing of the atmosphere from an acquisition to another, the decorrelation effects, processing errors, and so on), it is necessary to filter the interferograms products. In this study we have used the Goldstein filtering [65] discarding the pixel where the coherence value is less than 0.2 (in general, under this value the phase information can be considered completely lost).

	Setting parameter	Value
Terrain Correction	Pixel Spacing in Meter	20.0
	Pixel Spacing in Degree	1.796e-4
	Map Projection	WGS84
	No data Value at Sea	true
	Save Incidence Angle From Ellipsoid	true
Import-Vector	Vector File	Shapefile
	Separate Shapes	true
Land-Sea Mask	Land Mask	false
	Use SRTM	true
	Invert Geometry	false
	Shoreline Extension	0
IDL-Export	Format Name	ENVI

Table 5.4. Setting parameters of the part (c) of the SNAP processing.

Eventually, the first part of the processing chain provides for the geocoding task, defining the output square pixel spacing at 20 m spatial resolution (which is commonly used in literature for InSAR applications [67–69]).

Once the unwrapped differential interferograms and the coherence maps have been generated, we can put them in input to the monitoring displacements tool. It basically solves the mathematics problem well formulated in [59] using the approach described in Fig. 5.12, where the meaning of the matrices $\boldsymbol{A}$ and $\boldsymbol{B}$ is well defined in [59].

As we know, the phase unwrapping is performed up to an additive constant, which is different for each differential interferogram and this could lead to wrong results in the displacements estimation. Therefore, from an application point of view, it is necessary to identify an area, possibly close to the AOI, whose deformation is zero (*reference area*). If the AOI is characterized by movements of the ground, then the results obtained are the movements relative to the *reference area*. The choice of the *reference area* have also to take into account the coherence maps associated to each

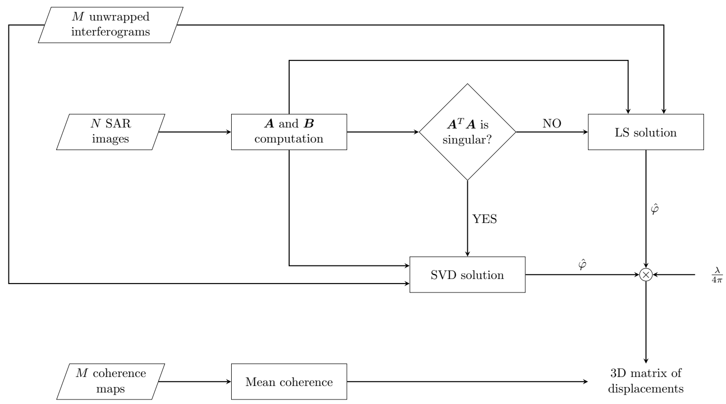

Figure 5.12. Exploded view of the IDL monitoring displacement tool.

interferogram. In fact, because of the unwrapped phase values are known only for that points whose coherence values exceed a given threshold, it is suitable that also the *reference area* remains consistent (that means value of its coherence exceeds the threshold) in all the interferograms. So, the additive constant to be removed is evaluated as the median value of the unwrapped phases in this points within the *reference area*. After that, the displacement values are available in form of a 3D IDL matrix (e.g. *matrix.img*). From an implementation point of view, the tool consists of several *routines* (IDL files with extension *.pro*), running by command line through a batch file (*batch.go*), which perform the block scheme of Fig. 5.12.

In order to mitigate the presence of an undesired atmospheric phase component (which can mask the actual deformation values out), a filtering operation has been performed as post-processing. It consists on the cascade of an high-pass filter performed in the spatial domain and a low-pass filter with respect to the time variable. Both these operations are implemented as routines in IDL language.

Eventually, once the deformation measurements have been obtained, we are able to merge the displacement information of different orbital positions and to separate one from another the deformation components, themselves [70]. To this end, let us suppose to have two different viewing angles, as depicted in Fig. 5.13. Therefore, the deformation components, measured

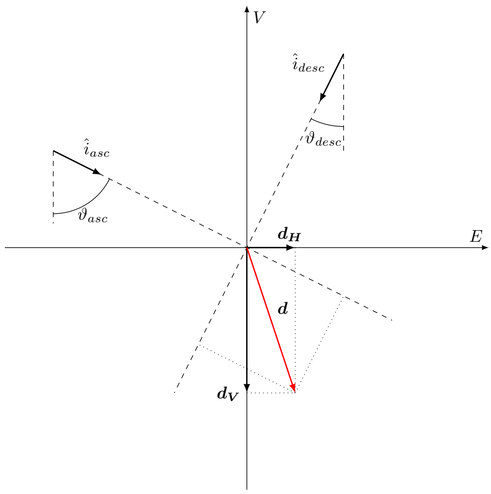

Figure 5.13. SAR geometry in the Vertical-East (V, E) plane with the displacement vector $\boldsymbol{d}$ in red, its two LOS projection and the vertical $\boldsymbol{d_V}$ and the horizontal $\boldsymbol{d_H}$ deformation components highlighted.

by the SAR sensor along the two LOS, can be expressed as the following

$$\begin{cases} d_{asc} = \boldsymbol{d} \cdot \hat{\imath}_{asc} = d_H \sin \vartheta_{asc} + d_V \cos \vartheta_{asc} \\ d_{desc} = \boldsymbol{d} \cdot \hat{\imath}_{desc} = -d_H \sin \vartheta_{desc} + d_V \cos \vartheta_{desc} \end{cases} \tag{5.37}$$

which can be equivalently expressed through the following matrix representation

$$\begin{bmatrix} d_{asc} \\ d_{desc} \end{bmatrix} = \begin{bmatrix} \sin \vartheta_{asc} & \cos \vartheta_{asc} \\ -\sin \vartheta_{desc} & \cos \vartheta_{desc} \end{bmatrix} \begin{bmatrix} d_H \\ d_V \end{bmatrix} \tag{5.38}$$

and easily solved with respect to the two deformation components relative to the vertical direction d_V and the horizontal one d_H. At this aim, it has been created a proper routine in IDL language applied as post-processing after it has been performed the whole DInSAR processing chain for each available geometries.

Activity Report

In this section some information about the developed activity is provided. With regard to the total amount of the processed data, Tab. 5.5 summarizes it for each target site and for each track used, specifying among input data (that are the S1 Interferometric Wide SLC data), intermediate products (coregistered data, interferograms pairs, coherence maps, and so on) and final products (the displacements 3D matrix and the outputs of the processing chain described in Fig. 5.9).

[GB]	**Fiumicino ascending**	**Fiumicino descending**	**Brumadinho descending**	**Total**
Input data	1480	912	864	3256
Intermediate data	6368	1980	1418	9766
Output data	2.7	1.5	1.5	5.7
Total	7850.7	2893.5	2283.5	13027.7

Table 5.5. Table of processed data volume for this activity.

Whereas, the processing time of each intermediate steps of the chain in Fig. 5.9 is described in Tab. 5.6. Due to the own characteristics of the adopted tools, it is more suitable define the times relative to the first part of the workflow (SNAP-part) referring to a single coregistered pair and to the three main parts (a,b,c) in Fig. 5.11; while, for the second part (IDL monitoring tool and post-processing) the measurements refer to the processing of all the interferograms and coherence maps previously generated. It is worthwhile to remark that: (i) the two main parts of the entire work-chain are performed on two different machine with different specifi-

[min]	Fiumicino ascending	Fiumicino descending	Brumadinho descending
part (a)	4.5	4.5	4.5
part (b)	5.0	5.0	7.0
part (c)	0.6	0.6	0.6
IDL Tool	7.0	5.0	5.0
Post-processing	0.8	0.5	0.5

Table 5.6. Table of actual processing times.

cations, as previously reported; (ii) the setting parameters used to process data are the same for each target site. Therefore, the processing time difference between same steps on the selected target areas, only depends on the different subsetting operations. In fact, because of the Fiumicino Airport is well visible from the S1 intensity image, it has been possible to define a proper subset in order both to decrease the dimension of the data to be processed benefiting the processing time and to have any information loss about the *reference area*. On the opposite, it has not been possible to do the same for the Brumadinho Dam zone. So, a larger subset has been performed in this last case. The overall processing to generate the interferogram pairs took about 48 and 138 hours for Fiumicino Airport area (in descending and ascending tracks, respectively) and 38 hours for Brumadinho Dam area.

Results

Now we move to show some results obtained by the application of the technique discussed before on S1 dataset covering the AOI of Fiumicino Airport. In Fig. 5.14 the average LOS deformation rates for both ascending and descending tracks is shown. Positive values indicate motion towards the sensor (so-called *uplift*, in blue), whereas negative values indicate motion away from the sensor (*subsidence*, in red). In particular, in the figures it is shown the map of displacement rates where the coherence values are more or equal then 0.4. The choice of that value allow us to exclude most of the areas that are not of interest for this analysis (like rural areas, wood areas and so forth). In this way, we can show deformation information over man-made infrastructures, buildings, bridges, roads, and so on.

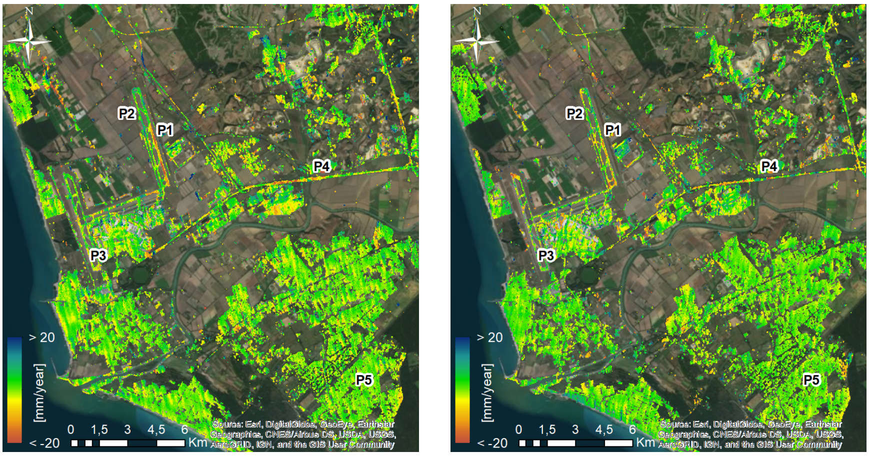

(a) (b)

Figure 5.14. Sentinel-1 average LOS deformation rate maps of the Fiumicino area over the period October 2014 - February 2019 for ascending (a) and descending (b) tracks.

The *reference area* for both the acquisition geometries is located in the right-down corner of the image where there is a residential zone, with man-made structures (like buildings, schools, houses and so forth). It has been chosen based on its features that well fit the definition of *reference area* and on other studies in literature [71, 72]. Moreover, ground deformation measurements time series on five target points are shown from Fig. 5.15 to Fig.5.19. These points are the same for both the geometry in order to highlight the differences and/or matching between them.

As a general comment, DInSAR analysis has shown the presence of slightly

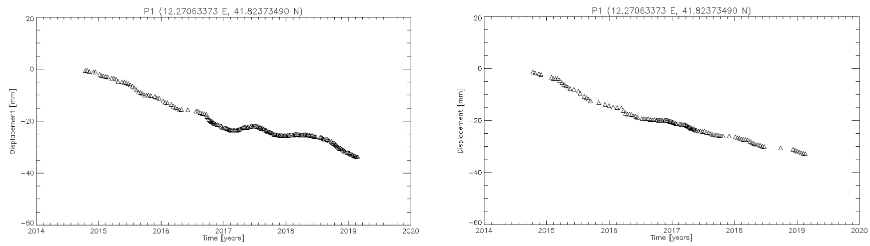

(a) (b)

Figure 5.15. S1 ground deformation measurements time series of the Fiumicino area point P1 over the period October 2014 - February 2019 for the point P1 of the ascending (a) and descending (b) tracks.

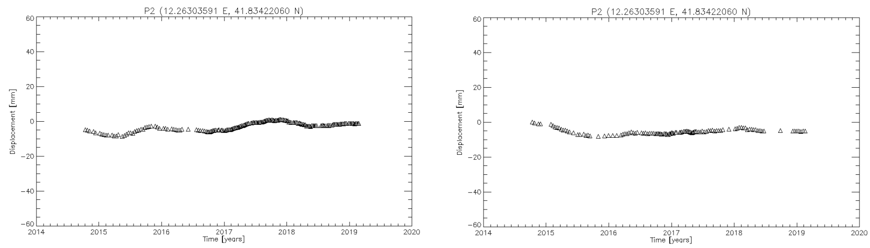

(a) (b)

Figure 5.16. S1 ground deformation measurements time series of the Fiumicino area point P2 over the period October 2014 - February 2019 for the point P2 of the ascending (a) and descending (b) tracks.

subsidence phenomena around the delta of the Tevere river (more evident close to the coastal area of the Ostia municipality). However, among the most relevant subsidence areas we can observe that ones located:

a. in the middle-southern part of the Fiumicino airport runway n.3 and n.4 (point P1), where a displacement rate of about 9 mm/year has been recorded

b. at the intersection point (P3) between the runway n.2 and the buildings of the airport, with a displacement rate of about 5 mm/year

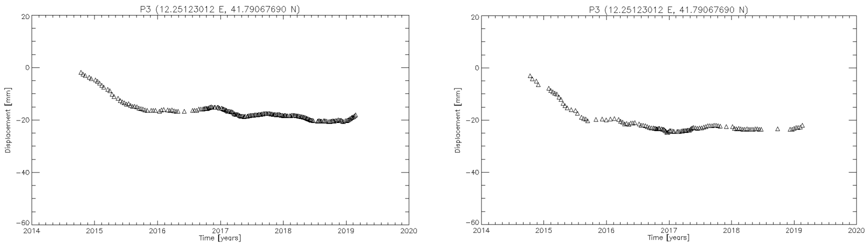

(a) (b)

Figure 5.17. S1 ground deformation measurements time series of the Fiumicino area point P3 over the period October 2014 - February 2019 for the point P3 of the ascending (a) and descending (b) tracks.

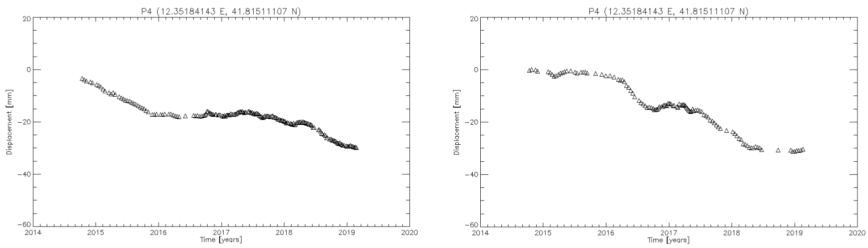

(a) (b)

Figure 5.18. S1 ground deformation measurements time series of the Fiumicino area point P4 over the period October 2014 - February 2019 for the point P4 of the ascending (a) and descending (b) tracks.

c. in some diffused points along the highway A91 with a displacement rate of more than 7 mm/year. In particular, we have selected the point P4 very close to that one shown in [73] where an analysis similar to this one has been conducted. From a visual inspection, it is possible to verify the effectiveness of the implemented method since the displacements evolution in time is very comparable in both the work.

After the decomposition of the ascending and descending LOS measurements, we have obtained the vertical and the horizontal deformation

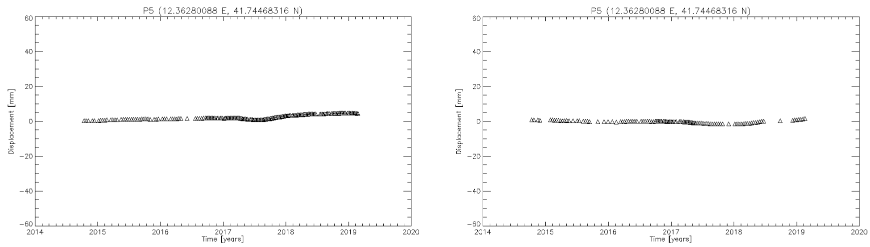

(a) (b)

Figure 5.19. S1 ground deformation measurements time series of the Fiumicino area point P5 over the period October 2014 - February 2019 for the point P4 of the ascending (a) and descending (b) tracks.

rates map shown in Fig. 5.20. As for the previous maps, also here we present the maps masking out that pixels where the coherence is less than 0.4. In this case, considerations similar to that previous ones can be made.

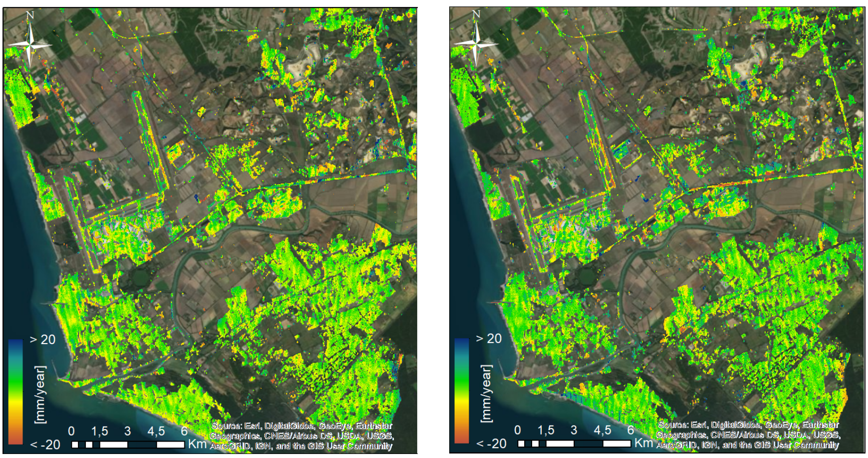

(a) (b)

Figure 5.20. S1 vertical (a) and horizontal (b) deformation rates of the Fiumicino area over the period October 2014 - February 2019.

Now we can show the results obtained for the second target site under investigation (the Brumadinho Dam). We recall that only the descending geometry is available in this case: the relative LOS deformation rate map (masking out the pixels where the coherence values is less then 0.4) is shown in Fig. 5.21. As we can see, important subsidence phenomena

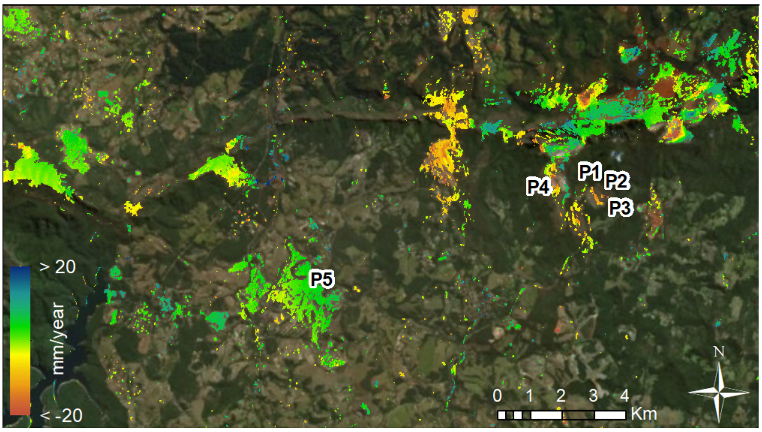

Figure 5.21. S1 average LOS deformation rate maps of the Brumadinho area over the period May 2015 - January 2019 for descending track.

are visible in the upper-right corner of the image, where several dams, including that one collapsed on the 25th January 2019, are located. For this reason, in order to verify its stability, we have selected the points P1 (at the top of the dam), P2 (at the center) and P3 (at the bottom) along it and the displacements time series are shown in Fig. 5.22-(a)-(b)-(c), respectively. For these points a displacements rate of more than 40 mm/year has been recorded. Similar considerations can be done for the point P4 in Fig. 5.22-(d). The choice of it lies on the fact that dams similar to the collapsed one are located in this place. Also in this case the degree of danger of the structures is remarkable. The point P5 in Fig. 5.22-(e) is located in the middle part of the selected *reference area*, that is the center of the Brumadinho country. Eventually, because of both acquisition geometries are not available for this study target, the vertical and horizontal components have not been calculated.

5.3 Subpixel Offset Tracking Technique

Today, a new class of methods can provide information complementary to that derived from DInSAR by working with the amplitude channel. These techniques, based on Sub-Pixel Offset Tracking (SPOT) [74, 75], allow the measurement of displacements in the South–North and East–West directions without any limitation on the observable rate. This means that

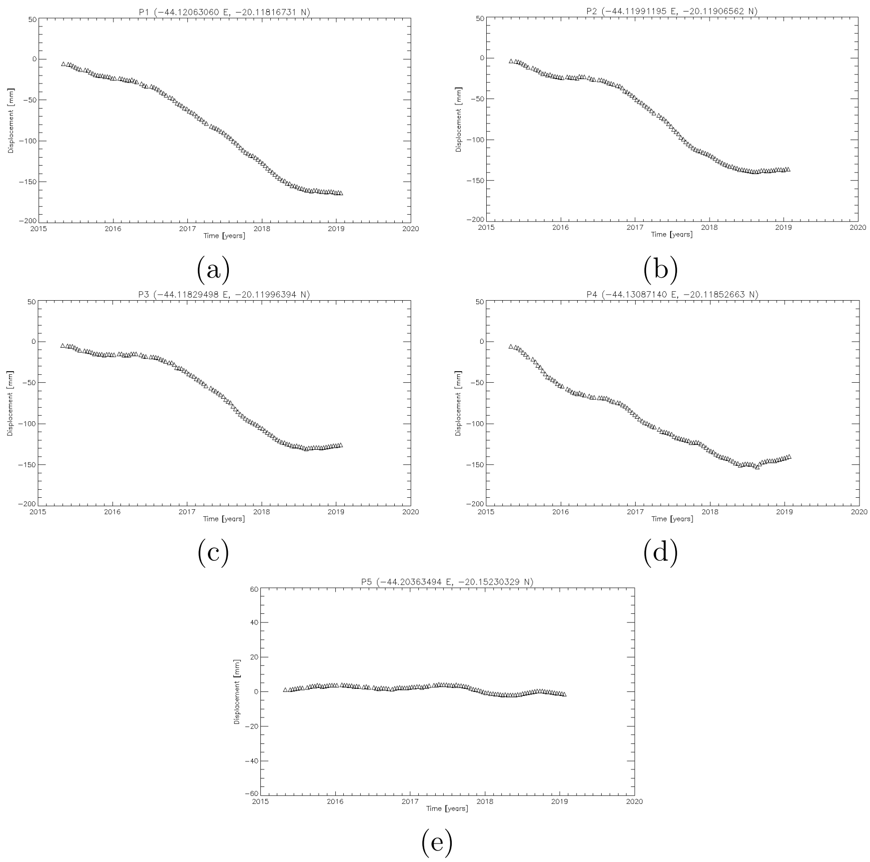

Figure 5.22. S1 ground deformation measurements time series over the period May 2015 - January 2019 for the points P1 (a), P2 (b), P3 (c), P4 (d) and P5 (e) of the Brumadinho area.

a pair of SAR images can be used to detect movements of several meters with a good degree of approximation [75]. SPOT methods are generally less precise than conventional DInSAR methods [74], however they are less sensitive to atmospheric effects and are not strictly only applicable to highly coherent targets, i.e., they can measure displacements even in densely vegetated areas [76].

5.3.1 Application on Slumgullion Landslide by Using Cosmo-SkyMed Data

SPOT methods have been well applied in movements estimation of glaciers and terrain [77–79] due to natural phenomena (for example, landslides) [74, 75] and/or human activities (subsidence induced by underground excavation) [80, 81]. In this section, the suitability of the SPOT methodology for the monitoring of the Slumgullion landslide (Colorado, US) is explored [82]. This landslide has been broadly studied in the past using field sensors due to the fast/slow related displacements [83–86]. From the beginning of 2000, SAR airborne remote sensing was also applied [87–90]. The use of satellite technologies in the literature was limited. In fact, kinematic characterization at landslide scale is today still rare, especially for long periods, due to the difficulty in implementing demanding ground surveys with adequate spatio-temporal coverage [85].

For these reasons, SAR SPOT was applied to three X-band COSMO-SkyMed spotlight images with about 1 m spatial resolution to monitor the Slumgullion landslide over a time frame of two years (from August 2011 to August 2013). In particular, they were combined in two coregistered pairs, the first covering the period August 2011–August 2012 and the second covering the period August 2012–August 2013. A third pair, covering the time frame August 2011–August 2013, was also considered to implement a consistency check of the obtained results.

Moreover, the landslide has been analyzed at both large and small scale, and the displacements retrieved are validated against ground data provided in the past literature.

Study area: Slumgullion landslide

The study area is the Slumgullion landslide (US), depicted in Fig. 5.23, with a LIDAR DEM with a 0.5 m spatial resolution superimposed and developed by the US National Center for Airborne Laser Mapping (NCALM).

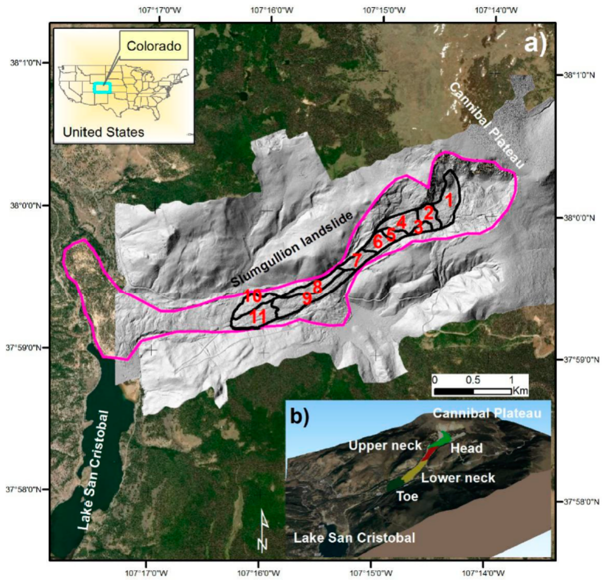

Figure 5.23. The Slumgullion landslide within the purple line. In box (a), the LIDAR DEM by NCALM superimposed onto the Google Earth view of the landslide.

In more details, the landslide is located in the San Juan Mountains (southwestern Colorado). It has been moving for about 350 years, with the maximum measured velocity of 6 m per year [84].It extends for about 7 km from the Cannibal Plateau to Lake San Cristobal, with a mean width and depth of 300 m and 14 m, respectively [83].

Inside the landslide, an area of about 1 km^2 (see black curve in Fig. 5.23) is still active. It presents a low ground-surface inclination (about 8 *degrees*). Based on its average displacement rate of 0.1–2.0 cm/day [91], it can be considered a very slow landslide according to [92].

The Slumgullion landslide is constituted of multiple kinematic elements, each of them moving like a rigid block sliding along faults [93, 94]. Therefore, the landslide has been divided into 11 primary temporally consistent kinematic elements (see labels in Fig. 5.23) [85]. As indicated in [95], these regions can be assembled into head (from Region 1 to 4), upper neck (from Region 5 to 7), lower neck (Region 8 and 9), and toe (Region 10 and 11), as we can see in box (b) of the Fig. 5.23).

Between 1985 and 1990, velocity of elements from 1 to 4 (the flattest part of the landslide) increased nearly linearly in the downslope direction [80, 83, 84]. Displacement rate increased from element 4 to 5 and increased almost linearly up to element 7, that is the fastest and steepest element of the landslide. Then, it widens and flattens, slowing downslope to elements 8 and 9. Finally, the landslide moved along the oldest ground surface forming elements 10 and 11, whose speed was much slower than that of elements 8 and 9.

Methodology

In Fig. 5.24 the block diagram of the implemented methodology is showed: in the upper part, the general processing chain (from the data input to the final results) is reported; in the lower part, an exploded view of the SPOT processing block is depicted.

Processing starts from standard coregistration [8]. If precise orbit data are available, an only orbit-based coregistration can be implemented. Otherwise, full coregistration (i.e., including cross-correlation and coherence refinement steps) is suggested, provided that the scene is much larger than the AOI. In this case, Ground Control Points (GCPs) located on the land-

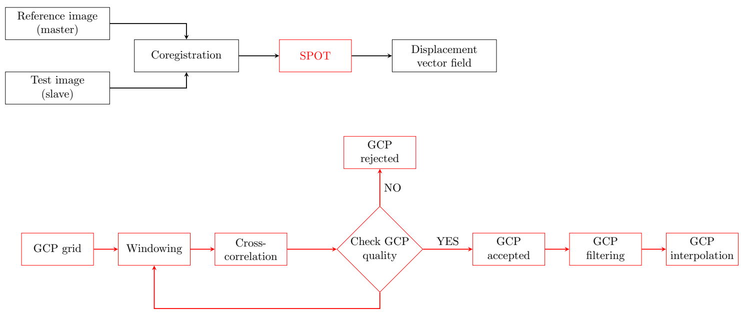

Figure 5.24. Flowchart of the implemented methodology.

slide will be automatically discarded because they usually exhibit very low cross-correlation and interferometric coherence values. The first acquired image is assumed to be the master image (the reference for the estimation of displacements). Hence, the displacements are evaluated in the slave image. The SPOT algorithm implements cross-correlation measures on several windows extracted from coregistered image pair in order to estimate the shift between the master patch and the slave patch. These windows are extracted around grid points quite regularly distributed across the images (see first two blocks of the lower diagram in Fig. 5.24). The cross-correlation between two null-mean patches $\boldsymbol{M}$ and $\boldsymbol{S}$, taken on the master and slave image, respectively, is computed as follows:

$$\boldsymbol{C} = \frac{\mathbb{F}^{-1}\left[\mathbb{F}[\boldsymbol{M}] \times \mathbb{F}[\boldsymbol{S}]^*\right]}{\sqrt{\langle \boldsymbol{M}^2 \rangle \times \langle \boldsymbol{S}^2 \rangle}}, \qquad C_{ij} \in [0, 1] \tag{5.39}$$

where the FT (inverse FT) is implemented via the FFT (inverse FFT) algorithm and the symbol $\langle \cdot \rangle$ represents the mean operator. In (5.39), $\boldsymbol{M}$ and $\boldsymbol{S}$ are oversampled by a factor f (which must be a power of two in order to optimize the FFT performance) to account for the sub-pixel movements, being the minimum detectable displacement (in pixel units) equal to $1/f$. We notice that $\boldsymbol{C}$ is a matrix. Its maximum identifies the amount of shift to be applied to the slave patch to have it superimposed onto the master patch. The higher (and sharper) the peak identifying the matrix maximum, the more reliable is the estimated shift. Specifically, because of $\boldsymbol{C}$ is a circular matrix, the maximum detectable shift is equal to $d/2$, being d the patch dimension (usually square).

In order to identify reliable shifts, two quality parameters are considered: the peak value c_{max} of the cross-correlation matrix and the ratio $q = c_{max}/\langle C \rangle$. For both of them, a pre-determined user-defined threshold is used to exclude invalid GCPs.

Accepted GCPs are then filtered to minimize noisy displacement patterns. To this aim, shifts are classified based on their sign. We have generated a three-class classification map (positive shift, negative shift, and null shift). A connected component labeling algorithm [96] is used to segment this classification map. Small regions surrounded by a homogeneous background of shifts with the same sign are assumed to be noisy patterns and, therefore, are discarded. Finally, filtered GCPs are interpolated into the final displacement map.

Results

An example of the results obtained with the SPOT technique is reported in Fig. 5.25, for the time frame August 2011–August 2012. The arrows represent the direction of the estimated vector field retrieved from the North–South and East–West components. According to the past literature, the highest velocity values have been recorded in the central part of the landslide (upper and lower necks). The result for the time frame August 2012–August 2013 is very similar to the one of the time frame August 2011–August 2012. In both the cases, the size of the correlation window has been set to 64 pixels, the cross-correlation threshold to 0.1, the threshold on the ratio q to 4, and the oversampling factor f to 4. This means that the minimum retrievable displacement is on the order of 17 cm

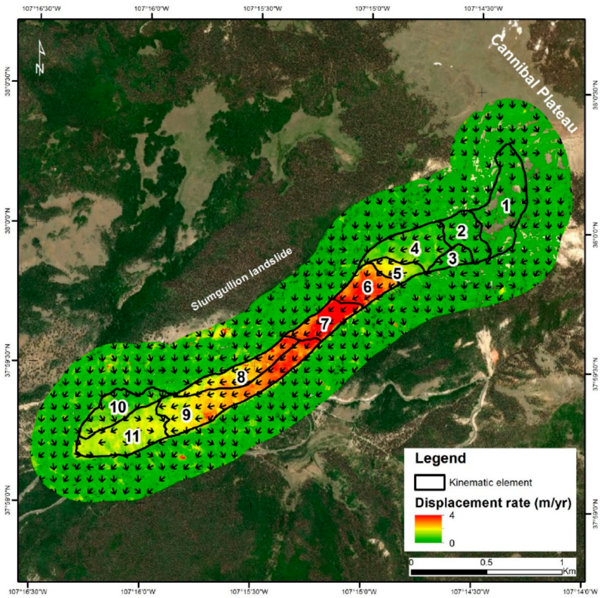

Figure 5.25. Slumgullion landslide displacement rate in $m/year$ for the time frame August 2011-August 2012. The arrows represent the direction of the estimated vector field.

and 10 cm in the azimuth and range direction, respectively. In Tab. 5.7, the parameters set to run the experiments are summarized. The third one (Run 3) regards a consistency check of the retrieved displacements fields.

In Fig. 5.26, the maps of quality parameters relative to the pair August 2011–August 2012 are shown: the c_{max} map in Fig. 5.26-(a) and the q map Fig. 5.26-(b). The noisy displacement patterns depicted in Fig. 5.25 correspond to areas with a low value of the considered quality parameters for the GCPs selection.

In Tab. 5.8, quantitative data about the estimated displacements rate, for a window dimension of 64 pixels, are reported. These values have been obtained by averaging the estimated velocities in the kinematic regions indicated in [85]. Although two different window dimensions (64 and 128

	Run 1	**Run 2**	**Run 3**
Parameter	Value	Value	Value
Master image	2011/08/03	2012/08/06	2011/08/03
Slave image	2012/08/06	2013/08/08	2013/08/08
Time span	369 days	367 days	736 days
Pixel spacing azimuth	0.70 m	0.70 m	0.70 m
Pixel spacing range	0.38 m	0.38 m	0.38 m
x-grid spacing	10 pixels	10 pixels	10 pixels
y-grid spacing	10 pixels	10 pixels	10 pixels
Oversampling factor (f)	4	4	4
Cross-correlation threshold	0.1	0.1	0.1
q threshold	4	4	4
Max displacement	8 m	8 m	16 m
Computational time	$\approx$ 45 min	$\approx$ 45 min	$\approx$ 45 min

Table 5.7. Summary of the SPOT parameters used in this work.

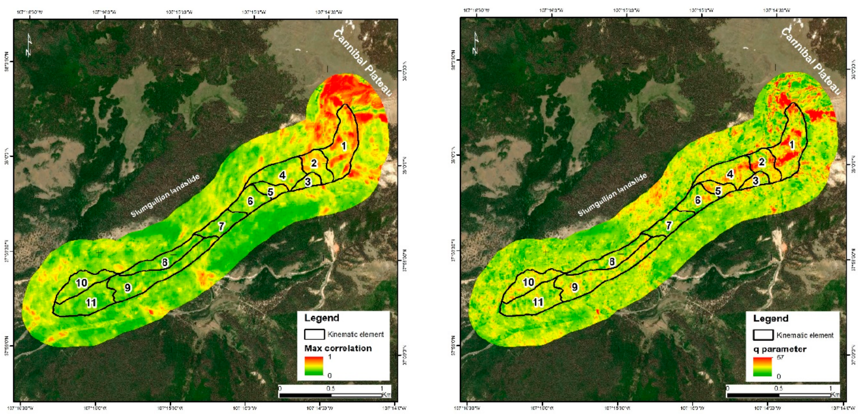

(a) (b)

Figure 5.26. c_{max} map (a) and the q map (b) for the satellite image pair August 2011-August 2012.

pixels) have been experimented, similar results have been produced.

The last two columns in Tab. 5.8 refer to the consistency check. Let

Region ID	$\langle \boldsymbol{V} \rangle$ **2011-2012**	$\boldsymbol{\sigma_V}$ **2011-2012**	$\langle \boldsymbol{V} \rangle$ **2012-2013**	$\boldsymbol{\sigma_V}$ **2012-2013**	$\boldsymbol{\lvert CC \rvert}$	$\boldsymbol{\sigma_{CC}}$
			$w = 64$			
Landslide	1.03	0.79	0.81	0.72	0.01	0.42
1	0.11	0.09	0.13	0.08	0.07	0.14
2	0.26	0.13	0.16	0.09	0.00	0.15
3	0.33	0.13	0.24	0.10	0.03	0.19
4	0.54	0.18	0.38	0.16	0.08	0.19
5	1.11	0.29	0.91	0.29	0.12	0.23
6	2.00	0.49	1.80	0.42	0.09	0.63
7	2.40	0.67	2.14	0.55	0.07	0.89
8	1.56	0.47	1.24	0.45	0.05	0.50
9	1.63	0.47	1.34	0.59	0.09	0.52
10	0.58	0.23	0.36	0.16	0.09	0.30
11	1.00	0.17	0.52	0.18	0.05	0.26

Table 5.8. Summary of the obtained results expressed in meters per year, for a window size of 64 pixels: V is the displacement velocity; CC represents the consistency check.

us call A the result for the period 2011–2012, B the one for the period 2012–2013, and C the one for the period 2011–2013. So, reliable results should return $A + B - C = 0$. As we can see in table, this is not strictly achieved. Anyway, the deviation from zero of the aforementioned equation is generally small. In particular, the distribution of the consistency check is Gaussian with a mean of about 1 $cm/year$ and standard deviation of 42 $cm/year$ in the 64-pixel window case. In the 128-pixel window case, the mean and standard deviation of the distribution are on the order of 2 $cm/year$ and 42 $cm/year$, respectively.

Let us now move to validate the obtained results, both at landslide and point scale. Recently, some papers using remote sensing data have been presented [88–91, 95]. But only in [91] the use of space-borne SAR data has been made. However, this work was focused on spotlight DIn-

SAR methods covering one year of observations, with small insights in long-term displacement monitoring and limited validation of the presented results against literature data. All other works are based on airborne data acquired by the NASA/JPL L-band UAVSAR with 0.6 m and 1.9 m spatial resolution in the azimuth and slant range directions, respectively [97]. A perfectly consistent validation set (i.e, ground measurements acquired over the same time span covering by the SAR images used in this study) is not available, especially concerning the landslide scale. The most referenced data are relevant to the period 1985–1990 and to the year 2010 (see Tab. 5.9).

Region ID	$\langle V_f \rangle$ **1985-1990**	σ_{V_f} **1985-1990**	$\langle V_{GB} \rangle$ **2010**	$\sigma_{V_{GB}}$ **2010**
Landslide	2.48	1.38	1.16	1.35
1	0.73	0.40	0.14	0.91
2	1.20	0.25	0.32	1.27
3	1.42	0.14	0.36	1.31
4	1.60	0.51	0.36	0.98
5	2.44	0.29	1.05	1.53
6	3.86	0.87	1.67	2.51
7	5.25	0.73	2.84	3.35
8	3.57	0.40	1.64	3.13
9	3.65	0.87	1.93	3.06
10	1.56	0.18	0.91	6.49
11	1.97	0.36	1.13	2.37

Table 5.9. Available literature data expressed in meters per year.

Data of the period 1985–1990 were produced in [93, 94] using photogrammetry and field surveys. Data referring to the year 2010 were collected in [85] through Ground-Based SAR Interferometry (GBInSAR) measurements. The latter study highlighted that, by 2010, the landslide's velocity halved compared to its values in the 1985–1990 period, and that the landslide head was affected by the largest decrease in velocity. The authors ascribed this behavior to both geomorphological and climatic factors. The displacement rates obtained in this study are consistent with those reported in Tab. 5.9 for the GBInSAR survey implemented in 2010 [85]. The direction of the estimated vector field (see arrows in Fig. 5.25) mainly follows the landslide slope profile and it is similar to the one presented in the past literature [95].

The presented results have shown that the estimated displacements are practically independent from the variation of the correlation window, being for all the regions below the theoretical sensitivity of the method, which is given by $1/f$. On the other hand, if we use a smaller correlation window (for example, 32 pixels) the frequency-domain cross-correlation is less reliable, and this increases the standard deviation of the estimated displacement field, which results in noisiness and physical inconsistency. Therefore, it is suggested to operate with the 64-pixel window in order to have both a lower computational time compared to the 128-pixel window (for these experiments, the computational time was about 2.1 hours per run, compared to about 45 minutes for each 64-pixel window run) and a higher level of detail with a better preservation of the landslide edges. In fact, for the 64-pixel window, the registered values in Tab. 5.8 of the standard deviation range from 0.08 $m/year$ in Region 1 (pair 2012–2013) to 0.67 $m/year$ in Region 7 (pair 2011–2012). These values are similar to those indicated in [93, 94].

It is worthwhile to notice that the noisier displacement patterns (see as an example the north of landslide Region 8) present very low values of the used quality parameters. This means that the peak of the correlation matrix c_{max} is not well-defined compared with the background, thus leading to an unreliable estimate of the displacements. In the landslide area, even though the peak of the correlation matrix is not very pronounced (as expected, based on the characteristics of the phenomenon under investigation), its ratio with respect to the mean (q) is quite high.

As stated above, the resulting distribution of the consistency check has a mean very close to zero either at landslide scale or within the 11 kinematic regions. As we can appreciate in Tab. 5.9, the registered deviations from zero range (in absolute value) from less than 1 $cm/year$ (Region 2) to 12 $cm/year$ (Region 5). Similar results have been obtained using the 128-pixel window dimension.

Now, we can move to discuss about the obtained results at a finer scale exploiting data concerning 19 Measurement Points (MPs) installed on the landslide by the US Geological Survey (USGS) [98]. Reference data for comparison have been extracted from [89], in which the kinematics of the landslide was analyzed in the time frame August 2011–April 2012 using airborne L-band remote sensing and was compared with GPS data collected at the USGS MPs. [1]

The comparison between the results of this study and those from [89] is shown in Fig. 5.27. The position of the MPs with respect to one of the available SAR acquisitions is also reported (note that MP1 and MP2 are not shown in this graphic since their position falls outside the image cut considered). Airborne SAR-derived data are displayed with blue bars and GPS data with gray bars. The results of this study (orange bars) have been obtained by taking the maximum displacement in a window of 100 $\times$ 100 meters around each MP, allowing us to compensate geocoding errors (some of the MPs are at the landslide borders and/or at the transition between different kinematic zones) and SPOT maps inhomogeneity/noise.

In general, the three datasets qualitatively present a good agreement. Disagreements are grouped, as expected, in the neck area, where the landslide is faster. In this sector, the presented results exhibit the highest inconsistency with respect to the airborne SAR and GPS data. Indeed,

[1] These data were reproduced through graph digitalization, and it is therefore possible that they show (negligible) differences with respect to their original version.

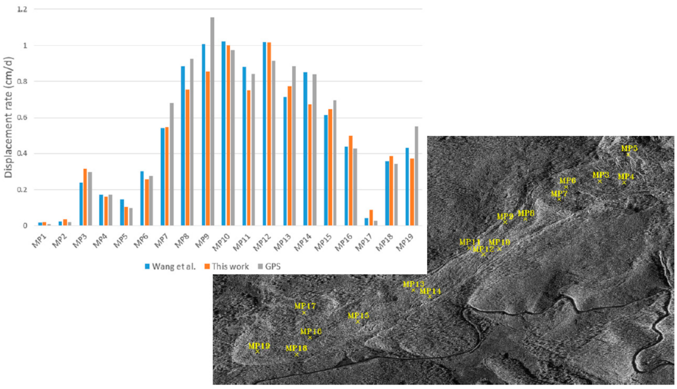

Figure 5.27. Comparison between space-borne COSMO-SkyMed displacement rates (orange), airborne UAVSAR displacement rates (blue) and GPS displacement rates (gray), for the 19 USGS MPs.

for the MP8, MP9, and MP14 points, the landslide displacement rate is underestimated when compared to GPS data of about 0.17 cm/day, 0.3 cm/day, and 0.16 cm/day, respectively. When the results are compared to the measurements extracted from airborne SAR images, the underestimation for that points is on the order of 0.13 cm/day, 0.15 cm/day, and 0.17 cm/day, respectively.

Eventually, assuming that points MP1 to MP7 belong to the head, that MP8 to MP14 belong to the neck, and that MP15 to MP19 belong to the toe, the registered RMSE of the displacement rates here estimated with respect to GPS measurements is about 0.05 cm/day for the head, 0.15 cm/day for the neck, and 0.09 cm/day for the toe.

This page intentionally left blank.

Chapter 6

Conclusions

The main research results concerning the SAR remote sensing techniques and applications, and achieved within the Ph.D. degree course, have been presented and discussed in this thesis.

First of all, a unified analytical formulation of the SAR raw signals of extended scenes, expressed both in space and in frequency domains and valid for all the operating modes, has been proposed. Based on this formulation, a simulation algorithm has been presented that allows to simulate SAR raw signals of extended scenes acquired with any acquisition mode, including the effects of trajectory deviations. It has been shown that this method is more accurate (since it makes less restrictive assumptions) and/or efficient than the available simulators for all acquisition modes, except for the cases in which a full 2D Fourier-domain approach is possible (i.e., stripmap, scanSAR, and spotlight cases without trajectory deviations with respect to the ideal straightline trajectory). In all other cases (i.e., sliding spotlight and TOPSAR modes with or without trajectory deviations, and stripmap, scanSAR, and spotlight cases with trajectory deviations), the proposed simulator is more accurate and/or efficient than existing ones. The proposed method is based on a 1D range

Fourier-domain processing, followed by a 1D azimuth time-domain integration. Computational complexity of the proposed simulation algorithm has been also evaluated, thus showing the bigger advantage with respect to the time-domain approach in terms of computing time. Eventually, accuracy of the proposed simulation scheme has been assessed by comparing the raw signals that it generates with those generated by using the exact time-domain approach. Simulations of SAR signals relative to extended, both canonical and realistic, scenes have been also provided.

The second presented research topic referred to a preliminary study of the potential subsidence phenomena affecting two selected target sites, using the SAR interferometry technique. The presented results have confirmed that the implemented DInSAR procedure provide displacement measurements in good agreement with those available in literature. The choice to generate a number of interferograms greater than the number of acquisitions (by means moving through a SBAS approach) has allowed us to filter out the errors typically involved in the interferometric procedure, to compensate for the possible temporal decorrelation effect and, finally, to partially mitigate the atmospheric artifacts. However, this choice has not paid in terms of a complete automation of the processing. Even though some drawbacks have been faced, the presented results are a promising indication for the future realization of a monitoring service based on the adopted methodology.

Eventually, the third research activity concerned the suitability of spaceborne SAR observations for fast landslides monitoring. Therefore, subpixel offset tracking methodology has been evaluated and applied to fast landslides such as the Slumgullion landslide (Colorado, US), using pairs of SAR images acquired with about one-year temporal baseline in spotlight mode with sub-meter resolution by the COSMO-SkyMed satellite. These data have been combined in two pairs covering two years (from August 2011 to August 2013) and the obtained results have been validated by means of a consistency check and against the temporally closest available literature data, both at landslide and point scale. The results discussed in this study have been demonstrated the reliability of space-borne radar imagery in order to monitor large landslide-induced movement and its consistency with the results given by more expensive and time-demanding strategies, such as field surveys and/or airborne remote sensing.

This page intentionally left blank.

Bibliography

[1] C. Elachi and J. J. Van Zyl, *Introduction to the physics and techniques of remote sensing.* John Wiley & Sons, 2006, vol. 28.

[2] N. Landsat, *Science data users handbook*, 7.

[3] C. Elachi, "Spaceborne radar remote sensing: Applications and techniques," *New York, IEEE Press, 1988, 285 p.*, 1988.

[4] C. A. Wiley, *Pulsed doppler radar methods and apparatus*, US Patent 3,196,436, Jul. 1965.

[5] C. Elachi, "Radar images of the earth from space," *Scientific American*, vol. 247, no. 6, pp. 54–61, 1982.

[6] L. E. Roth and S. D. Wall, "The face of venus. the magellan radar-mapping mission.," in *The Face of Venus. The Magellan Radar-Mapping Mission*, 1995.

[7] E. Sentinel, *Sar user guide introduction. 2016*, 1.

[8] G. Franceschetti and R. Lanari, *Synthetic aperture radar processing.* New York, NY, USA: CRC press, 1999.

[9] J. C. Curlander and R. N. McDonough, *Synthetic aperture radar: systems and signal processing.* 1991.

[10] G. Franceschetti, *Electromagnetics: theory, techniques, and engineering paradigms.* Springer Science & Business Media, 2013.

[11] G. Franceschetti and G. Schirinzi, “A sar processor based on two-dimensional fft codes,” *IEEE Transactions on Aerospace and Electronic Systems*, vol. 26, no. 2, pp. 356–366, 1990.

[12] W. Chialin, K. Liu, and M. Jin, “Modeling and a correlation algorithm for spaceborne sar signals,” *IEEE Transactions on Aerospace and Electronic Systems*, vol. 18, no. 5, pp. 563–575, 1982.

[13] R. Raney, “A comment on doppler fm rate,” *International Journal of Remote Sensing*, vol. 8, no. 7, pp. 1091–1092, 1987.

[14] C. Chang, M. Jin, and J. Curlander, “Squint mode sar processing algorithms,” in *Proc. IGARSS*, vol. 89, 1989, pp. 1702–1706.

[15] A. Moreira and Y. Huang, “Airborne sar processing of highly squinted data using a chirp scaling approach with integrated motion compensation,” *IEEE Transactions on Geoscience and Remote Sensing*, vol. 32, no. 5, pp. 1029–1040, 1994.

[16] G. Franceschetti, R. Lanari, and E.-S. Marzouk, “A new two-dimensional squint mode sar processor,” *IEEE transactions on aerospace and electronic systems*, vol. 32, no. 2, pp. 854–863, 1996.

[17] J. Way and E. A. Smith, “The evolution of synthetic aperture radar systems and their progression to the eos sar,” *IEEE transactions on geoscience and remote sensing*, vol. 29, no. 6, pp. 962–985, 1991.

[18] H. Runge, “Benefits of antenna yaw steering for sar,” in *IGARSS'91; Proceedings of the 11th Annual International Geoscience and Remote Sensing Symposium*, vol. 1, 1991, pp. 257–261.

[19] G. W. Davidson and I. Cumming, “Signal properties of spaceborne squint-mode sar,” *IEEE Transactions on Geoscience and Remote Sensing*, vol. 35, no. 3, pp. 611–617, 1997.

[20] J. C. Kirk, “Motion compensation for synthetic aperture radar,” *IEEE Transactions on Aerospace and Electronic Systems*, no. 3, 1975.

[21] M. Y. Jin and C. Wu, "A sar correlation algorithm which accommodates large-range migration," *IEEE Transactions on Geoscience and Remote Sensing*, no. 6, pp. 592–597, 1984.

[22] G. Franceschetti, R. Lanari, V. Pascazio, and G. Schirinzi, "Wasar: A wide-angle sar processor," in *IEE Proceedings F-Radar and Signal Processing*, IET, vol. 139, 1992, pp. 107–114.

[23] C. Cafforio, C. Prati, and F. Rocca, "Sar data focusing using seismic migration techniques," *IEEE transactions on aerospace and electronic systems*, vol. 27, no. 2, pp. 194–207, 1991.

[24] R. H. Stolt, "Migration by fourier transform," *Geophysics*, vol. 43, no. 1, pp. 23–48, 1978.

[25] R. K. Raney, H. Runge, R. Bamler, I. G. Cumming, and F. H. Wong, "Precision sar processing using chirp scaling," *IEEE Transactions on geoscience and remote sensing*, vol. 32, no. 4, pp. 786–799, 1994.

[26] A. Papoulis, "Systems and transforms with applications in optics," *McGraw-Hill Series in System Science, Malabar: Krieger, 1968*, 1968.

[27] L. R. Rabiner, R. W. Schafer, and C. M. Rader, "The chirp z-transform algorithm and its application," *Bell System Technical Journal*, vol. 48, no. 5, pp. 1249–1292, 1969.

[28] R. Lanari and G. Fornaro, "A short discussion on the exact compensation of the sar range-dependent range cell migration effect," *IEEE Transactions on Geoscience and Remote Sensing*, vol. 35, no. 6, pp. 1446–1452, 1997.

[29] R. Bamler, "A comparison of range-doppler and wavenumber domain sar focusing algorithms," *IEEE Transactions on Geoscience and Remote Sensing*, vol. 30, no. 4, pp. 706–713, 1992.

[30] G. Franceschetti, R. Lanari, and E. Marzouk, “Efficient and high precision space-variant processing of sar data,” *IEEE transactions on aerospace and electronic systems*, vol. 31, no. 1, pp. 227–237, 1995.

[31] D. Belcher and C. Baker, “High resolution processing of hybrid strip-map/spotlight mode sar,” *IEE Proceedings-Radar, Sonar and Navigation*, vol. 143, no. 6, pp. 366–374, 1996.

[32] R. Lanari, S. Zoffoli, E. Sansosti, G. Fornaro, and F. Serafino, “New approach for hybrid strip-map/spotlight sar data focusing,” *IEE Proceedings-Radar, Sonar and Navigation*, vol. 148, no. 6, pp. 363–372, 2001.

[33] J. Mittermayer, R. Lord, and E. Borner, “Sliding spotlight sar processing for terrasar-x using a new formulation of the extended chirp scaling algorithm,” in *IGARSS 2003. 2003 IEEE International Geoscience and Remote Sensing Symposium. Proceedings (IEEE Cat. No. 03CH37477)*, IEEE, vol. 3, 2003, pp. 1462–1464.

[34] F. De Zan and A. M. Guarnieri, “Topsar: Terrain observation by progressive scans,” *IEEE Transactions on Geoscience and Remote Sensing*, vol. 44, no. 9, pp. 2352–2360, 2006.

[35] D. A. Dell’Aglio, G. Di Martino, A. Iodice, D. Riccio, and G. Ruello, “A unified formulation of sar raw signals from extended scenes for all acquisition modes with application to simulation,” *IEEE Transactions on Geoscience and Remote Sensing*, vol. 56, no. 8, pp. 4956–4967, 2018.

[36] P. Prats, R. Scheiber, J. Mittermayer, A. Meta, and A. Moreira, “Processing of sliding spotlight and tops sar data using baseband azimuth scaling,” *IEEE Transactions on geoscience and remote sensing*, vol. 48, no. 2, pp. 770–780, 2009.

[37] G. Sun, M. Xing, Y. Wang, Y. Wu, Y. Wu, and Z. Bao, "Sliding spotlight and tops sar data processing without subaperture," *IEEE Geoscience and Remote Sensing Letters*, vol. 8, no. 6, pp. 1036–1040, 2011.

[38] W. Yang, J. Chen, H. Zeng, J. Zhou, P. Wang, and C.-S. Li, "A novel three-step image formation scheme for unified focusing on spaceborne sar data," *Progress In Electromagnetics Research*, vol. 137, pp. 621–642, 2013.

[39] A. Meta, P. Prats, U. Steinbrecher, J. Mittermayer, and R. Scheiber, "Terrasar-x topsar and scansar comparison," in *7th European Conference on Synthetic Aperture Radar*, VDE, 2008, pp. 1–4.

[40] G. Franceschetti, M. Migliaccio, D. Riccio, and G. Schirinzi, "Saras: A synthetic aperture radar (sar) raw signal simulator," *IEEE Transactions on Geoscience and Remote Sensing*, vol. 30, no. 1, pp. 110–123, 1992.

[41] S. Cimmino, G. Franceschetti, A. Iodice, D. Riccio, and G. Ruello, "Efficient spotlight sar raw signal simulation of extended scenes," *IEEE Transactions on Geoscience and Remote Sensing*, vol. 41, no. 10, pp. 2329–2337, 2003.

[42] G. Franceschetti, R. Guida, A. Iodice, D. Riccio, and G. Ruello, "Efficient simulation of hybrid stripmap-spotlight sar raw signals from extended scenes," *IEEE transactions on geoscience and remote sensing*, vol. 42, no. 11, pp. 2385–2396, 2004.

[43] L. C. Graham, "Synthetic interferometer radar for topographic mapping," *Proceedings of the IEEE*, vol. 62, no. 6, pp. 763–768, 1974.

[44] A. Papoulis and S. U. Pillai, *Probability, random variables, and stochastic processes.* Tata McGraw-Hill Education, 2002.

[45] F. Gatelli, A. M. Guamieri, F. Parizzi, P. Pasquali, C. Prati, and F. Rocca, "The wavenumber shift in sar interferometry," *IEEE Transactions on Geoscience and Remote Sensing*, vol. 32, no. 4, pp. 855–865, 1994.

[46] H. A. Zebker and J. Villasenor, "Decorrelation in interferometric radar echoes," *IEEE Transactions on geoscience and remote sensing*, vol. 30, no. 5, pp. 950–959, 1992.

[47] R. Lanari, G. Fornaro, D. Riccio, M. Migliaccio, K. P. Papathanassiou, J. R. Moreira, M. Schwabisch, L. Dutra, G. Puglisi, G. Franceschetti, *et al.*, "Generation of digital elevation models by using sir-c/x-sar multifrequency two-pass interferometry: The etna case study," *IEEE Transactions on Geoscience and Remote Sensing*, no. 5, pp. 1097–1114, 1996.

[48] D. Massonnet, M. Rossi, C. Carmona, F. Adragna, G. Peltzer, K. Feigl, and T. Rabaute, "The displacement field of the landers earthquake mapped by radar interferometry," *Nature*, vol. 364, no. 6433, p. 138, 1993.

[49] G. Peltzer and P. Rosen, "Surface displacement of the 17 may 1993 eureka valley, california, earthquake observed by sar interferometry," *Science*, vol. 268, no. 5215, pp. 1333–1336, 1995.

[50] R. M. Goldstein, H. Engelhardt, B. Kamb, and R. M. Frolich, "Satellite radar interferometry for monitoring ice sheet motion: Application to an antarctic ice stream," *Science*, vol. 262, no. 5139, pp. 1525–1530, 1993.

[51] D. Massonnet, P. Briole, and A. Arnaud, "Deflation of mount etna monitored by spaceborne radar interferometry," *Nature*, vol. 375, no. 6532, p. 567, 1995.

[52] R. Lanari, P. Lundgren, and E. Sansosti, “Dynamic deformation of etna volcano observed by satellite radar interferometry,” *Geophysical Research Letters*, vol. 25, no. 10, pp. 1541–1544, 1998.

[53] M. Costantini and P. A. Rosen, “A generalized phase unwrapping approach for sparse data,” in *IEEE 1999 International Geoscience and Remote Sensing Symposium. IGARSS'99 (Cat. No. 99CH36293)*, IEEE, vol. 1, 1999, pp. 267–269.

[54] A. Ferretti, C. Prati, and F. Rocca, “Permanent scatterers in sar interferometry,” *IEEE Transactions on geoscience and remote sensing*, vol. 39, no. 1, pp. 8–20, 2001.

[55] C. Colesanti, A. Ferretti, F. Novali, C. Prati, and F. Rocca, “Sar monitoring of progressive and seasonal ground deformation using the permanent scatterers technique,” *IEEE Transactions on Geoscience and Remote Sensing*, vol. 41, no. 7, pp. 1685–1701, 2003.

[56] M. Costantini, A. Iodice, L. Magnapane, and L. Pietranera, “Monitoring terrain movements by means of sparse sar differential interferometric measurements,” in *IGARSS 2000. IEEE 2000 International Geoscience and Remote Sensing Symposium. Taking the Pulse of the Planet: The Role of Remote Sensing in Managing the Environment. Proceedings (Cat. No. 00CH37120)*, IEEE, vol. 7, 2000, pp. 3225–3227.

[57] S. Usai, E. Sansosti, P. Berardino, R. Lanari, G. Fornaro, M. Tesauro, and P. Lundgren, “Modelling terrain deformations at the phlegrean fields with insar,” in *IGARSS 2000. IEEE 2000 International Geoscience and Remote Sensing Symposium. Taking the Pulse of the Planet: The Role of Remote Sensing in Managing the Environment. Proceedings (Cat. No. 00CH37120)*, IEEE, vol. 5, 2000, pp. 2245–2247.

[58] M. Costantini, A. Iodice, and L. Pietranera, "Temporal analysis of terrain subsidence by means of sparse sar differential interferometric measurements," in *SAR Image Analysis, Modeling, and Techniques III*, International Society for Optics and Photonics, vol. 4173, 2000, pp. 251–258.

[59] P. Berardino, G. Fornaro, R. Lanari, and E. Sansosti, "A new algorithm for surface deformation monitoring based on small baseline differential sar interferograms," *IEEE transactions on geoscience and remote sensing*, vol. 40, no. 11, pp. 2375–2383, 2002.

[60] R. Lanari, O. Mora, M. Manunta, J. J. Mallorquı, P. Berardino, and E. Sansosti, "A small-baseline approach for investigating deformations on full-resolution differential sar interferograms," *IEEE Transactions on Geoscience and Remote Sensing*, vol. 42, no. 7, pp. 1377–1386, 2004.

[61] G. H. Golub and C. Reinsch, "Singular value decomposition and least squares solutions," in *Linear Algebra*, Springer, 1971, pp. 134–151.

[62] V. Klema and A. Laub, "The singular value decomposition: Its computation and some applications," *IEEE Transactions on automatic control*, vol. 25, no. 2, pp. 164–176, 1980.

[63] M. Manunta, C. De Luca, I. Zinno, F. Casu, M. Manzo, M. Bonano, A. Fusco, A. Pepe, G. Onorato, P. Berardino, *et al.*, "The parallel sbas approach for sentinel-1 interferometric wide swath deformation time-series generation: Algorithm description and products quality assessment," *IEEE Transactions on Geoscience and Remote Sensing*, vol. 57, no. 9, pp. 6259–6281, 2019.

[64] C. W. Chen and H. A. Zebker, "Phase unwrapping for large sar interferograms: Statistical segmentation and generalized network models," *IEEE Transactions on Geoscience and Remote Sensing*, vol. 40, no. 8, pp. 1709–1719, 2002.

[65] R. M. Goldstein and C. L. Werner, "Radar interferogram filtering for geophysical applications," *Geophysical research letters*, vol. 25, no. 21, pp. 4035–4038, 1998.

[66] E. Sansosti, P. Berardino, M. Manunta, F. Serafino, and G. Fornaro, "Geometrical sar image registration," *IEEE Transactions on Geoscience and Remote Sensing*, vol. 44, no. 10, pp. 2861–2870, 2006.

[67] S. Fiaschi, D. Closson, N. A. Karaki, P. Pasquali, P. Riccardi, and M. Floris, "The complex karst dynamics of the lisan peninsula revealed by 25 years of dinsar observations. dead sea, jordan," *ISPRS Journal of Photogrammetry and Remote Sensing*, vol. 130, pp. 358–369, 2017.

[68] D. Massonnet and K. L. Feigl, "Radar interferometry and its application to changes in the earth's surface," *Reviews of geophysics*, vol. 36, no. 4, pp. 441–500, 1998.

[69] G. Rufino, A. Moccia, and S. Esposito, "Dem generation by means of ers tandem data," *IEEE Transactions on Geoscience and Remote Sensing*, vol. 36, no. 6, pp. 1905–1912, 1998.

[70] M. Manzo, G. Ricciardi, F. Casu, G. Ventura, G. Zeni, S. Borgström, P. Berardino, C. Del Gaudio, and R. Lanari, "Surface deformation analysis in the ischia island (italy) based on spaceborne radar interferometry," *Journal of Volcanology and Geothermal Research*, vol. 151, no. 4, pp. 399–416, 2006.

[71] F. Bozzano, C. Esposito, P. Mazzanti, M. Patti, and S. Scancella, "Imaging multi-age construction settlement behaviour by advanced sar interferometry," *Remote Sensing*, vol. 10, no. 7, p. 1137, 2018.

[72] M. Polcari, M. Albano, A. Montuori, C. Bignami, C. Tolomei, G. Pezzo, S. Falcone, C. La Piana, F. Doumaz, S. Salvi, *et al.*, "Insar monitoring of italian coastline revealing natural and anthropogenic ground deformation phenomena and future perspectives," *Sustainability*, vol. 10, no. 9, p. 3152, 2018.

[73] J. M. Delgado Blasco, M. Foumelis, C. Stewart, and A. Hooper, "Measuring urban subsidence in the rome metropolitan area (italy) with sentinel-1 snap-stamps persistent scatterer interferometry," *Remote Sensing*, vol. 11, no. 2, p. 129, 2019.

[74] A. Singleton, Z. Li, T. Hoey, and J.-P. Muller, "Evaluating sub-pixel offset techniques as an alternative to d-insar for monitoring episodic landslide movements in vegetated terrain," *Remote Sensing of Environment*, vol. 147, pp. 133–144, 2014.

[75] A. Manconi, F. Casu, F. Ardizzone, M. Bonano, M. Cardinali, C. De Luca, E. Gueguen, I. Marchesini, M. Parise, C. Vennari, *et al.*, "Brief communication: Rapid mapping of landslide events: The 3 december 2013 montescaglioso landslide, italy," *Natural Hazards and Earth System Sciences*, vol. 14, no. 7, pp. 1835–1841, 2014.

[76] L. Sun and J.-P. Muller, "Evaluation of the use of sub-pixel offset tracking method to monitor landslides in densely vegetated terrain in the three gorges region, china," in *Dragon 3Mid Term Results*, vol. 724, 2014.

[77] C. Lüttig, N. Neckel, and A. Humbert, "A combined approach for filtering ice surface velocity fields derived from remote sensing methods," *Remote Sensing*, vol. 9, no. 10, p. 1062, 2017.

[78] T. Strozzi, A. Luckman, T. Murray, U. Wegmuller, and C. L. Werner, "Glacier motion estimation using sar offset-tracking procedures," *IEEE Transactions on Geoscience and Remote Sensing*, vol. 40, no. 11, pp. 2384–2391, 2002.

[79] N. C. Riveros, L. D. Euillades, P. A. Euillades, S. M. Moreiras, and S. Balbarani, "Offset tracking procedure applied to high resolution sar data on viedma glacier, patagonian andes, argentina," 2013.

[80] J. Huang, K. Deng, H. Fan, and S. Yan, "An improved pixel-tracking method for monitoring mining subsidence," *Remote sensing letters*, vol. 7, no. 8, pp. 731–740, 2016.

[81] H. Fan, X. Gao, J. Yang, K. Deng, and Y. Yu, "Monitoring mining subsidence using a combination of phase-stacking and offset-tracking methods," *Remote Sensing*, vol. 7, no. 7, pp. 9166–9183, 2015.

[82] D. Amitrano, R. Guida, D. Dell'Aglio, G. Di Martino, D. Di Martire, A. Iodice, M. Costantini, F. Malvarosa, and F. Minati, "Long-term satellite monitoring of the slumgullion landslide using space-borne synthetic aperture radar sub-pixel offset tracking," *Remote Sensing*, vol. 11, no. 3, p. 369, 2019.

[83] M. Parise and R. Guzzi, *Volume and shape of the active and inactive parts of the Slumgullion landslide, Hinsdale County, Colorado*. US Department of the Interior, US Geological Survey, 1992.

[84] D. Crandell and D. Varnes, "Slumgullion earthflow and earthslide near lake city," *Colorado [abs.]: Geological Society of America Bulletin*, vol. 71, no. 12 pt 2, p. 1846, 1960.

[85] W. H. Schulz, J. A. Coe, P. P. Ricci, G. M. Smoczyk, B. L. Shurtleff, and J. Panosky, "Landslide kinematics and their potential controls from hourly to decadal timescales: Insights from integrating ground-based insar measurements with structural maps and long-term monitoring data," *Geomorphology*, vol. 285, pp. 121–136, 2017.

[86] R. Guzzi and M. Parise, "Surface features and kinematics of the slumgullion landslide, near lake city, colorado," US Geological Survey, Tech. Rep., 1992.

[87] J. Coe, J. Godt, W. Ellis, W. Savage, J. Savage, P. Powers, D. Varnes, and P. Tachker, "Preliminary interpretation of seasonal movement of the slumgullion landslide as determined from gps observations, july

1998–july 1999," *US Geological Survey, Open-File Report*, pp. 00–102, 2000.

[88] C. Wang, X. Mao, and Q. Wang, "Landslide displacement monitoring by a fully polarimetric sar offset tracking method," *Remote Sensing*, vol. 8, no. 8, p. 624, 2016.

[89] C. Wang, J. Cai, Z. Li, X. Mao, G. Feng, and Q. Wang, "Kinematic parameter inversion of the slumgullion landslide using the time series offset tracking method with uavsar data," *Journal of Geophysical Research: Solid Earth*, vol. 123, no. 9, pp. 8110–8124, 2018.

[90] B. G. Delbridge, R. Bürgmann, E. Fielding, S. Hensley, and W. H. Schulz, "Three-dimensional surface deformation derived from airborne interferometric uavsar: Application to the slumgullion landslide," *Journal of geophysical research: solid earth*, vol. 121, no. 5, pp. 3951–3977, 2016.

[91] P. Milillo, E. J. Fielding, W. H. Shulz, B. Delbridge, and R. Burgmann, "Cosmo-skymed spotlight interferometry over rural areas: The slumgullion landslide in colorado, usa," *IEEE Journal of Selected Topics in Applied Earth Observations and Remote Sensing*, vol. 7, no. 7, pp. 2919–2926, 2014.

[92] R. E. Tepel, "Landslides: Investigation and Mitigation," *Environmental and Engineering Geoscience*, vol. IV, no. 2, pp. 277–278, Jan. 1998.

[93] W. K. Smith, "Photogrammetric determination of movement on the slumgullion slide, hinsdale county, colorado 1985-1990," US Geological Survey, Tech. Rep., 1993.

[94] R. Fleming, R. L. Baum, and M. Giardino, *Map and description of the active part of the Slumgullion landslide, Hinsdale County, Colorado*. US Department of the Interior, US Geological Survey, 1999.

[95] B. Delbridge, R. Bürgmann, E. Fielding, and S. Hensley, "Kinematics of the slumgullion landslide from uavsar derived interferograms," in *2015 IEEE International Geoscience and Remote Sensing Symposium (IGARSS)*, IEEE, 2015, pp. 3842–3845.

[96] L. Shapiro and G. C. Stockman, "Computer vision," in *Prentice Hall*, 2002.

[97] S. Hensley, H. Zebker, C. Jones, T. Michel, R. Muellerschoen, and B. Chapman, "First deformation results using the nasa/jpl uavsar instrument," in *2009 2nd Asian-Pacific Conference on Synthetic Aperture Radar*, IEEE, 2009, pp. 1051–1055.

[98] J. Coe, J. Godt, W. Ellis, W. Savage, J. Savage, P. Powers, D. Varnes, and P. Tachker, "Seasonal movement of the slumgullion landslide as determined from gps observations, july 1998-july 1999," US Geological Survey, Tech. Rep., 2000.